

# UNCLASSIFIED

AD NUMBER
ADB972063
NEW LIMITATION CHANGE
TO Approved for public release, distribution unlimited
FROM Distribution authorized to U.S. Gov't. agencies and their contractors; Administrative/Operational Use; DEC 1966. Other requests shall be referred to National Aeronautics and Space Administration, Washington, DC.
AUTHORITY
NASA TR Server Website, 6 Nov 2006

THIS PAGE IS UNCLASSIFIED

UNANNOUNCED

AD-B972 063



NASA CONTRACTOR  
REPORT



NASA CR-652

NASA CR-652

CATALOGUED BY  
NMC TECHNICAL LIBRARY

acc #  
145-7571

RECORD COPY

# CRYOGENIC LIQUID EXPERIMENTS IN ORBIT

VOLUME II: BUBBLE MECHANICS,  
BOILING HEAT TRANSFER, AND  
PROPELLANT TANK VENTING IN A  
ZERO-GRAVITY ENVIRONMENT

DTIC  
ELECTE  
DEC 22 1993  
S E D

by Jay L. McGrew and B. K. Larkin

Prepared by  
MARTIN MARIETTA CORPORATION  
Denver, Colo.  
for George C. Marshall Space Flight Center

93-30854



NATIONAL AERONAUTICS AND SPACE ADMINISTRATION • WASHINGTON, D. C. • DECEMBER 1966

93 12 21 194

2a Dec 1966

2 CRYOGENIC LIQUID EXPERIMENTS IN ORBIT,  
1, 2:  
~~VOLUME II~~ BUBBLE MECHANICS, BOILING HEAT TRANSFER,  
AND PROPELLANT TANK VENTING IN A  
ZERO-GRAVITY ENVIRONMENT //

By Jay L. McGrew and B. K. Larkin

Distribution of this report is provided in the interest of information exchange. Responsibility for the contents resides in the author or organization that prepared it.

Prepared under Contract No. NAS 8-11328 by  
/ MARTIN MARIETTA CORPORATION  
Denver, Colo. //

for George C. Marshall Space Flight Center

NATIONAL AERONAUTICS AND SPACE ADMINISTRATION

### FOREWORD

This report was prepared by the Martin Company, Denver, Colorado, under Contract NAS8-11328, Criteria for Cryogenic Liquid Experiments in Orbit, for the George C. Marshall Space Flight Center of the National Aeronautics and Space Administration. The work was administered under the technical direction of the Propulsion and Vehicle Engineering Laboratory, George C. Marshall Space Flight Center, with Leon Hastings acting as project manager.

Accession For	
NTIS CRA&I	<input type="checkbox"/>
DTIC TAB	<input type="checkbox"/>
Unannounced	<input checked="" type="checkbox"/>
Justification .....	
By .....	
Distribution /	
Availability Codes	
Dist	Avail and/or Special
12	

DTIC QUALITY INSPECTED 3

## CONTENTS

	<u>Page</u>
Foreword . . . . .	iii
Contents . . . . .	v
Summary . . . . .	ix
Symbols . . . . .	x and xi
I.     Boiling Heat Transfer and Bubble Mechanics in Zero Gravity . . . . .	1
A.   Introduction . . . . .	1
B.   Technical Discussion . . . . .	2
C.   Experimental Apparatus . . . . .	22
D.   Experimental Results and Conclusions . . . . .	39
II.    Liquid Venting . . . . .	54
A.   Introduction . . . . .	54
B.   Experimental Program . . . . .	55
C.   Results and Conclusions . . . . .	71
References . . . . .	80
Appendix A -- Analysis of Buoyancy Force with Nonconstant Density . . . . .	A-1
Appendix B -- Cantilevered Spring Wire . . . . .	B-1
 <u>Figure</u>	
1     A Bubble on an Inclined Surface . . . . .	10
2     Dimensionless Volume vs Contact Angle, Normal Gravity . . . . .	18

3	Hydrogen Bubble Diameter vs Contact Angle Normal Gravity . . . . .	19
4	Hydrogen Bubble Diameter in Low Gravity . . . . .	21
5	Marangoni Flow Experiment 1, Experimental Apparatus . . . . .	23
6	Marangoni Flow Experiments 2 and 3 Experimental Apparatus . . . . .	25
7	Bubble Thermophoresis Experimental Apparatus . . .	27
8	Bubble Thermophoresis Lighting and Viewing Schematic . . . . .	28
9	Bubble Thermophoresis Experimental Apparatus (without bubble holder) . . . . .	29
10	Bubble Force Experiment Bubble Insertion Technique (Expanded View: Bubble Holder and Thermocouple Probes) . . . . .	30
11	Boron Tungsten Wire Calibration . . . . .	31
12	Bubble on a Heated Surface Experimental Apparatus .	33
13	Boiling Apparatus . . . . .	35
14	Photograph of Boiling Apparatus . . . . .	36
15	Drop Capsule Schematic . . . . .	38
16	Marangoni Flow (Flow Away from Heated Center Rod, sec) Experiment 1 (Test Liquid n-Butyl Alcohol) . .	40
17	Marangoni Flow (Flow Forward Cooled Center Rod, sec), Experiment 1 (Test Liquid, n-Butyl Alcohol) .	41
18	Marangoni Flow (sec) Experiment 2 (Test Liquid, n-Butyl Alcohol) . . . . .	42
19	Bubble Force Parameter vs Liquid Temperature Gradient (Test Liquid, n-Butyl Alcohol) . . . . .	43
20	Bubble Force Parameter vs Liquid Temperature Gradient (Test Liquid, Methanol) . . . . .	44

21	Marangoni Flow Around Air Bubbles on a Heated Surface . . . . .	46
22	Liquid Flow at a Bubble Surface . . . . .	48
23	Shadowgraphs of Density Patterns in the Vicinity of Air Bubbles in n-Butyl Alcohol . . . . .	50
24	Boiling Experiment, Bubble Formation in Normal and Zero Gravity (Test Liquid, Liquid Hydrogen) .	52
25	Line Drawing of the Experimental Apparatus . . .	56
26	Front View Experimental Apparatus . . . . .	57
27	Reservoir - Side View . . . . .	58
28	Camera - Side View . . . . .	59
29	Experimental Apparatus with Pressure Readout and Control Equipment . . . . .	60
30	Zero - Gravity Venting of Freon TF, Cylinder Diameter = 29.2 cm, Vent Valve 1/2 Turn Open . .	62
31	Zero - Gravity Venting of Freon TF, Cylinder Diameter = 15.2 cm, Vent Valve 1/2 Turn Open . . .	63
32	Zero - Gravity Venting of Freon TF, Cylinder Diameter = 15.2 cm, Vent Valve 1 Turn Open . . . .	64
33	16-ft Droptower Facility . . . . .	67
34	Venting Experiment, 8-in. Hydrogen Dewar . . . .	68
35	Hydrogen Venting Apparatus . . . . .	69
36	Hydrogen Venting Schematic . . . . .	70
37	Venting Test 30 . . . . .	73
38	Venting Test 24 (Using Liquid Hydrogen) . . . . .	75
39	Venting Test 47 . . . . .	76
40	Pressure Change from Venting . . . . .	78

Table

1	Liquid Hydrogen Venting Data . . . . .	72
---	----------------------------------------	----

## SUMMARY

Many propellant storage and handling problems encountered by the Saturn V/S-IVB, and other vehicles can be solved only by orbiting experiments. Because of the complexities and cost of such an operation, it is necessary to design the experiments carefully. This project was planned to clarify certain aspects of heat transfer and fluids mechanics pertaining to low-gravity conditions and thus support the experimental effort.

Research programs concerned with bubble behavior and boiling phenomena and propellant tank venting are reported herein. A fourth portion of this project concerned with propellant settling and interface dynamics is reported in Volume I of this report.

Boiling Heat Transfer and Bubble Mechanics - The behavior of bubbles in a zero-gravity environment was investigated both experimentally and theoretically. Liquid flow around bubbles, which flow results strictly from surface tension gradients, was shown to cause an appreciable net force on the bubble. Theoretical prediction of the bubble force was made and was found to agree very well with experimental results.

Temperature induced liquid flow around bubbles as a heat transport mechanism was investigated. Liquid flow and temperature patterns were studied by use of various optical techniques. The growth and departure of boiling-produced vapor bubbles were studied.

Liquid Venting - The phenomena of zero-gravity venting with boiling liquids was investigated. Freon and liquid hydrogen were used as test fluids in drop tower experiments.

Data Film - Sixteen millimeter movie films of test results are available on request. The film can be obtained by requesting:

Film Supplement to Program Final Report NAS8-11328  
Martin CR-66-25 Vol II

from: Photographic Branch  
Technical Services TS-P  
MSFC  
Redstone Arsenal, Alabama.



## SYMBOLS

a	The capillary constant
b	Radius of curvature of bubble origin
ds	Segment of arc on bubble surface
F	Coefficient in Young's equation
f	Force
$F_b$	Buoyancy force
$F_t$	Thermophoretic force
g	Acceleration
$\bar{g}$	Local gravity vector
k	Coefficient in Young's equation
$K_E$	Eötvös constant $-(\text{erg mole}^{-2/3} \text{ deg}^{-1})$
M	Mass of one gram formula weight of substance
$P_T$	Tangential pressure
r	Bubble radius
R	Radius of Curvature
t	Time
T	Temperature
U	Dimensionless variable (bubble shape analysis)
W	Dimensionless variable
X	Coordinate variable
Y	Coordinate variable
Z	Coordinate variable
$\alpha$	Angle of inclination of plane
$\lambda$	Surface tension gradient

$\beta$	Bond number for bubbles
$\gamma$	Interfacial tension (deg/cm)
$\Gamma$	$= \gamma (M/\rho)^{2/3}$
$\theta$	Angular coordinate
$\rho, \rho_L, \rho_g$	Density, liquid and gas density
$\phi$	Contact angle
$\psi$	Dimensionless force
$\mu$	Viscosity

## I. BOILING HEAT TRANSFER AND BUBBLE MECHANICS IN ZERO GRAVITY

### A. INTRODUCTION

Nucleate boiling and the general behavior of bubbles play significant roles in the control of cryogenic propellants in zero gravity. The objective of this study was to investigate various facets of nucleate boiling and bubble behavior such that analyses of certain aspects of zero-gravity propellant management becomes possible. Even though the process of nucleate boiling in zero gravity has been studied extensively by a number of investigators (Ref 1, 2, 3, and 4), many significant questions have remained unanswered. The most critical unsolved problems are concerned with heat transfer rates and bubble configuration during boiling. In normal gravity situations, high boiling heat transfer rates are obtained. The high rates of heat transfer are classically explained in terms of the turbulence and mixing resulting from rapid growth and departure of the bubble from the heating surface. Experiments show that high heat transfer rates are also obtained in zero gravity (Ref 1 and 3) and in fact zero-gravity and normal gravity data obtained by Shirley (Ref 3) are identical. Thus the classical model for the boiling process requires rapid growth and departure of bubbles from the heating surface even in zero-gravity.

In the investigation discussed below, the growth and departure of boiling-produced vapor bubbles were studied. Bubble growth rate and size at departure are pertinent to both the problem of heat transfer rate and the migration of bubbles in the bulk liquid in low gravity. Assuming that the bubble might depart from the heating surface, the motion of the bubble under the influence of surface tension and vapor pressure gradients was investigated. Also, surface tension gradient-produced liquid convection around the bubble was studied as an additional mechanism for heat transfer in zero-gravity.

## B. TECHNICAL DISCUSSION

### 1. Surface Flow Phenomena (Marangoni Flow)

The phenomena of liquid flow at a liquid/vapor interface under the influence of surface tension gradients has been known for over one hundred years. The flow effect was first described by Marangoni (Ref 5) as follows: "If for any reason differences of surface tension exist along a free liquid surface, liquid will flow toward the region of higher surface tension." The above flow phenomena termed Marangoni flow generally results from inhomogeneities in the liquid phase such as result from concentration differences or temperature differences. An example of Marangoni flow is observed in "wine tears" formed around the rim of a glass of wine. Normal capillary forces cause some of the wine to climb up the rim of the glass where evaporation of ethyl alcohol from the wine occurs. Surface tension of alcohol/water mixtures increases with decreasing alcohol content, thus the liquid depleted of alcohol by evaporation tends to concentrate at the rim of the glass away from the liquid surface and surface tension unbalance pulls wine up the glass. As liquid is pulled up the glass, droplets of liquid develop becoming quite large and break away and flow down the glass, thus the name wine tears. A continual flow of liquid up the glass under the influence of surface tension gradients and down the glass as droplets is established.

Temperature differences along a liquid surface will also result in surface tension gradients and Marangoni flow. This effect is of a particular importance in the following discussions. The relationship between surface tension and liquid temperature is expressed by the Eötvös equation:

$$-K_E = \frac{d\gamma}{dT} = \frac{d[\gamma(M/\rho)^{2/3}]}{dT} \quad [1]$$

The Eötvös constant for various liquids is tabulated:

<u>Liquid</u>	<u>K<sub>E</sub></u>
Acetone	+1.9
Carbon tetrachloride	+2.2
Phenol	+1.85
Toluene	+2.2
Hydrogen	+1.36
Nitrogen	+2.0
Oxygen	+1.9

As can be seen from the above data, many liquids have an Eötvös constant of approximately +2.0. This is a general tendency for liquids. In any event the Eötvös constant is always a positive number, thus the numerical value of  $\Gamma$  decreases with temperature, and since  $\rho$  decreases with temperature,  $\gamma$  must also decrease with temperature, which is the general case for liquids. Thus, if temperature differences exist along a liquid/vapor interface, Marangoni flow will be observed (liquid flowing at the surface toward the colder region).

Surface tension driven convection in a pool of liquid has been studied by various investigators (Ref 6). In addition, Marangoni flow results in several interesting and important effects in bubble behavior and boiling heat transfer. These effects are discussed below.

## 2. Bubble Thermophoresis

Consider a gas or vapor bubble in a pool of nonisothermal liquid. As previously discussed, Marangoni flow should be established due to temperature induced surface tension gradients around the bubble. Considering the manner in which surface tension varies with temperature, the surface tension force unbalance will result in liquid flow around the bubble from the hot toward the cold region. Thus, if the bubble surface is capable of applying a directed net force to the surrounding liquid, an equal and opposite reaction force must be experienced by the bubble. An analysis of the force on the bubble is given next.

Forces on the Bubble - The net resultant force on the bubble due to Marangoni flow can readily be determined by considering the surface tension force unbalance over the bubble surface. A few words of explanation concerning the following analysis are in order. For sake of simplicity in analysis and experimentation, the temperature patterns will be such that:

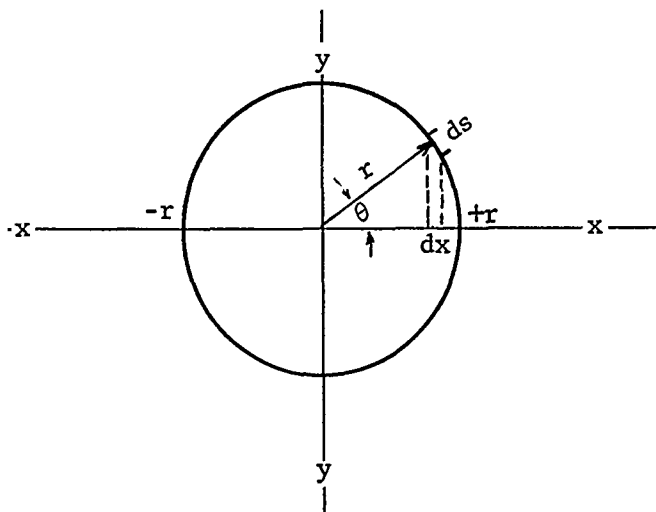
$$\frac{\partial T}{\partial z} = \frac{\partial T}{\partial y} = 0, \quad [2]$$

and

$$\frac{\partial T}{\partial x} = \text{constant}. \quad [3]$$

Thus flow around the bubble will be symmetrical about the x axis, and the net resultant force on the bubble will lie along the x

axis. Since the surface tension of the liquid changes from point to point over the bubble surface, tangential forces will be exerted in addition to the normal forces.\* In the following analysis it is assumed that the normal component of surface tension at a point is balanced by the pressure difference across the membrane at that point, and that the net force acting on the bubble can be determined by integrating the tangential component over the bubble surface. The bubble is not spherical because of the variations in the normal component of surface tension, but sphericity will be assumed to facilitate the analysis. This simplification will lead to only minor errors. The geometry used in the analysis is shown below.



The tangential (shear) pressure at the bubble surface is given by:

$$P_T = \frac{dy}{ds}, \quad [4]$$

where

$$ds = \frac{dx}{\sin \theta}.$$

Also:

$$2\pi y ds = dA, \quad [5]$$

and

$$P_T = \frac{df}{dA} = \frac{df}{2\pi y ds}, \quad [6]$$

---

\*V. G. Levich: Physicochemical Hydrodynamics. P 380 and 381, Prentice Hall Inc., Englewood Cliffs, California, 1962.

where

$$df = (2\pi y ds) \frac{dy}{dx} \sin \theta = 2\pi y dx \frac{dy}{dx}.$$

Assume:

$$\gamma = a + \lambda x, \quad [7]$$

then

$$\frac{dy}{dx} = \lambda.$$

Thus:

$$df = 2\pi \lambda y dx. \quad [8]$$

Taking the x component of df:

$$dF_t = df \sin \theta;$$

$$dF_t = 2\pi y \lambda \sin \theta dx;$$

$$y = r \sin \theta;$$

$$x = r \cos \theta, \quad dx = -r \sin \theta d\theta;$$

So

$$F_t = -2\pi \lambda r^2 \int_{\pi}^0 \sin^3 \theta d\theta; \quad [9]$$

$$F_t = 2/3 \pi r^2 \lambda \left[ \cos \theta (\sin^2 \theta + 2) \right]_{\pi}^0$$

Finally, the net thermophoretic force on the bubble is:

$$F_t = 8/3 \pi r^2 \lambda. \quad [10]$$

Neglecting the variation in liquid density with temperature, which is a reasonable assumption for our purposes,\* the buoyancy force on a spherical bubble is:

$$F_b = 4/3 \pi r^3 (\rho_L - \rho_g) g. \quad [11]$$

Taking the ratio of thermophoretic force to the buoyancy force:

$$\psi = \frac{F_t}{F_b} = \frac{8/3 \pi r^2 \lambda}{4/3 \pi r^3 (\rho_L - \rho_g) g} = \frac{2\lambda}{r(\rho_L - \rho_g) g}. \quad [12]$$

Quantitative measurements of the thermophoretic force on bubbles were made by Young, Goldstein, and Block (Ref 7).

In their experiments small bubbles were held motionless in a vertical temperature gradient such that the thermophoretic force acting downward on the bubble was in balance with the buoyancy force. From dimensional analysis they developed the expression:

$$\frac{\partial T}{\partial x} = \frac{k}{\partial T} (\rho_L - \rho_g) g r F \left[ (\mu/\rho) (gr^3)^{\frac{1}{2}} - - - \right]. \quad [13]$$

In experiments using silicone oils, they evaluated the terms  $k$  and  $F$ , finding them to be  $k = 2/3$ , and  $F = 1$ .

Thus:

$$\frac{\partial T}{\partial x} \cdot \frac{\partial \gamma}{\partial T} = \frac{\partial \gamma}{\partial x} = \lambda = 2/3 gr (\rho_L - \rho_g) \quad [14]$$

Now since in their experiments  $F_T = F_b$ ,  $\psi = 1$ , then:

---

\*The buoyancy force on a spherical bubble is given:  $F_b = 4/3 \pi r^3 (\rho_o + 2\alpha r) g$ , for the case  $\rho_o \gg \rho_g$ , and  $\rho = (\rho_o + \alpha y)$  (See Appendix A).



$$1 = \frac{\frac{\partial T}{\partial x} \frac{\partial \gamma}{\partial T}}{2/3 \, g r (\rho_L - \rho_g)} = \frac{3/2 \, \lambda}{r (\rho_L - \rho_g) g}. \quad [15]$$

Comparing the experimental result of Young with the similar theoretical result derived above, we find:

$$\frac{r (\rho_L - \rho_g) g}{\lambda} = 1.5 = 1/k \text{ (Young's expression);} \quad [16]$$

$$\frac{r (\rho_L - \rho_g) g}{\lambda} = 2.00 = 1/k \text{ (McGrew's expression).} \quad [17]$$

It is seen that Eq [16] results in a somewhat lower  $1/k$  value than in Eq [17]. A further discussion of the departure and a possible explanation is given in a later Section D.

In addition to the bubble force resulting from surface tension variations, some effect of liquid/vapor pressure is to be expected. If a variation of vapor pressure around the bubble surface exists, then mass transfer will occur through the bubble. Liquid will evaporate on the warm side and vapor will condense on the cold side of the bubble. The evaporation and condensation process will result in a tendency for the bubble to migrate toward the hotter liquid region. Although the effect of vapor pressure is understood in a qualitative sense, insufficient study of the effect has been accomplished to permit a meaningful analysis. In general, however, the effect of liquid/vapor pressure will result in an increased thermophoretic force, but no analytical prediction of the relative effect of vapor pressure versus surface tension forces is proposed.

### 3. Liquid Convection Due to Marangoni Flow around the Bubble

The phenomena of liquid flow around bubbles as a consequence of surface tension gradients has been previously discussed. It has been stated that liquid will flow from the hot region toward the cold region, thus Marangoni flow results in convective transfer of both mass and heat. No analyses of the convection mechanisms resulting from Marangoni flow are presented, but the experimental results are reported in a later section of this report.

#### 4. Bubble Shape and Boiling

The most popular method of predicting bubble shape and size at departure is that developed by Fritz (Ref 8). Capillary theory, based upon the work of Bashforth and Adams (Ref 9), serves as the basis for the Fritz correlation. Because of the simplicity of this theory, only elementary physical properties are necessary as input data. These properties are interfacial tension, contact angle, and vapor and liquid densities. By using these data, the magnitude of the local gravitational field, and the angle of inclination of the surface, it is possible to predict bubble shapes and volumes at departure from a heating surface. Satisfactory comparisons between this theory and experimental results may be found in the work of Fritz (Ref 8), Jakob (Ref 10), and Siegel and Keshock (Ref 11).

It is interesting to note that the capillary theory which is useful for the prediction of bubble sizes has a plurality of other applications. The capillary theory for bubbles is identical with that for liquid drops. In this latter connection, there are applications for the theory in spraying insecticides on plant leaves, recovering petroleum in underground reservoirs, condensing heat transfer, and wetting of polymers. The works of Kawasaki (Ref 12), Furmidge (Ref 13), and Bikerman (Ref 14) concerning the shape of liquid drops on an inclined surface were used to test the accuracy of the numerical computations.

The capillary theory of bubble growth has not been successful in all applications however. Because this theory assumes that bubble departure is governed by a buoyancy force, the validity of its application to low gravity problems has been questioned. Bubble growth on a surface certainly induces an inertial force, and it seems that this force might become dominant in low gravity applications. Indeed, Clarke and Merte (Ref 15), using assumed bubble sizes, show that inertial forces dominate buoyancy forces even for normal earth gravity condition for oxygen, nitrogen, hydrogen, and water.

It is generally observed that theoretical analyses of bubble growth and departure meet with only limited success. A fundamental source of difficulty is in describing the shape of the liquid/vapor interface. While capillary theory describes the interface, it neglects several factors of possible importance -- inertial and drag forces. Other models which do include inertial and drag forces always require assumptions concerning the interface. Thus, there is no single theory which may be relied upon

for all conditions. The following material applies capillary theory and some experimental data to the problem of bubble growth and departure in a near zero gravitational field. The work of Fritz (Ref 8) is generalized in the following discussion to the extent that the boiling surface need not be horizontal but may have any orientation.

Application of Capillary Theory - Since the equations describing the shape of a bubble (or drop) on an inclined surface are not available in the literature, a detailed derivation is presented here.

Requirements for static equilibrium across an interface lead to the Laplace equation:

$$\Delta P = \gamma \left( \frac{1}{R_1} + \frac{1}{R_2} \right), \quad [18]$$

where  $\Delta P$  is the pressure difference across the interface,  $\gamma$  is the interfacial tension, and the  $R$ s are radii of curvature at the interface [see p 6 of Adamson (Ref 16) for a derivation]. For a bubble (or drop) attached to a flat surface, it is assumed that at some point the interface has a tangent plane which is parallel to the flat surface (see Fig. 1). This point is the origin. The  $Z$  axis of a Cartesian system is chosen to be perpendicular to flat surfaces -- positive direction is toward the flat surface. Let  $\vec{g}$  be a vector representing the local gravitational field. This  $\vec{g}$  intersects the  $Z$  axis at angle  $\alpha$  and  $X$  axis is assumed to lie in the plane determined by  $\vec{g}$  and the  $Z$  axis. Since both  $Z$  and  $X$  axes are now determined, the  $Y$  axis is fixed by assuming a right-handed coordinate system.

Equation [18] applies at every point on the interface, and in particular, it applies at the origin:

$$\Delta P_o = \frac{2\gamma}{b}, \quad [19]$$

where the sum of curvatures at the origin are used to define  $b$  in Eq [19].

From the assumption of hydrostatic equilibrium, the pressure difference may also be written as:

$$\Delta P = \Delta P_o + g\Delta\rho (X \sin \alpha - Z \cos \alpha), \quad [20]$$

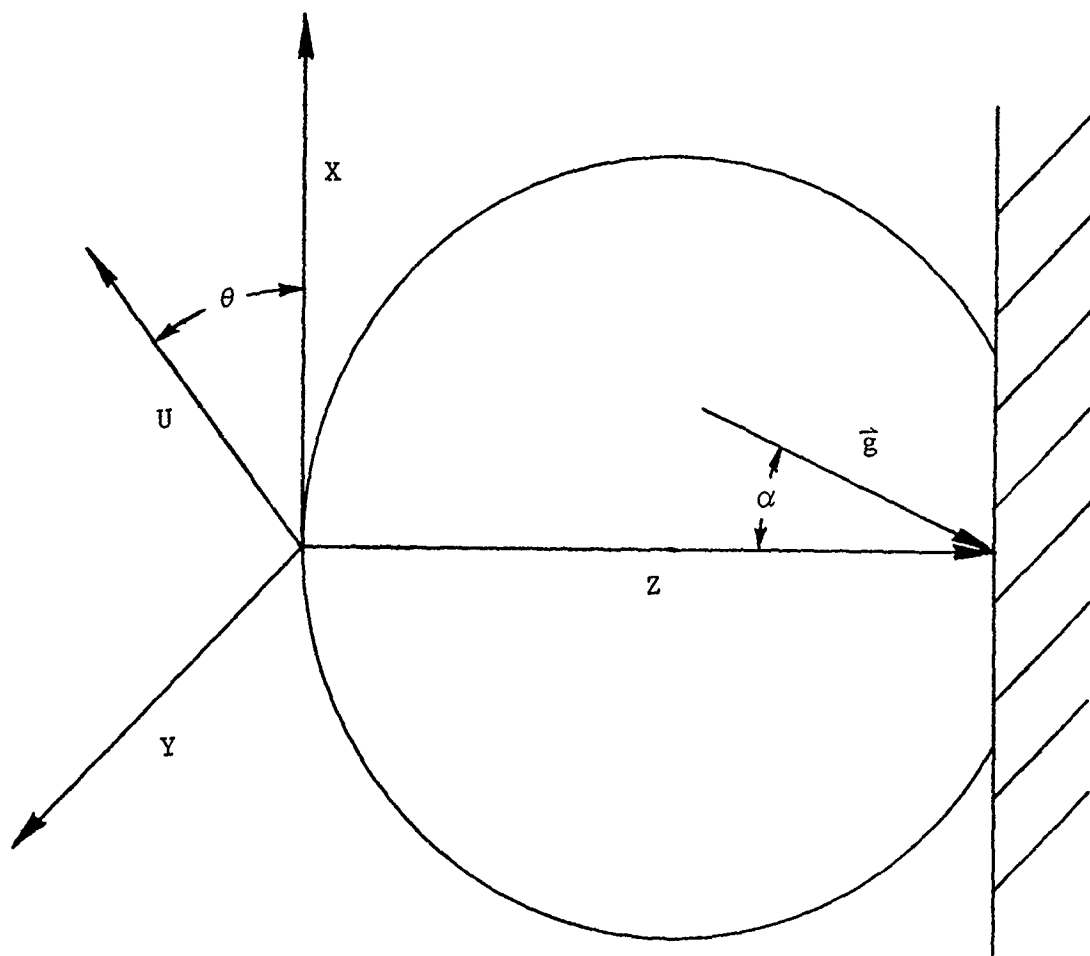


Fig. 1 A bubble on an Inclined Surface

where  $\Delta\rho$  is the density of liquid minus density of the vapor in the bubble, and  $g$  is the magnitude of  $\vec{g}$ . Pressures are eliminated between Eq [18], [19], and [20], and the result may be written:

$$\frac{1}{R_1} + \frac{1}{R_2} = \frac{2}{b} + \frac{g\Delta\rho}{\gamma} (X \sin \alpha - Z \cos \alpha). \quad [21]$$

It is assumed that the interface is represented by a relationship between coordinates  $X$ ,  $Y$ , and  $Z$  of a surface point. This relationship may be written as  $Z$  equals  $f(X,Y)$ , where  $f$  has continuous second partial derivatives. If this is the case, then the curvatures in Eq [21] may be written as derivatives following Bateman (Ref 17), p 170:

$$\frac{1}{R_1} + \frac{1}{R_2} = \frac{\partial}{\partial X} (p/H) + \frac{\partial}{\partial Y} (q/H);$$

$$p = \frac{\partial Z}{\partial X}, \quad q = \frac{\partial Z}{\partial Y}; \quad [22]$$

and

$$H = (1 + p^2 + q^2)^{\frac{1}{2}}.$$

By combining Eq [21] and [22], one obtains a nonlinear partial differential equation. When  $\alpha$  equals zero, the equation is equivalent to the equation of Bashforth and Adams (Ref 9).

Certain boundary conditions are necessary to complete the statement of the problem. From the manner in which the origin was chosen, it is obvious that

$$\frac{\partial Z}{\partial X} = \frac{\partial Z}{\partial Y} = 0 \quad [23]$$

at the origin. Since the origin is on the surface, it follows that

$$Z(0,0) = 0. \quad [24]$$

Because the  $XZ$  plane is a plane of symmetry, it is only necessary to deal with half the bubble, say that corresponding to  $Y$  greater than zero.

Surfaces of revolution are frequently found to be solutions to the above system and it seems that cylindrical coordinates would be more efficient than Cartesian coordinates. The equation of transformation are:

$$\begin{aligned} X &= bU \cos \theta \\ Y &= bU \sin \theta \\ Z &= bW \end{aligned} \quad [25]$$

where  $U$  is a dimensionless radius,  $W$  is a dimensionless axial distance, and  $\theta$  is the angle between  $U$  and the  $X$  axis. In these new coordinates, the equation of the interface is:

$$\begin{aligned} &\left(1 + \frac{W_\theta^2}{U^2}\right) W_{uu} - \frac{2W_u}{U^2} W_\theta W_{u\theta} + \left(1 + \frac{W_u^2}{U^2}\right) \frac{W_{\theta\theta}}{U^2} + \\ &+ \left(1 + \frac{W_u^2}{U^2} + \frac{2}{U^2} W_\theta^2\right) \frac{W_u}{U} = \left[2 + \beta(U \sin \alpha \cos \theta - W \cos \alpha)\right] \\ &\left(1 + \frac{W_u^2}{U^2} + \frac{W_\theta^2}{U^2}\right)^{3/2} \end{aligned} \quad [26]$$

where  $\beta$  equals  $b^2 g \Delta\rho/\gamma$ . Note that subscripts on  $W$  indicate differentiation.

If one were to solve Eq [26] by finite differences, the results would be a set of  $W$  values established at lattice points in the  $U$ - $\theta$  plane. This is not the most convenient form, since the bubble terminates on a flat surface ( $W$  is a constant). Thus the equation is transformed from independent variables  $U$  and  $\theta$  to independent variables  $W$  and  $\theta$ . Identities that were used in this transformation are:

$$\begin{aligned} W_u &= U_w^{-1}; \\ W_\theta &= -U_w^{-1} U_\theta; \\ W_{uu} &= -U_w^{-3} U_{ww}; \end{aligned}$$

$$W_{u\theta} = U_w^{-3} U_\theta U_{ww} - U_w^{-2} U_{w\theta};$$

$$W_{\theta\theta} = 2U_\theta U_w^{-2} U_{w\theta} - U_w^{-1} U_{\theta\theta} - U_\theta^2 U_w^{-3} U_{ww}. \quad [27]$$

After substituting Eq [27] into Eq [26] and simplifying, the following equations are obtained:

$$AU_{ww} + 2BU_{w\theta} + CU_{\theta\theta} + D = 0, \quad [28]$$

where

$$A = 1 + \frac{U_\theta^2}{U^2},$$

$$B = - \frac{U_w U_\theta}{U^2},$$

$$C = \frac{1 + U_w^2}{U^2},$$

$$D = (2 + \beta(U \sin \alpha \cos \theta - W \cos \alpha)) \left(1 + U_w^2 + \frac{U_\theta^2}{U^2}\right)^{3/2} - \frac{1}{U} \left(1 + U_w^2 + \frac{2U_\theta^2}{U^2}\right).$$

Equation [28] is the form of the capillary equation which was solved in this program. Certain limiting forms may be solved with comparative ease. If  $\beta$  is zero, then the equation for a spherical surface satisfies Eq [28]. If  $\alpha$  is zero, the surface is one of revolution, and all theta derivatives in Eq [28] vanish. Thus, Eq [28] becomes an ordinary differential equation. This equation was solved by hand calculation in 1857 (with the aid of a £ 50 grant from the Royal Society), and the results were published by Bashforth and Adams (Ref 9).

Because of the nonlinear character of Eq [28], the development of an exact solution was not possible. However, a simple method for numerical solution was developed such that the problem was easily handled by an IBM 7094 computer. Solution of Eq [28] for a single value of  $\beta$  only requires about 0.5-minute machine time.

Finite difference solutions are generated using dependent variables  $V$  and  $Q$  where:

$$V = \frac{\partial U}{\partial W}, \quad Q = \frac{\partial U}{\partial \theta}. \quad [29]$$

The equations to be solved are:

$$A \frac{\partial V}{\partial W} + 2B \frac{\partial V}{\partial \theta} + C \frac{\partial Q}{\partial \theta} + D = 0, \quad [30]$$

and

$$\frac{\partial V}{\partial \theta} = \frac{\partial Q}{\partial W}. \quad [31]$$

Solutions are generated on a set of lattice points in the  $\theta$ - $W$  plane. By using  $n$  equally spaced points over the interval  $0 \leq \theta \leq \pi$ , the increment  $\Delta\theta$  is given by:

$$\Delta\theta = \pi/(n-1). \quad [32]$$

Subscripts on the dependent variables designate lattice points, for example,

$$V_{j,k} = V(j\Delta\theta, k\Delta W). \quad [33]$$

Assuming that coefficients  $A$ ,  $B$ ,  $C$ ,  $D$  are known at line  $k$ , then the dependent variables are found at line  $k+1$  by solving:

$$\begin{aligned} \frac{A}{\Delta W} (V_{j,k+1} - V_{j,k}) + \frac{B}{\Delta\theta} (V_{j+1,k+1} - V_{j-1,k+1}) + \\ + \frac{C}{2\Delta\theta} (Q_{j+1,k} - Q_{j-1,k}) + D = 0; \end{aligned} \quad [34]$$

$$Q_{j,k+1} - Q_{j,k} = \frac{\Delta W}{2\Delta\theta} (V_{j+1,k+1} - V_{j-1,k+1}), \quad [35]$$

$$U_{j,k+1} - U_{j,k} = \frac{\Delta W}{2} (V_{j,k+1} + V_{j,k}). \quad [36]$$



To solve Eq [34] it is necessary to treat a system of simultaneous equations at each  $k$  level. Fortunately, the system is tridiagonal, and the procedure of Peaceman and Rachford (Ref 18) applies. Coefficients in Eq [34] vary with position, and the following are used in Eq [28]:

$$\begin{aligned} U &= U_{j,k}; \\ U_w &= V_{j,k}; \\ U_\theta &= Q_{j,k}. \end{aligned} \quad [37]$$

Derivatives of both  $U$  and  $V$  with respect to  $\theta$  equal zero at 0 and  $\pi$ . This requirement was approximated using equations of the following type:

$$3U_{1,k} - 4U_{2,k} + U_{3,k} = 0. \quad [38]$$

Computations were started at  $k$  equals one -- not  $k$  equals zero. For the region between zero and one (the first  $\Delta W$  increment), the surface was assumed to be spherical. Starting values along the line  $k$  equals one, as obtained from the spherical approximation, are:

$$\left. \begin{aligned} U_{j,1} &= \sqrt{2\Delta W}; \\ V_{j,1} &= (1 - \Delta W)/U_{j,1}; \\ Q_{j,1} &= 0. \end{aligned} \right\} \quad j = 1, 2, \dots, n; \quad [39]$$

Both surface area and volume at  $k$  equals one were computed by assuming sphericity. Additional increments of area and volume were estimated by:

$$S_j = \left[ (\Delta W)^2 + (U_{j,k+1} - U_{j,k})^2 \right]^{\frac{1}{2}}; \quad [40]$$

$$\Delta A = \frac{\Delta \theta}{2} \sum_{j=0}^{n-2} (S_j + S_{j+1}) (U_{j,k+1} + U_{j+1,k+1}); \quad [41]$$

$$\Delta V = \frac{\Delta W \Delta \theta}{4} \sum_{j=0}^{n-2} \left( U_{j,k+1} + U_{j+1,k+1} \right)^2; \quad [42]$$

where  $\Delta A$  and  $\Delta V$  are incremental surface and volume, respectively, between lines  $k$  and  $k+1$ .

The computations, as outlined above, may be terminated when a certain contact angle is obtained. It has been observed (Ref 12, 13, 14) that the angle of intersection between an interface and the inclined surface is not constant but varies with position. Thus, it seems necessary to define "contact angle" for an inclined surface. In defining contact angle, one may use the Dupré equation as presented by Adamson (Ref 16 p 265). The derivation may be based either upon a balance of forces or by minimizing energy. In either case, the fact that the bubble may be in a gravitational field is neglected. For bubbles on a horizontal surface, such derivations seem to be valid, because displacements of the line of solid/liquid/vapor contact are perpendicular to the gravitational field.

It is possible to find a point on an inclined surface such that the line of solid/liquid/vapor contact moves perpendicular to  $\vec{g}$ . Let  $\vec{\lambda}$  be a vector in the solid surface, which is normal to the line of contact. Direction numbers of  $\vec{g}$  and  $\vec{\lambda}$  are  $(\sin \alpha, 0, -\cos \alpha)$  and  $\frac{\partial Z}{\partial X}, \frac{\partial Z}{\partial Y}, 0$ , respectively. But  $\vec{g}$  and  $\vec{\lambda}$  are perpendicular whenever  $\frac{\partial Z}{\partial X}$  equals zero. This latter derivative will be zero whenever  $h(\theta)$  is zero where:

$$h(\theta) = \cos \theta + \frac{\sin \theta}{U} U_{\theta}. \quad [43]$$

Note that  $h(\theta)$  is one, and  $h(\pi)$  is minus one. Assuming  $h(\theta)$  defines a continuous function, then there will be a value  $\theta_0$  between 0 and  $\pi$  such that  $h(\theta_0)$  equals zero. At  $\theta_0$ , the angle of intersection between the bubble and the inclined surface will be the same as that for a horizontal surface.

In the computer procedure,  $h(j\Delta\theta)$  is computed for increasing  $j$  until a root is found. The value of  $\theta_0$  is estimated by linear interpolation. If  $\phi$  is the angle of intersection between the bubble and the inclined surface, then it may be given by:

$$\phi = \frac{\pi}{2} + \tan^{-1} \left[ U_w \left( 1 + (U_{\theta}/U)^2 \right)^{\frac{1}{2}} \right]. \quad [44]$$

The machine program evaluates  $\phi$  at  $j$  and  $j-1$  where,  $(j-1) \theta \leq \theta_0 \leq j \theta$ , and  $\phi$  at  $\theta_0$  is computed by linear interpolation. Advancing and receding angles  $\phi(\pi)$  and  $\phi(0)$  are also computed.

Computations were performed for bubbles and drops on planes inclined at 30, 60, and 90 deg with  $\vec{g}$  using a  $\Delta W$  increment of 0.001. For the capillary Eq [28] and the definition of  $\beta$ , it follows that  $\beta$  is positive for bubbles and negative for drops. But the shape of a drop on a plane incline at angle  $\alpha$  is the same as that of a bubble on a plane inclined at angle  $\pi - \alpha$ . Thus, the results also include bubble shapes for planes inclined at 120 and 150 deg.

For the computation of bubble volumes, it is convenient to eliminate  $b$  by use of the capillary constant  $a$ , where:

$$a^2 = \frac{2\gamma}{g\Delta\rho}. \quad [45]$$

Let  $V_m$  represent the maximum bubble volume at departure and  $\bar{V}_m$  be the dimensionless volume as computed. Then:

$$V_m = b^3 \bar{V}_m, \quad [46]$$

and

$$V_m / a^3 = \left( \frac{\beta}{2} \right)^{3/2} \bar{V}_m. \quad [47]$$

Shown in Fig. 2 is  $V_m / a^3$  as a function of contact angle for surfaces inclined at 0, 30, 90, and 150 deg with the horizontal.

The surface tension of liquid hydrogen is 2 dynes/cm, while the density is 0.071 gm/cc. Using these values in Eq [45] shows that the normal gravity value of the capillary constant for hydrogen is 0.24 cm. Thus, bubble volumes may be readily computed for hydrogen. After the bubbles depart from the surface, they become spherical. Shown in Fig. 3 are the diameters of spheres of volume equal to the maximum volume at departure as presented on Fig. 2. These data are for normal gravity boiling.

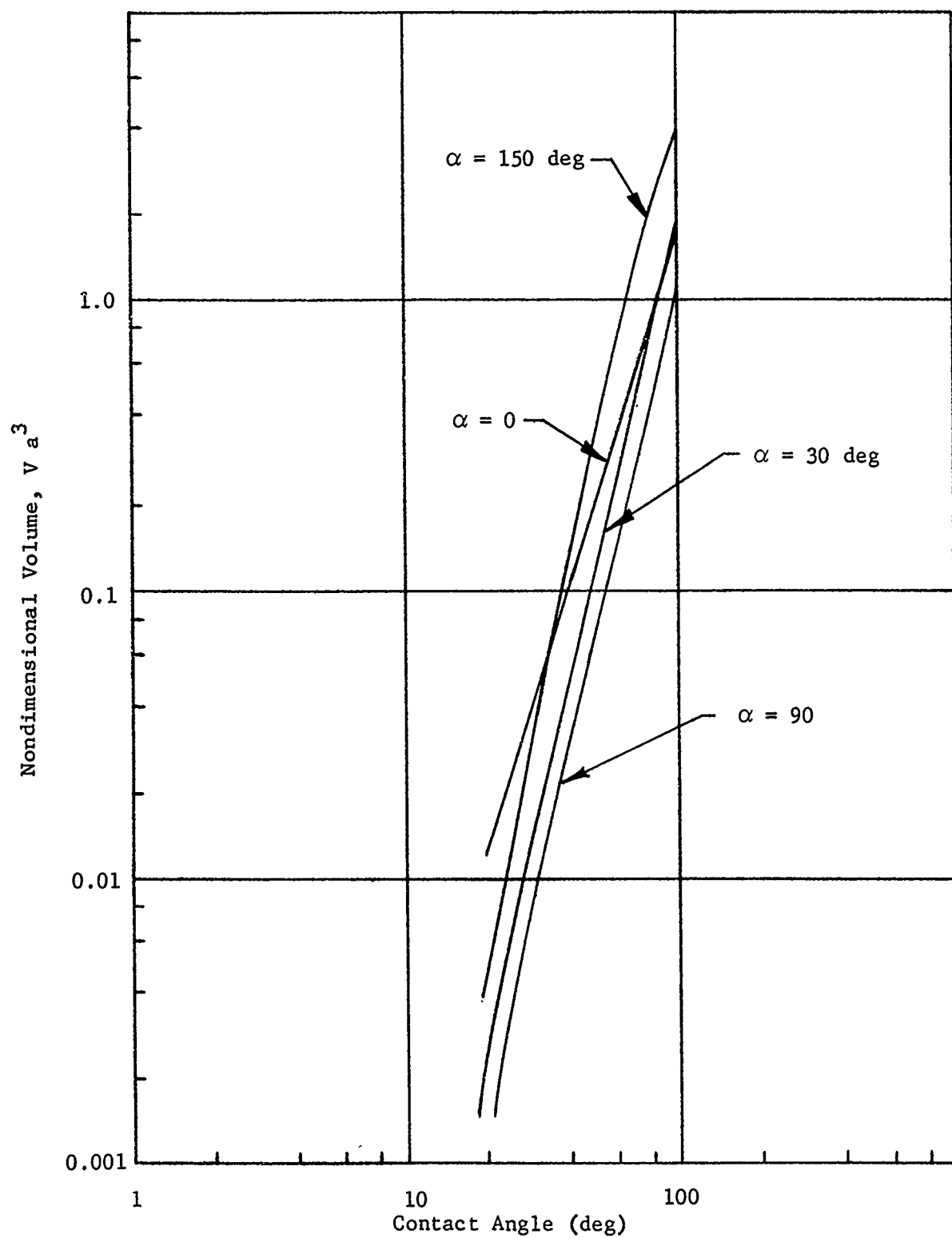


Fig. 2 Dimensionless Volume vs Contact Angle, Normal Gravity

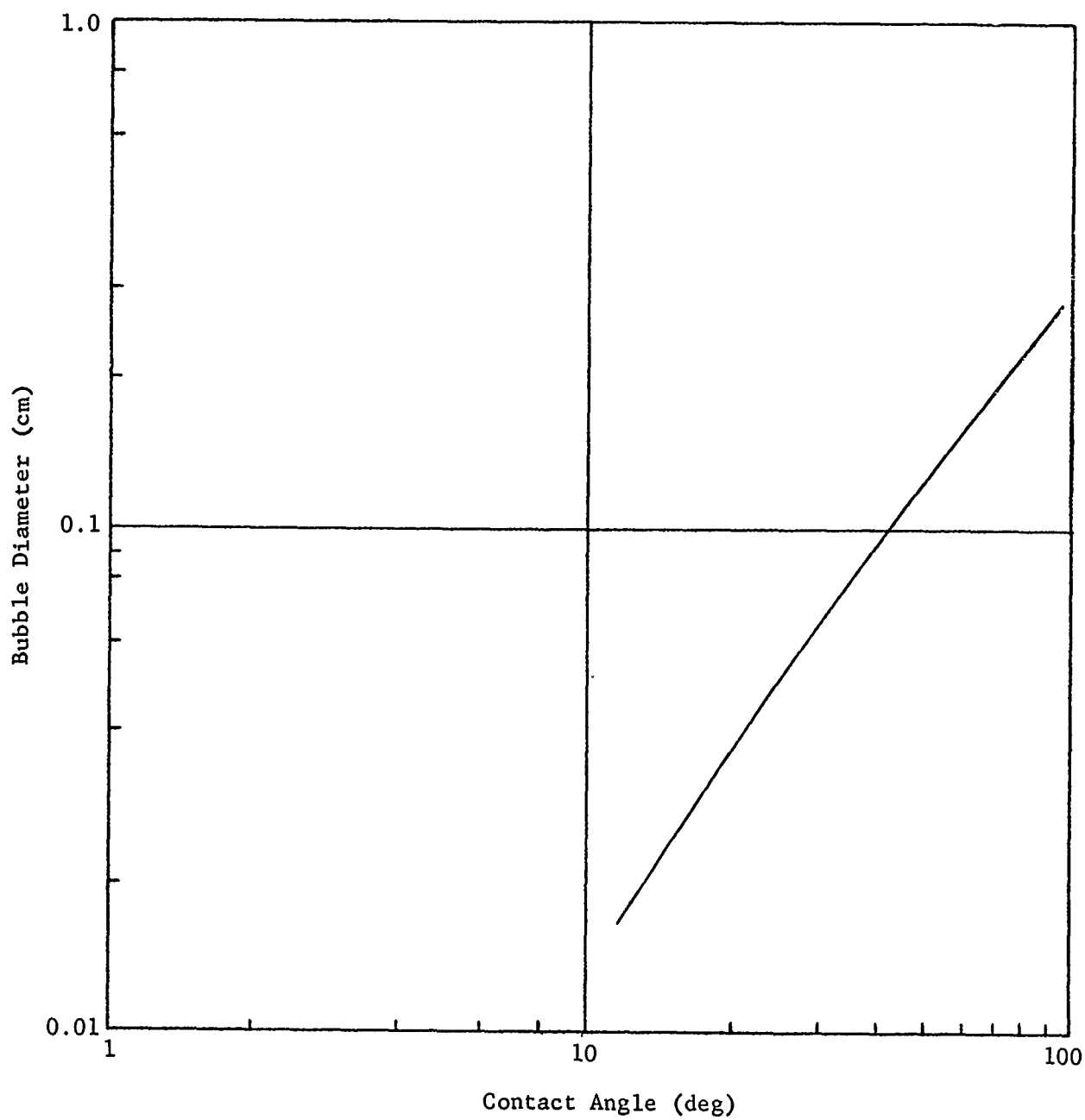


Fig. 3 Hydrogen Bubble Diameter vs Contact Angle, Normal Gravity

High-speed photographs of hydrogen bubbles were taken in this study for normal gravity boiling on a smooth vertical stainless steel surface. These data indicate the bubble diameter to be about 0.03 in. Graham (Ref 19) studied boiling of hydrogen on a horizontal chromel ribbon. By examining the film supplement (Ref 19), the bubbles were estimated to be about 0.03 in. in diameter also.

The photographs, however, are not of sufficient quality to show the contact angle. Thus, it is not possible to predict hydrogen bubble sizes directly from theory. It is possible to force agreement between theory and experiment by assuming the contact angle. From Fig. 3, this contact angle is found to be about 25 deg.

Scaling to low gravity, on the basis of capillarity, is now easy. The theory shows that  $\beta$  is constant which, in turn, implies that all dimensions scale as the minus one-half power of  $|\vec{g}|$ . Figure 4 shows bubble diameters as a function of gravity level for bubbles leaving a vertical surface.

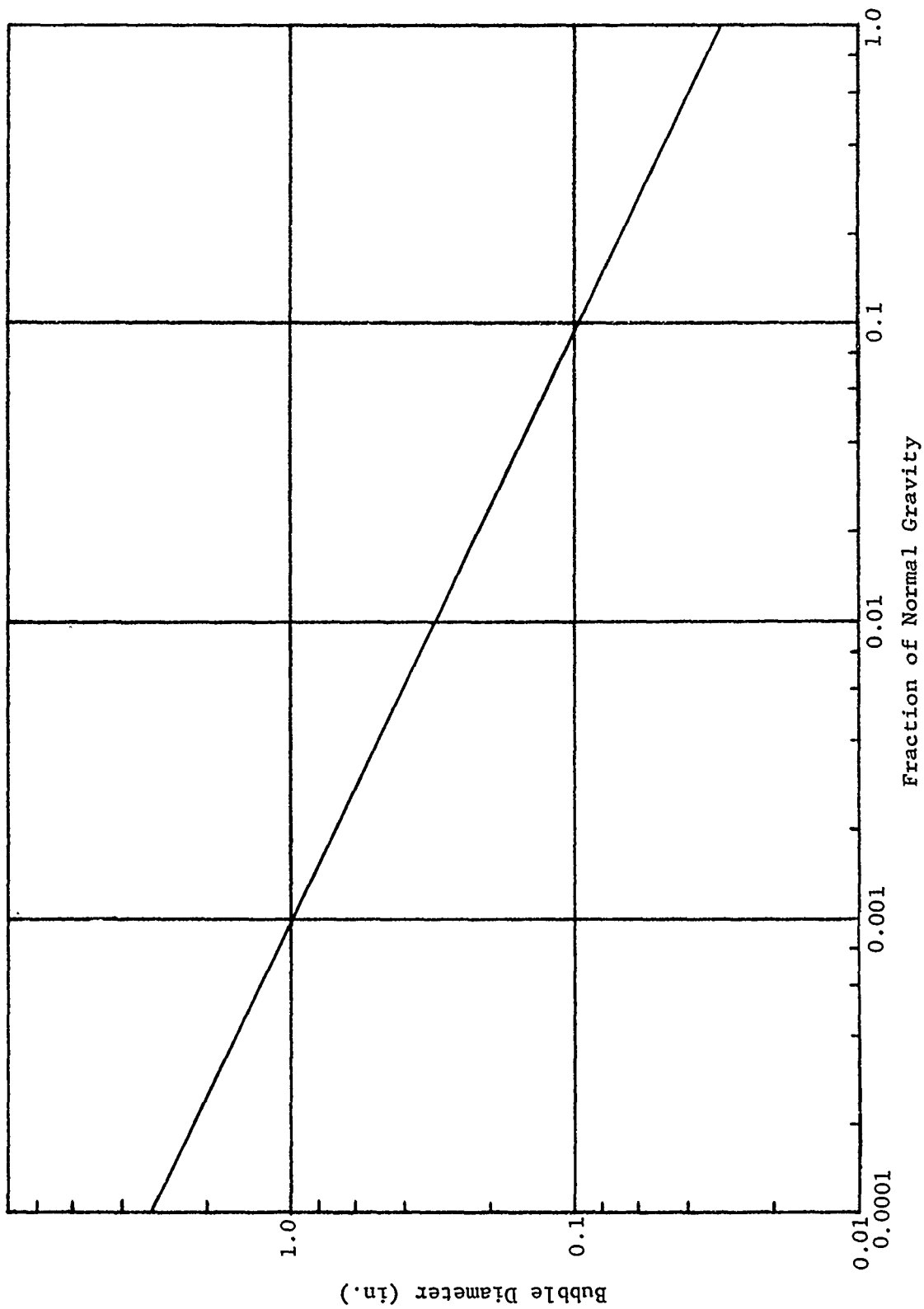


Fig. 4 Hydrogen Bubble Diameter in Low Gravity

## C. EXPERIMENTAL APPARATUS

A series of experiments were conducted both in normal gravity and zero gravity to corroborate the theories presented in previous sections of this report and in some instances to develop data on phenomena which cannot be analyzed by strictly theoretical means.

The apparatus and experimental techniques used in the investigations are described in this section while results obtained are presented in the following section.

### 1. Surface Flow Apparatus and Experimental Procedures

The apparatus and procedures for these experiments were developed to provide visual evidence of the previously discussed theory, i.e., the motion of liquid surfaces under the influence of surface tension gradients. Experiments numbered 1, 2, and 3 were performed to investigate various aspects of Marangoni flow.

Experiment 1 - The apparatus (Fig. 5) consists of a flat glass container placed on a one-half-in. diameter copper rod. A thin film of reagent grade n-butyl alcohol containing Eccospheres\* is placed in the glass container. The copper rod is alternately heated and cooled to produce temperature variations and Marangoni flow on the surface of the liquid film.

In this experiment, we were interested in observing flow at the liquid surface, thus we selected only Eccospheres that float. The spheres on the liquid surface were illuminated with a collimated light source directed at a 45-deg angle to the surface. The particles, which became quite visible, were then photographed to record movements of the liquid surface under the influence of temperature-induced surface tension gradients.

---

\* Eccospheres is the trade name for hollow glass spheres approximately  $10^{-4}$  in. in diameter. The spheres have varying densities due to variations in size and wall thickness. They can readily be sorted according to density by placing a sample quantity of them in the test liquid. The lighter spheres will rise to the liquid surface, the heavier ones will settle out, and some percentage with exactly the density of the liquid will remain suspended. With proper illumination, the spheres can be observed optically thus permitting visualization of liquid flow.



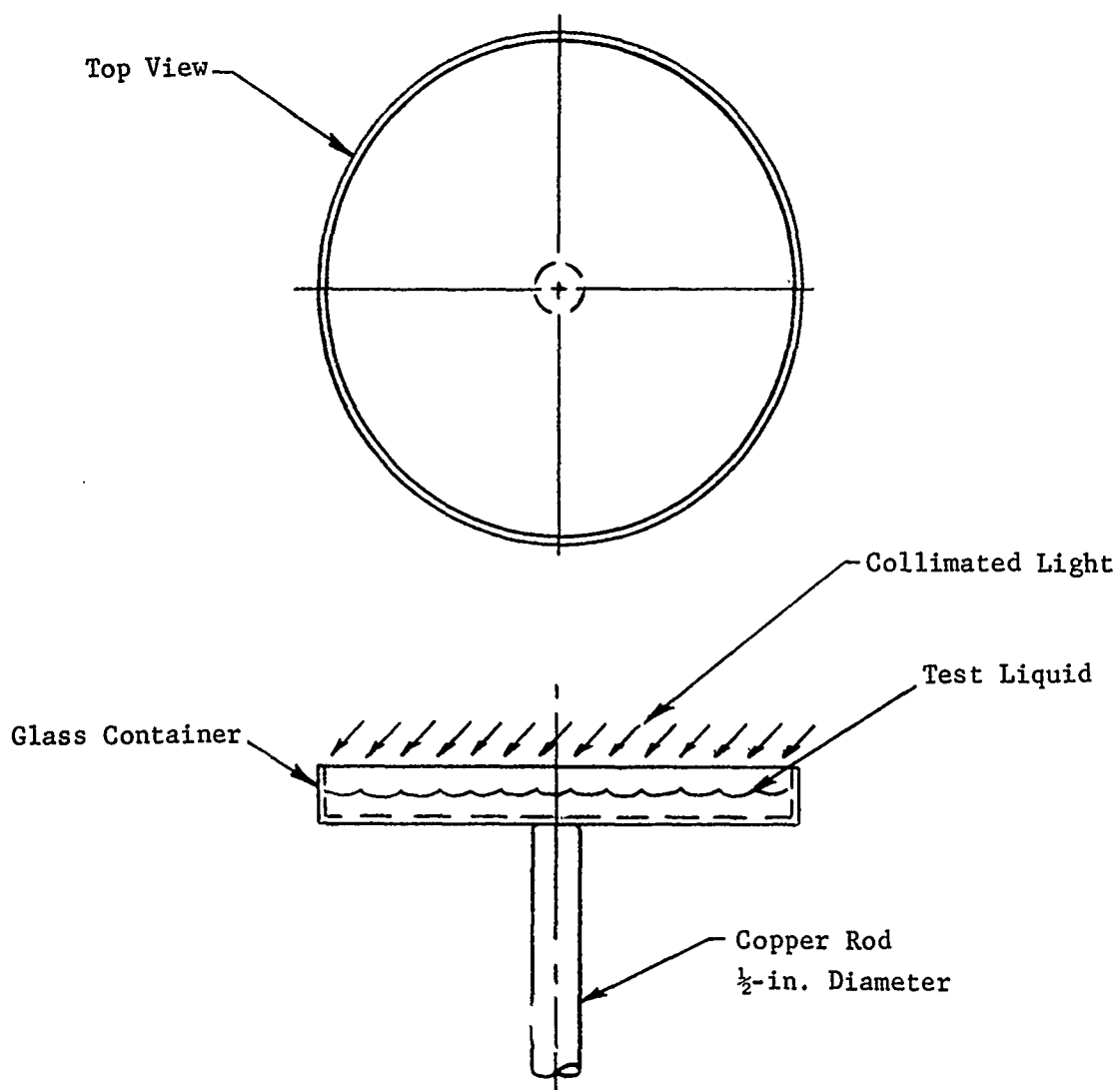


Fig. 5 Marangoni Flow, Experiment 1, Experimental Apparatus

Experiment 2 - This experiment (Fig. 6) uses the apparatus pictured in Fig. 5 with one exception. Two copper rods laid lengthwise across the bottom of the glass container replace the single rod used before. One of these rods was heated and the other cooled. By illumination of the Eccospheres, as explained previously, flow of the liquid surface is observed and photographed.

Experiment 3 - The objective of this experiment is to show qualitatively the liquid deformation resulting from surface flow. To accomplish this the liquid was dyed blue, and a frosted screen was added above the container used for experiment 2. A red light was directed from below (Fig. 6) such that an image of the colored liquid projects onto the frosted screen.

The key to this procedure is the filtering of the red light through the blue test liquid. If the light is directed through a very thin film of the liquid, the image on the screen appears red. The color would change to a yellow-green at medium liquid depth and to a dark blue at the deepest point. Liquid depth is thus indicated by color. The liquid image on the frosted screen is recorded on colored 16-mm film.

## 2. Bubble Thermophoresis

Experimental determination of the thermophoretic force on bubbles was made to corroborate the theory previously presented. In these experiments, measurements were made of the thermophoretic force on bubbles over a range of temperature gradients, liquid properties, and bubble sizes.

Test Theory - The experimental technique used involved suspending the bubble on the free end of a fine cantilevered filament in a pool of nonisothermal liquid. The deflection of the filament due to bubble forces is proportional to the force and is measured by use of a traveling microscope. By measuring the size of the bubble (also with the microscope) and liquid temperatures, the buoyancy force was computed. The thermal component of force was then computed by subtracting the buoyancy component from the net force as indicated by deflection of the filament.

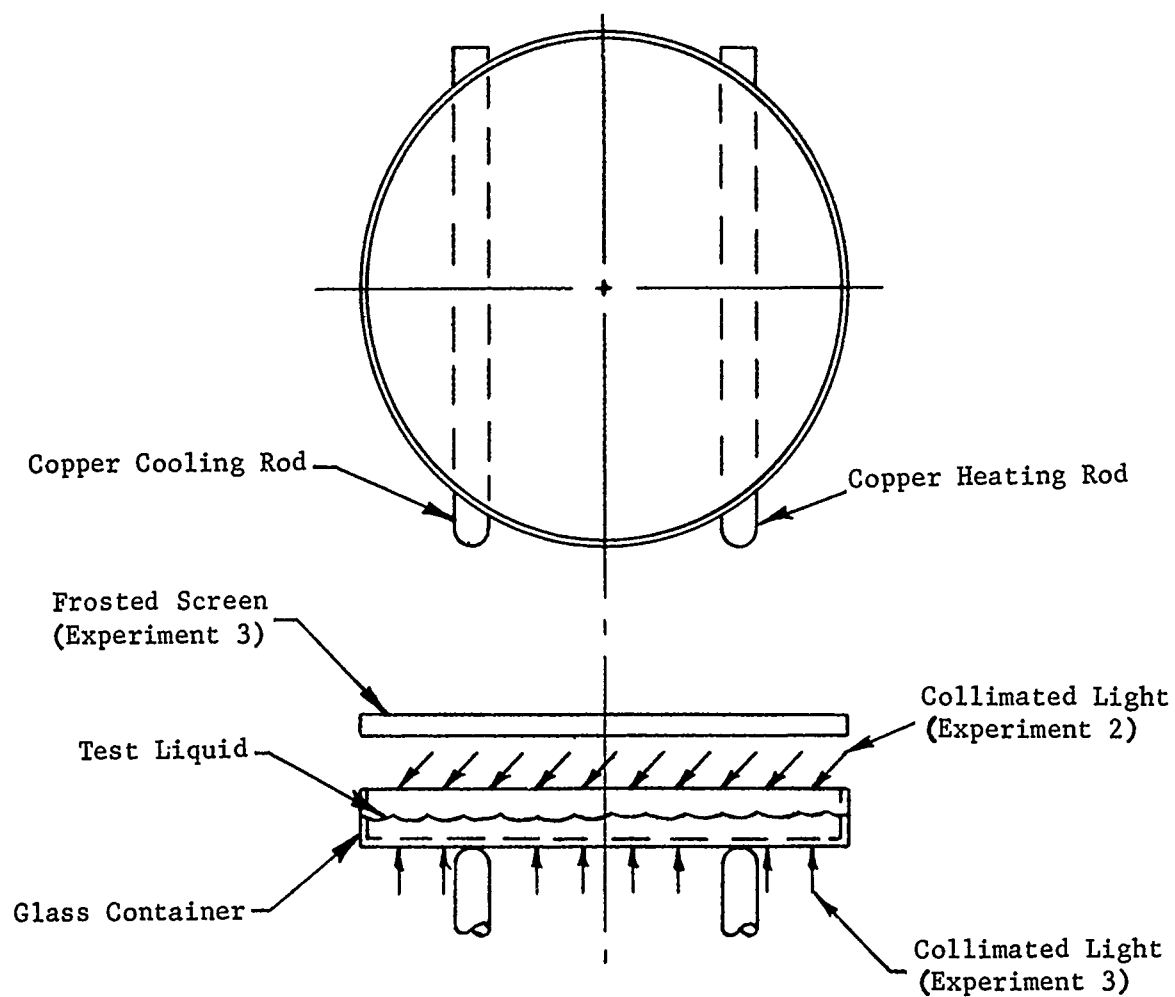


Fig. 6 Marangoni Flow Experiments 2 and 3, Experimental Apparatus

Test Apparatus - The apparatus used (Fig. 7, 8, and 9) consists of a rigid test fixture on which the liquid container and cooling bath are mounted. Three leveling screws in the base of the fixture permit proper alignment during tests. The liquid container is of phenolic material with two plexiglass ports. One of these ports was used to introduce collimated light -- the other to view and photograph results (Fig. 8). Observations were made through the viewing port by the traveling microscope that is equipped with a vernier scale with accuracy to 0.001 cm. The aluminum bottom plate of the liquid container had a fin extending downward into a cooling bath. The bath was filled with an ice and water mixture.

A 35-watt electrical heater was mounted on an adjustable stand (Fig. 7 and 9) for ease of obtaining the appropriate test liquid depth (0.2 to 0.8 cm). Thermal response of the test liquid to cooling and heating is analyzed in Appendix B.

Temperatures were measured by thermocouples imbedded in the heating and cooling surfaces and by thermocouple probes (Fig. 7). The thermocouples were connected through a selector switch to a hand balanced pyrometer.

The test liquids were reagent grade n-butyl alcohol and methanol with Eccospheres suspended by the method previously described.

The test liquids were reagent grade n-butyl alcohol and methanol with Eccospheres suspended by the method previously described. Fluid properties are given below:

Liquid	T (°C)	$\rho$ (g/cc)	$\gamma$ ( $\frac{\text{dynes}}{\text{cm}}$ )	$\frac{d\gamma}{dT}$ ( $\frac{\text{dynes}}{\text{cm}^\circ\text{C}}$ )	Vap Press (mm Hg)
n-Butyl Alcohol	0	0.823	26.2	0.080	--
	20	0.810	24.6		4.4
	40	0.796	--	0.083	18.6
	50	0.790	22.1		
Methanol	0	0.810	--	0.083	--
	20	--	22.6		95.3
	30	--			155.0
	40	--			257
	50	--	20.1		--
	64.7	--	--		760.0

The bubble, produced by a hypodermic needle, was held in place by a small wire device as shown in Fig. 10. Three fine "fingers" held the bubble with a minimum of contact such that liquid flow was disturbed as little as possible. The bubble holder was attached to the end of the cantilevered wire mentioned previously. Desired characteristics of the wire were determined by analysis (Appendix B). The wire, a tungsten-boron filament, was calibrated and found to be very repeatable. Other materials were tried but were discarded due to hysteresis and nonrepeatability. Final calibration of the force measurement system is shown in Fig. 11.

During some experiments, liquid flow patterns were observed by use of the suspended Eccosphere technique previously described. Still photographs and 16-mm movies were taken of the flow patterns.

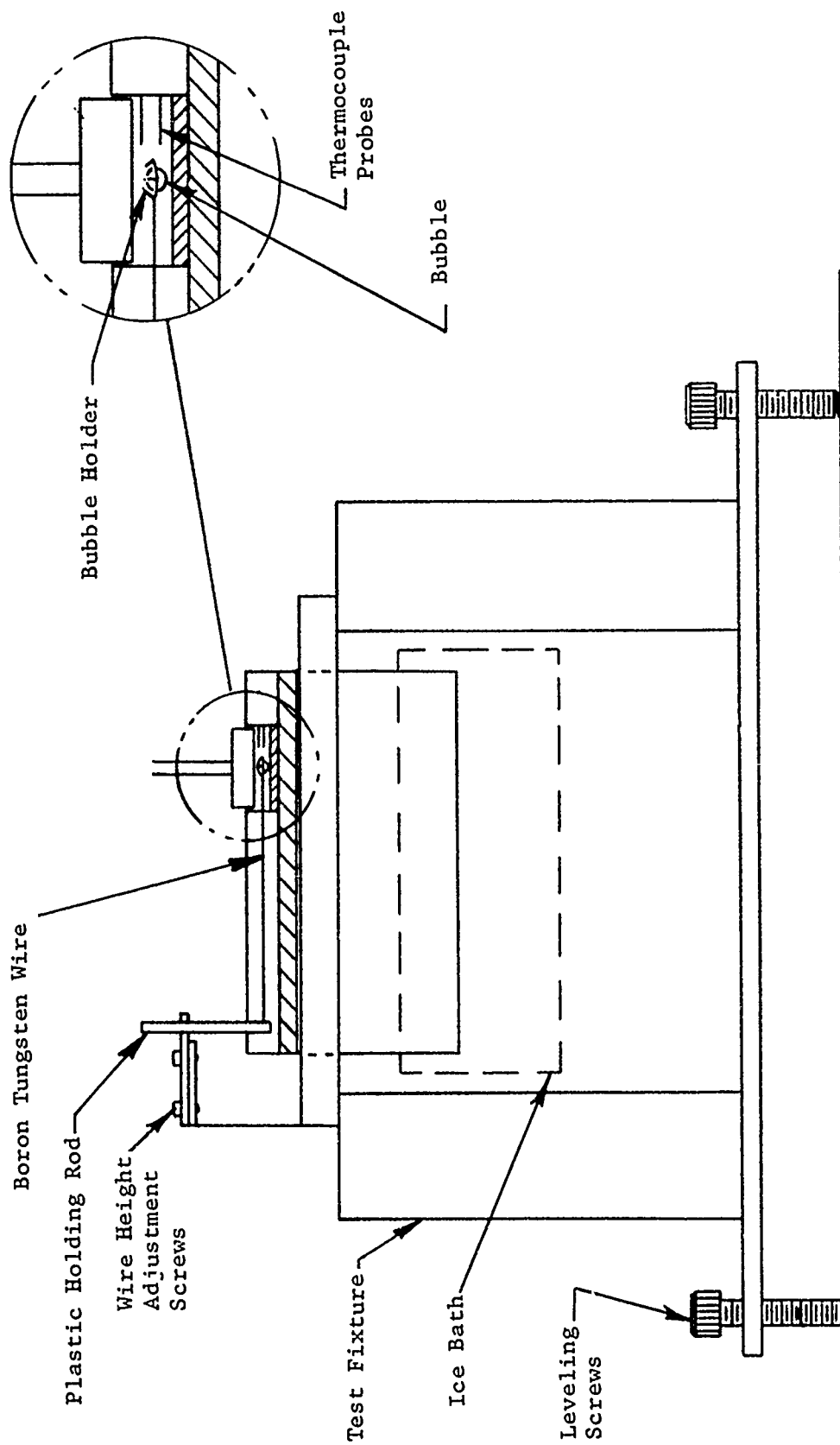


Fig. 7 Bubble Thermophoresis Experimental Apparatus

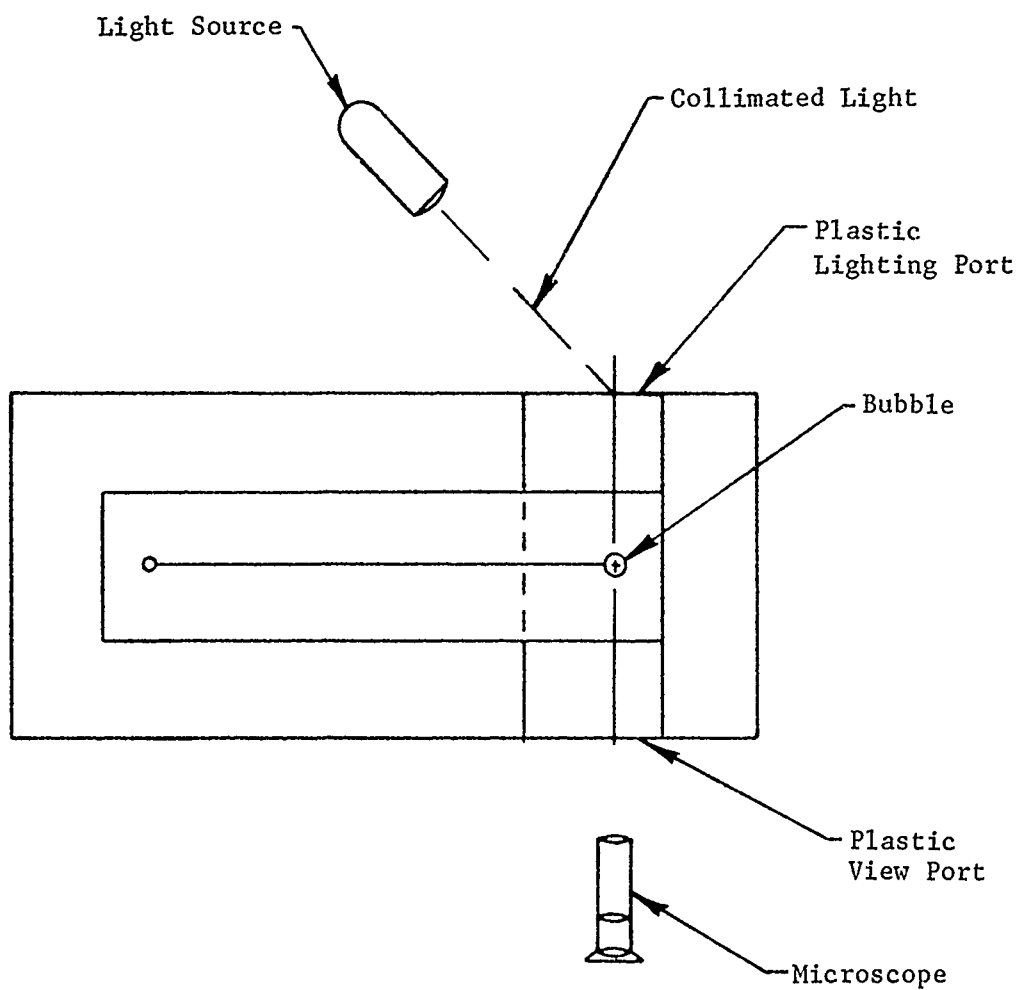


Fig. 8 Bubble Thermophoresis Lighting and Viewing Schematic

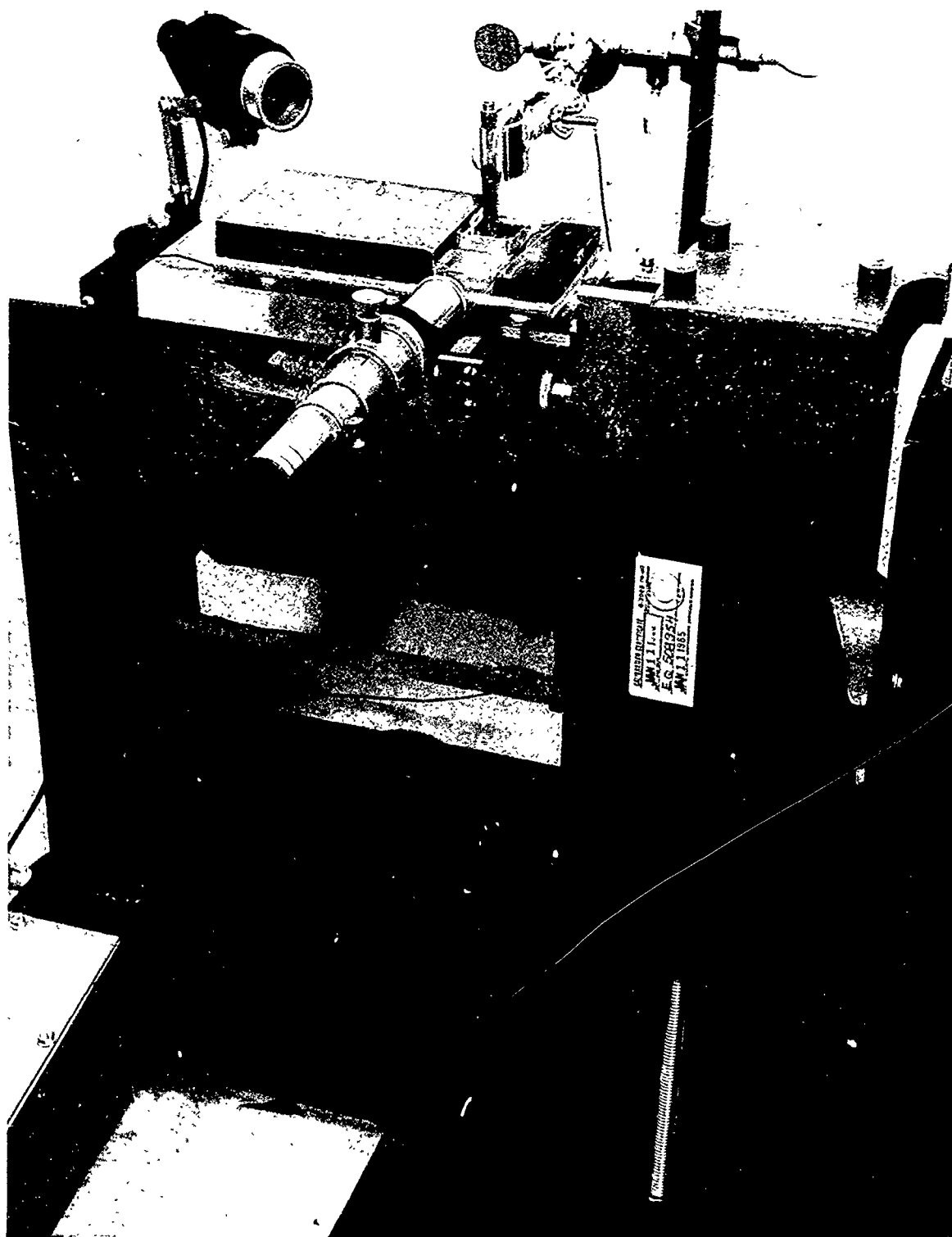


Fig. 9 Bubble Thermophoresis Experimental Apparatus (without bubble holder)

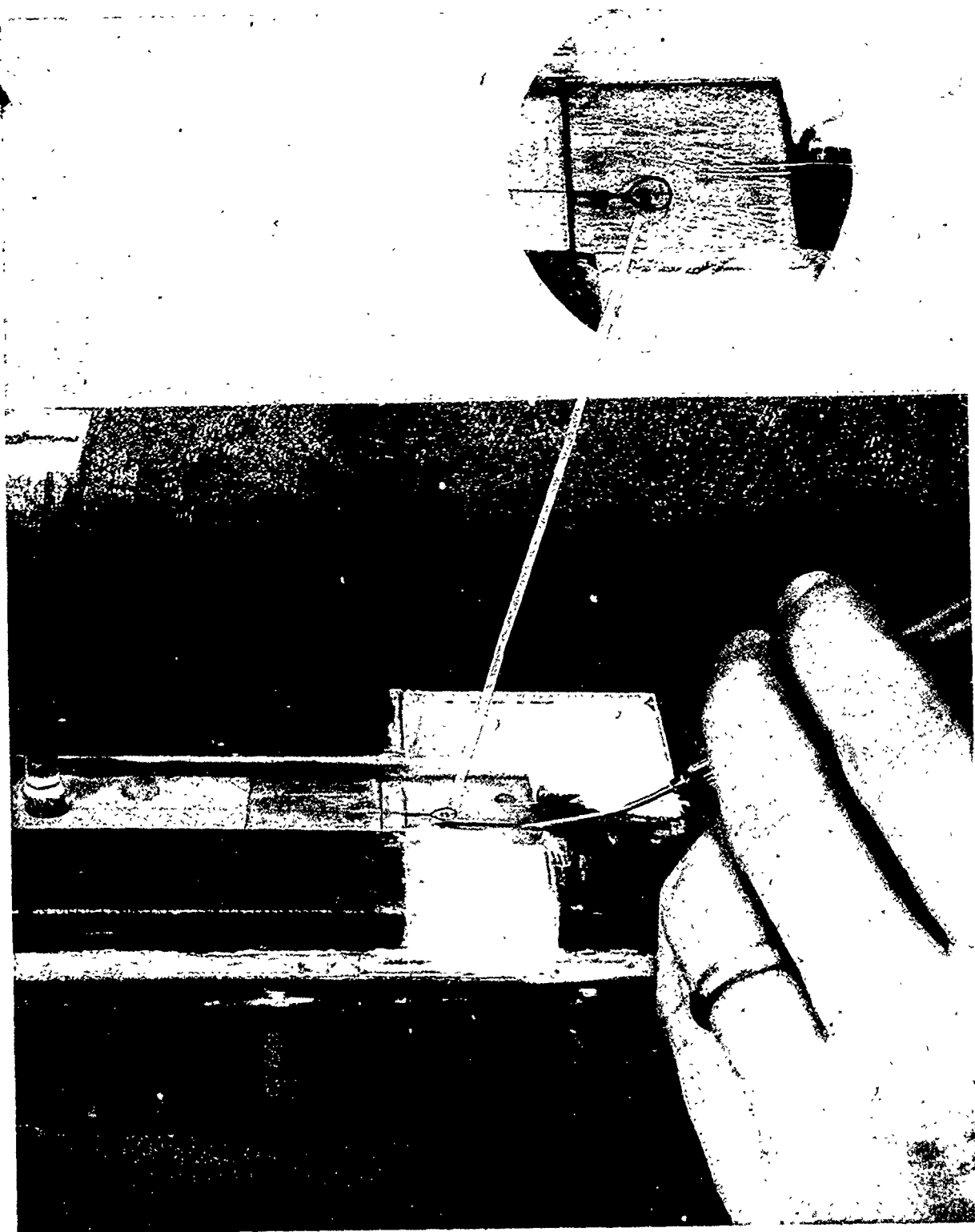


Fig. 10 Bubble Force Experiment Bubble Insertion Technique  
(Expanded View: Bubble Holder and Thermocouple Probes)



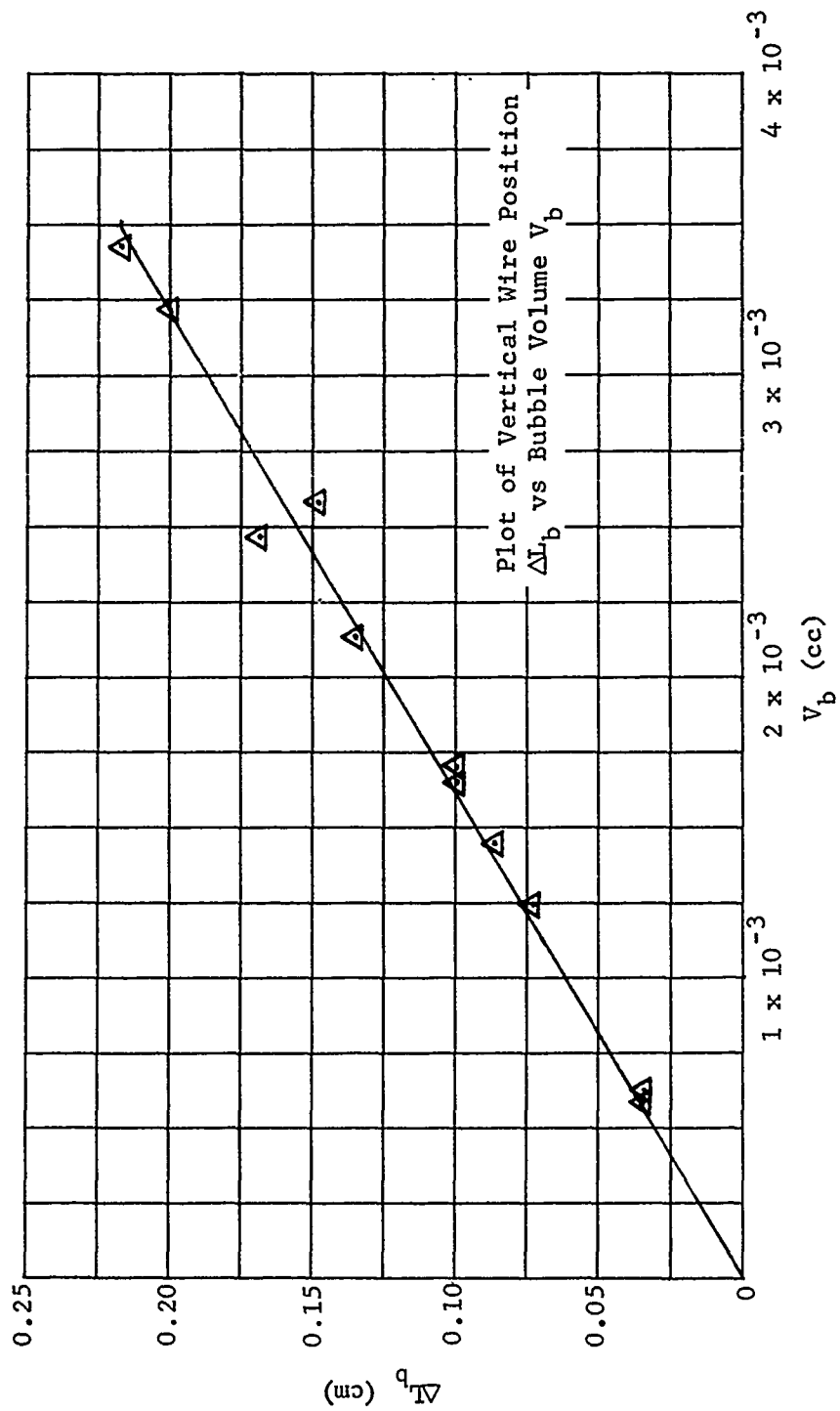


Fig. 11 Boron Tungsten Wire Calibration

Experiment Procedure - The liquid container was filled with the appropriate test liquid and a bubble was placed in the holder by use of the hypodermic needle. A rough check of the bubble size was made with the microscope, and if it were not the desired size, the bubble was repeatedly replaced until the appropriate size was obtained. The position of the bubble was adjusted, by use of the adjustment screws, to coincide with the center of the test liquid. The heater was then carefully put in place and adjusted for elevation. The experiment was started by filling the ice bath and energizing the electrical heater. Bubble size, wire deflection, and liquid temperatures were monitored and recorded. The experiment was terminated when predetermined liquid temperatures were reached. By using the data analysis technique previously described, the thermophoretic force is determined and the term  $\psi$  (thermal force/buoyancy force) is computed. For data presentation, the  $\psi$  term is normalized for bubble size by multiplying  $\psi$  by bubble radius ( $r$ ). The normalized term ( $\psi r$ ) is plotted as a function of temperature gradient.

Following some of the experiments, Eccospheres were placed in the liquid in the vicinity of the bubble, and photographs and movies of the liquid flow were taken.

### 3. Marangoni Flow around Bubbles

The liquid flow patterns around a suspended bubble were observed and recorded as previously discussed. In addition, flow and temperature patterns were recorded for the situation of air and vapor bubbles on a heated surface. The experimental apparatus used (Fig. 12) was the same as that used for the thermophoresis experiments, except that the wire and bubble holder were removed, and the bubble was placed directly on the heater surface. Flow patterns were recorded using the suspended Eccosphere technique. Temperature patterns were observed using the direct shadow photography technique. A shaft of collimated light was directed through the test liquid at right angles to the parallel view ports. The refraction patterns were then focused on a movie film using a parabolic mirror and a lens system.

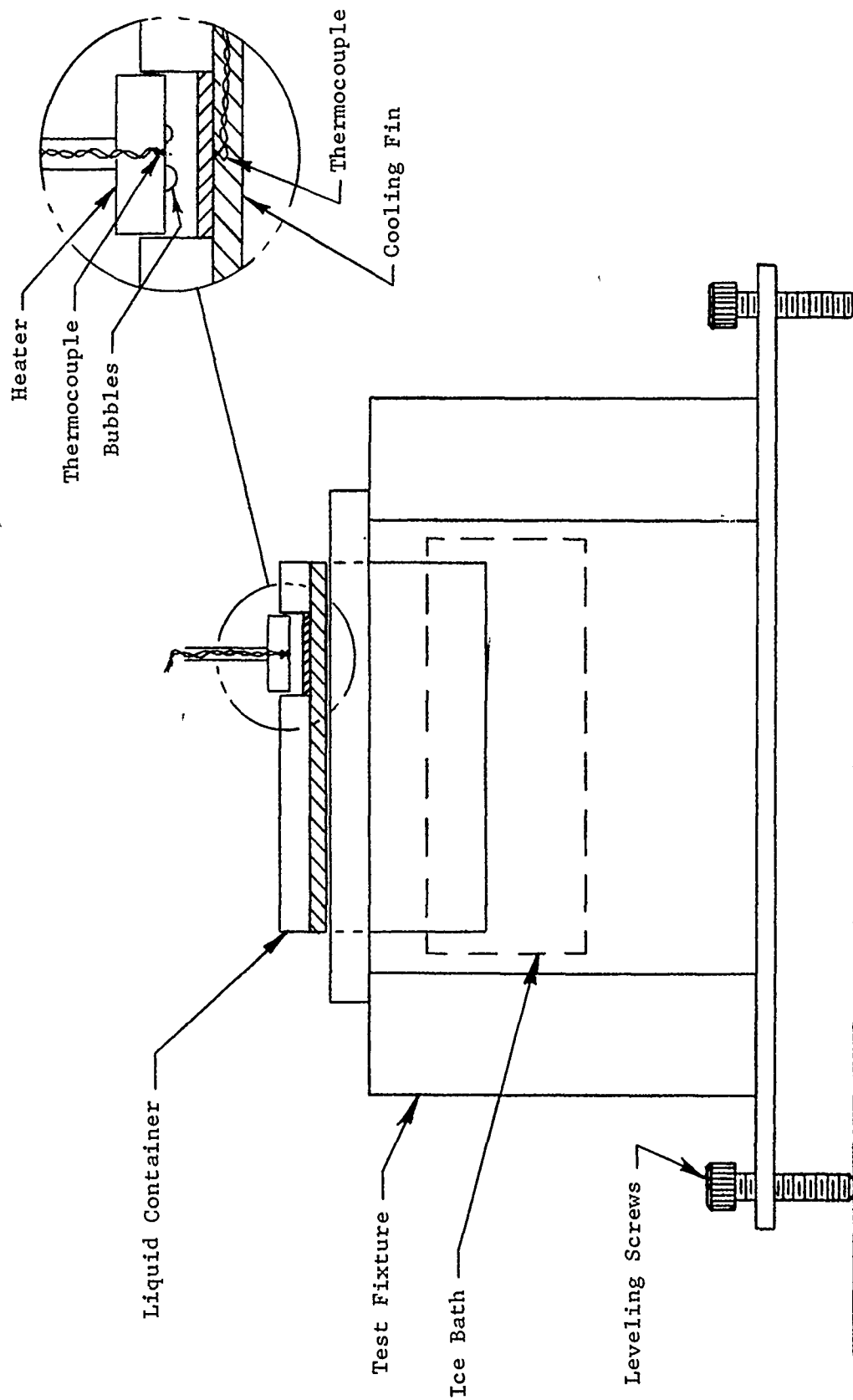


Fig. 12 Bubble on a Heated Surface Experimental Apparatus

#### 4. Boiling

Because of the complexity of the boiling process, theoretical results are not adequate for predicting behavior in low gravity. Thus, an experimental program was necessary to supplement the theory. To provide a basis for the experimental phase, comparison tests were run in both normal and zero gravity. Experimental studies were made of the formation and growth of hydrogen bubbles in both normal and zero gravity. Two types of zero-gravity experiments were performed. In one type, the boiling was initiated in normal gravity. Following a few minutes of such boiling, the experimental package was released, and during 0.8-sec free-fall time, the boiling in zero gravity was observed. In this type of experiment, the influence of the transition from normal to zero gravity on boiling could be observed. In the second type of experiment, the nucleation heat was applied after the experimental package had been released. Many investigators fear that the existence of convective boundary layer flow prior to free fall might adversely influence the bubble growth in zero gravity. This difficulty is circumvented by the second series of tests, since the liquid was quiescent prior to release.

Boiling was effected by the apparatus shown in Fig. 13 and 14. Bubbles were formed at an imperfection in the center of a highly polished stainless steel surface. This surface was the flat side of a disk 11/16 in. in diameter and 1/2-in. thick. Surrounding the stainless steel disk is a Teflon disk as Fig. 13 shows.

As a dimensional reference, a 1/32-in. diameter wire, fastened at the back of the disk, stands 1/4 in. in front of the test surface. Drilled into the stainless steel disk is a 1/4-in. diameter hole which contains a nichrome heater. This nichrome heater is sharpened to a needle point and is pressed against the back of the polished surface by a coiled spring. Electrical current flow is through the upper heater wire, the fastening screw, the stainless disk, the nichrome needle, and back through the lower heater wire. Since the contact point between the stainless steel surface and the nichrome needle represents the greatest electrical resistance in the heater circuit, the contact point is also the heat source. Epoxy resin fills the annular space between the nichrome needle and the stainless steel disk.

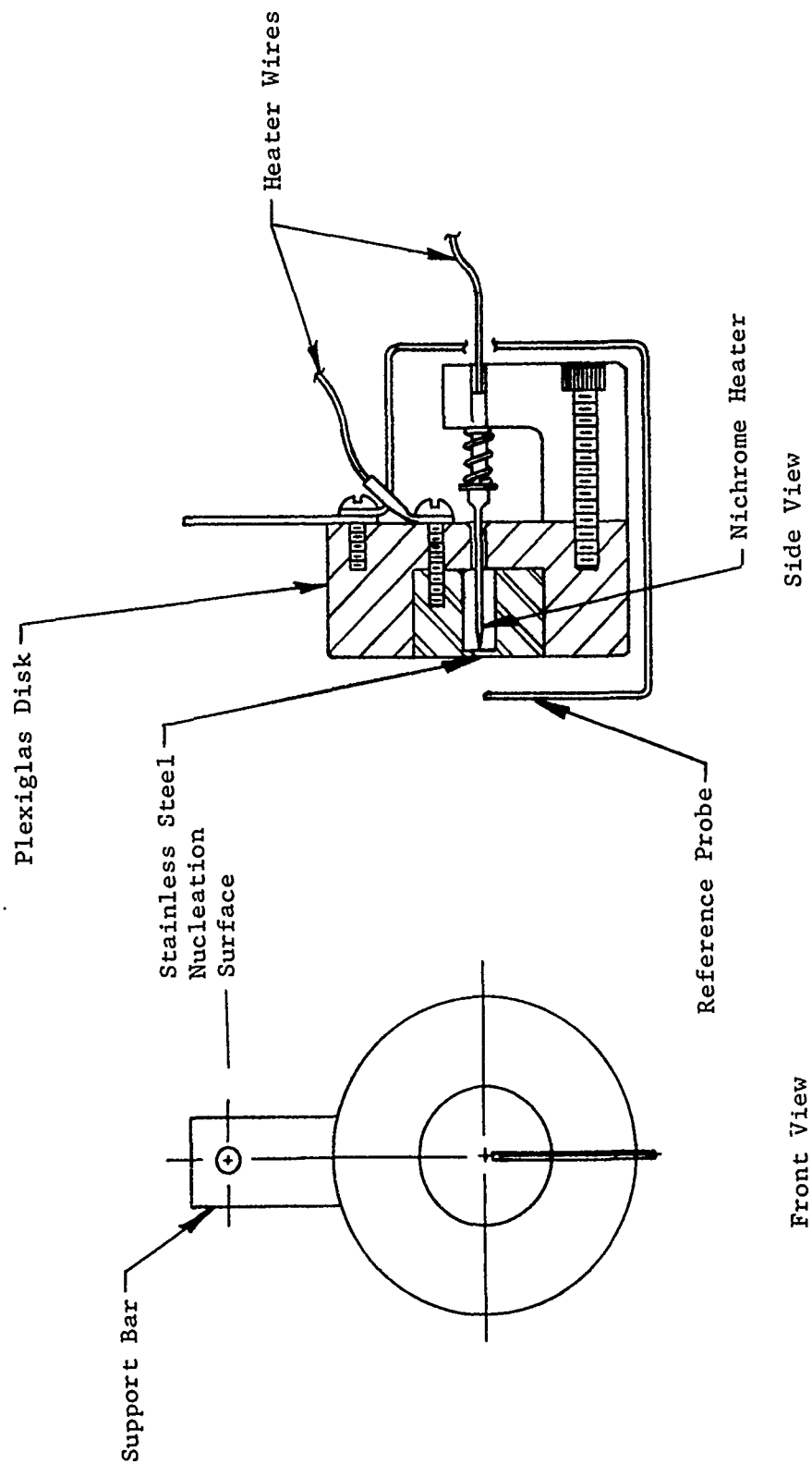


Fig. 13 Boiling Apparatus

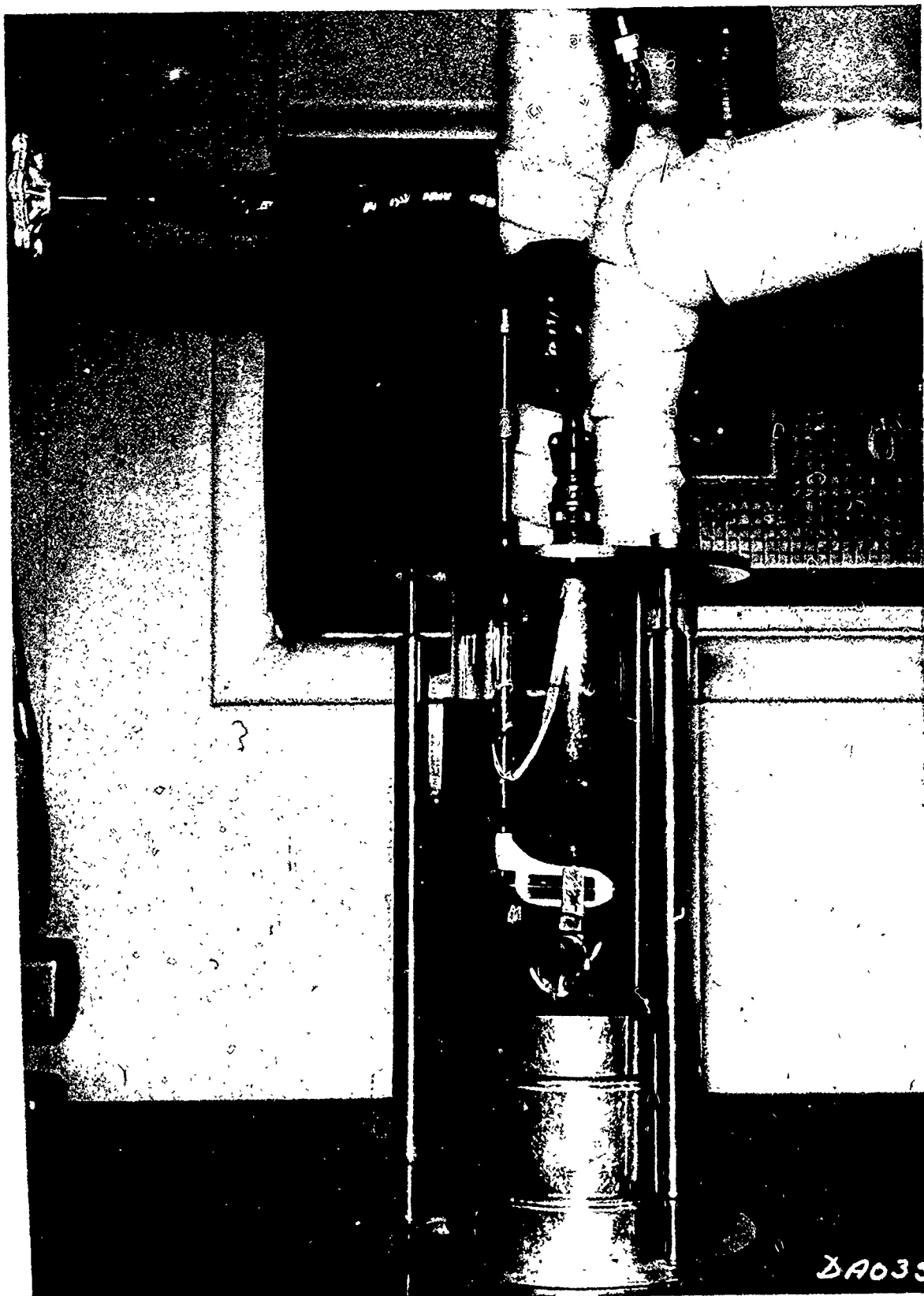


Fig. 14 Photograph of Boiling Apparatus

The boiling apparatus was hung from the lid of a 4-in. glass dewar. Sideviews were taken of the bubbles with a 16-mm Milliken camera, type DB IV. Kodak tri-x negative film was used at a rate of 400 frames per sec. A single 250-watt sun gun provided illumination. To diffuse the light, a piece of opal glass was located outside the dewar and between the light source and test surface. Because the camera view was from the side, the camera axis makes an angle of 90 deg to the normal of the stainless steel surface. The sun gun illumination was aimed to make a 45-deg angle with the normal to the stainless steel surface.

Figure 15 is the drop capsule schematic. All equipment to the right of the dashed line is contained within the drop capsule. Prior to conducting a test, it is established that the potential gradient is within safe limits for handling liquid hydrogen. After connecting the transfer line between the test dewar and the 1000-liter storage dewar, the valves shown in Fig. 15 are set as follows:

- ① closed;
- ② closed;
- ③ closed;
- ④ open;
- ⑤ open.

To fill the test dewar, we first open ① and ② to purge the transfer line. Later, ③ is opened and ② is closed to admit hydrogen to the system. When the test dewar is full, ③ is closed, ① is closed, ② is opened, and ④ is closed. The transfer line is removed, and the capsule is connected to the tower hoist and raised to the top of the tower. From the control console, we close ⑤. Power is applied to the heater surface, the sun gun, and the camera motor. When the pressure in the dewar reaches 5 psig, the hydraulic cutting block is actuated to sever the wire which holds the capsule. After the capsule strikes the wheat bin, we open ⑤, and disconnect the heater, sun gun, and camera motor. In those runs in which heat was applied in zero gravity, a wire, terminated by an alligator clip, was connected between the cutting block and capsule. After the capsule had dropped about 6 in., the alligator clip pulled loose from the capsule, and this action energized the heater circuit.

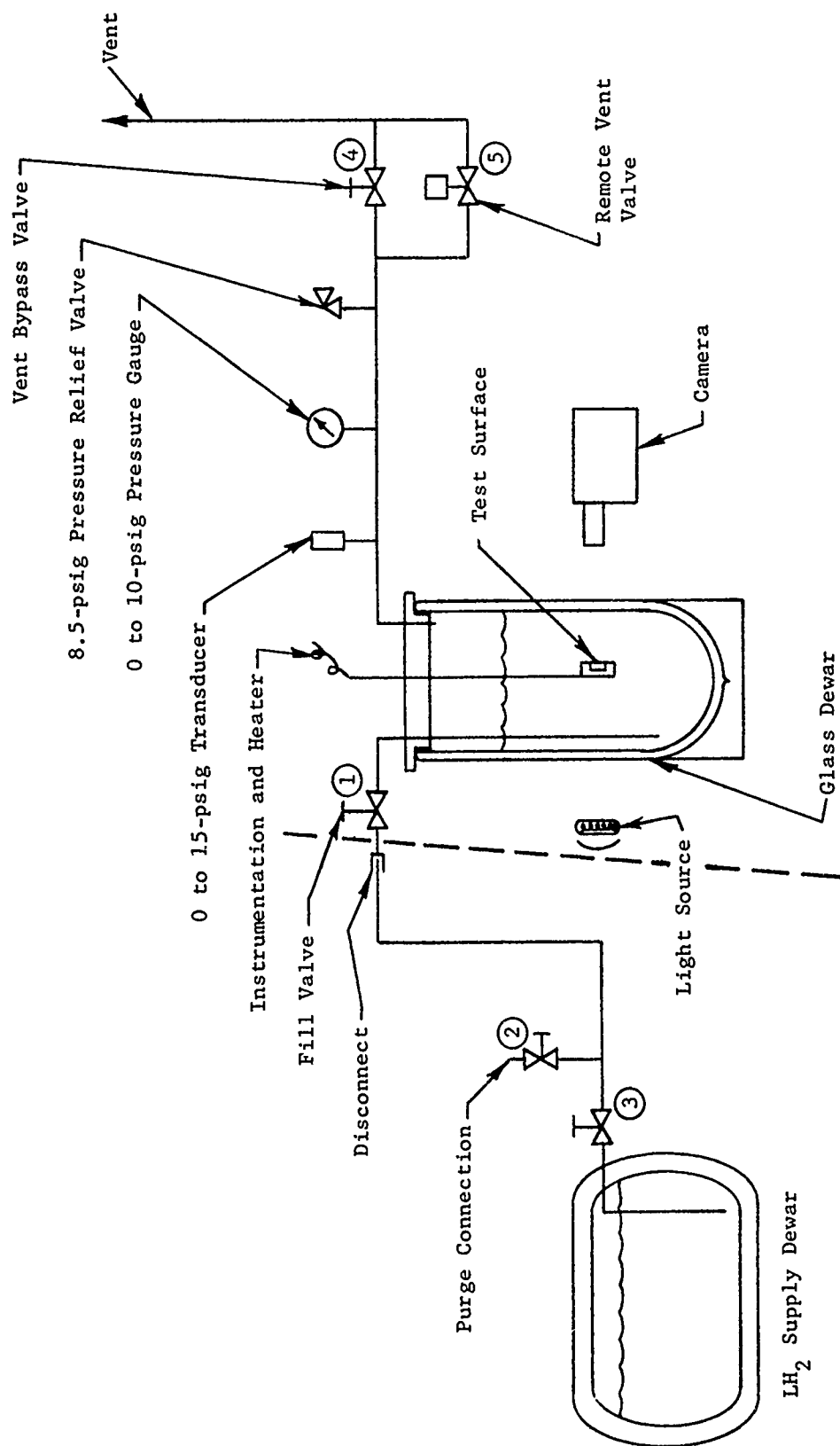


Fig. 15 Drop Capsule Schematic



## D. EXPERIMENTAL RESULTS AND CONCLUSIONS

### 1. Surface Flow Phenomena

Using the experimental apparatus previously described, several surface flow experiments were conducted. The results of the experiments are qualitative in nature. The flow of the surface under the influence of surface tension gradients was photographed with the movie camera. Figures 16 and 17 are successive frames of the film. Figure 16 shows that when the copper rod was heated, the surface of the liquid flowed away from the heated center. The temperature gradient across the liquid surface was approximately  $15^{\circ}\text{C}/\text{cm}$ , and the flow velocity at the liquid surface was approximately  $1/2 \text{ cm/sec}$ . When the copper rod was cooled rather than heated, the direction of surface flow was reversed as shown in Fig. 17. With heating, liquid flowing away from the center caused a depression to form in the liquid over the rod. Cooling, on the other hand, resulted in an increase in liquid depth over the copper rod.

Results obtained from the experiments in which liquid was simultaneously heated and cooled (Fig. 18) are similar to those discussed above. In all cases, the liquid flowed from the hot rod toward the cool rod causing a depletion of liquid in the hot region and an accumulation in the cooler region. Temperature gradients on the order of  $4^{\circ}\text{C}/\text{cm}$  were obtained in these experiments, and surface liquid velocities of approximately  $1 \text{ cm/sec}$  were observed. Successive frames of the data movie are shown in Fig. 18. Color movies of the liquid deformation due to surface flow show that liquid always moved away from the hot region when a temperature gradient existed.

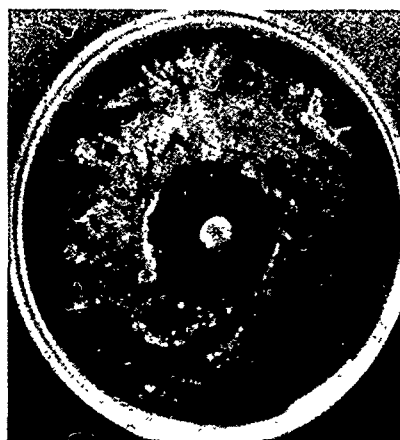
Experimental results show that liquid flows in a direction of decreasing temperature under the influence of surface tension gradients at a liquid/vapor interface.

### 2. Bubble Force Experiments

The bubble force apparatus discussed previously was used for experimental determination of the magnitude of the thermophoretic force. Using the previously described test procedure, experiments were conducted over a range of bubble sizes and temperature gradients. Test liquids were reagent grade n-butyl alcohol and methanol. Test results are shown in Fig. 19 and 20.



T - 0



T + 1



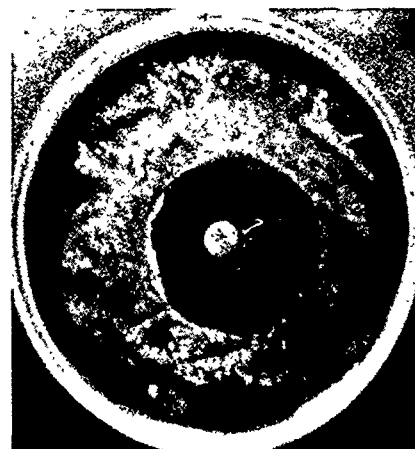
T + 2



T + 3



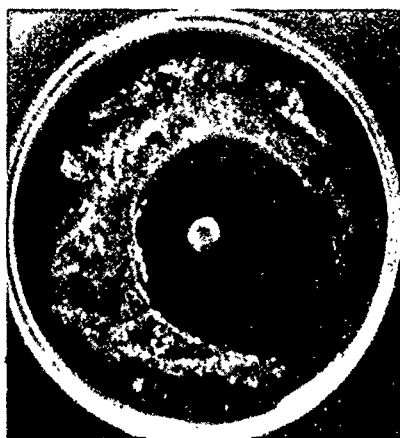
T + 4



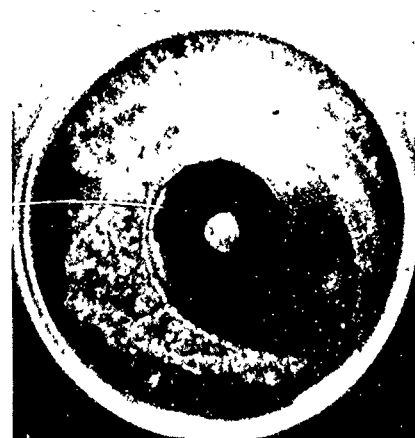
T + 5



T + 6



T + 7



T + 8

Fig. 16 Marangoni Flow (Flow Away from Heated Center Rod, sec),  
Experiment 1 (Test Liquid, n-Butyl Alcohol)



T - 0



T + 1



T - 2



T + 3



T + 4



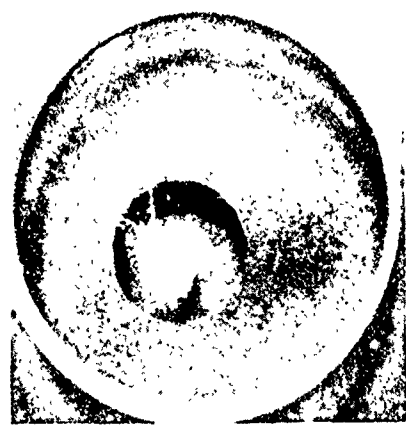
T + 5



T + 6



T + 7



T + 8

Fig. 17 Marangoni Flow (Flow Toward Cooled Center Rod, sec), Experiment 1 (Test Liquid, n-Butyl Alcohol)



T + 0



T + 1



T + 2



T + 3



T + 4



T + 5



T + 6



T + 7

Fig. 18 Marangoni Flow (sec), Experiment 2 (Test Liquid, n-Butyl Alcohol)

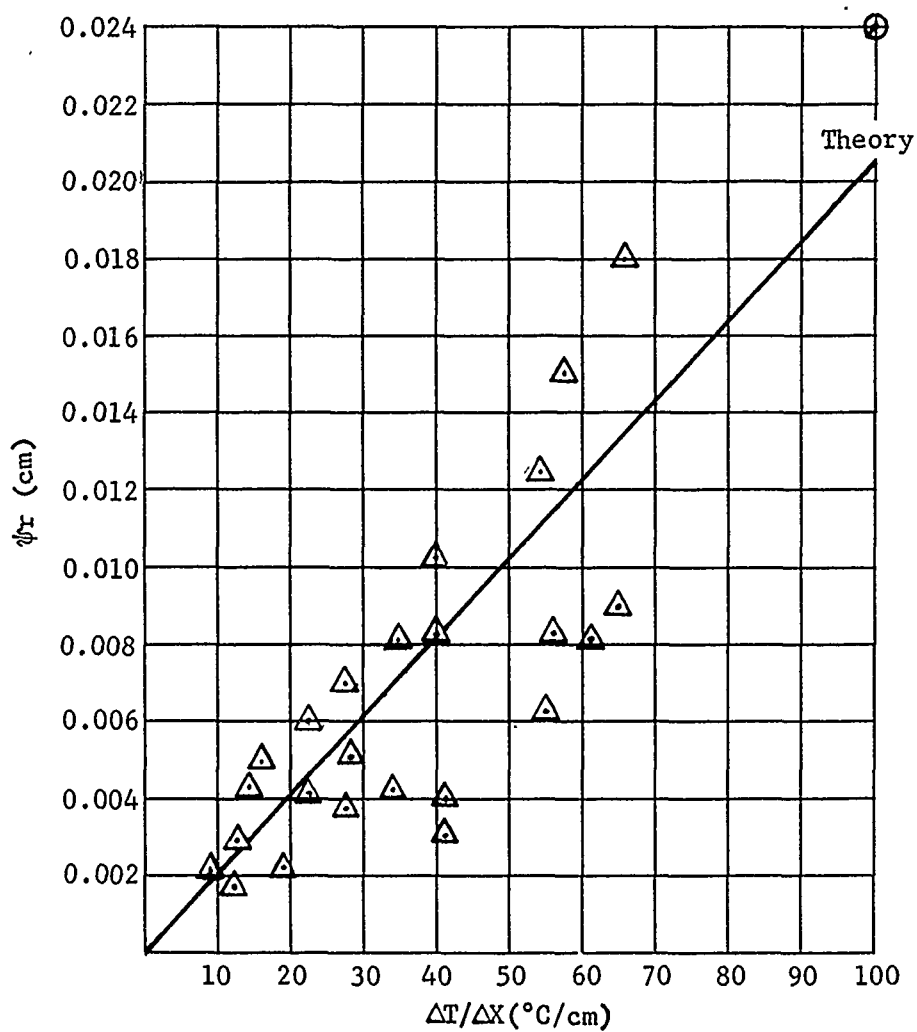


Fig. 19 Bubble Force Parameter vs Liquid Temperature Gradient (Test Liquid, n-Butyl Alcohol)

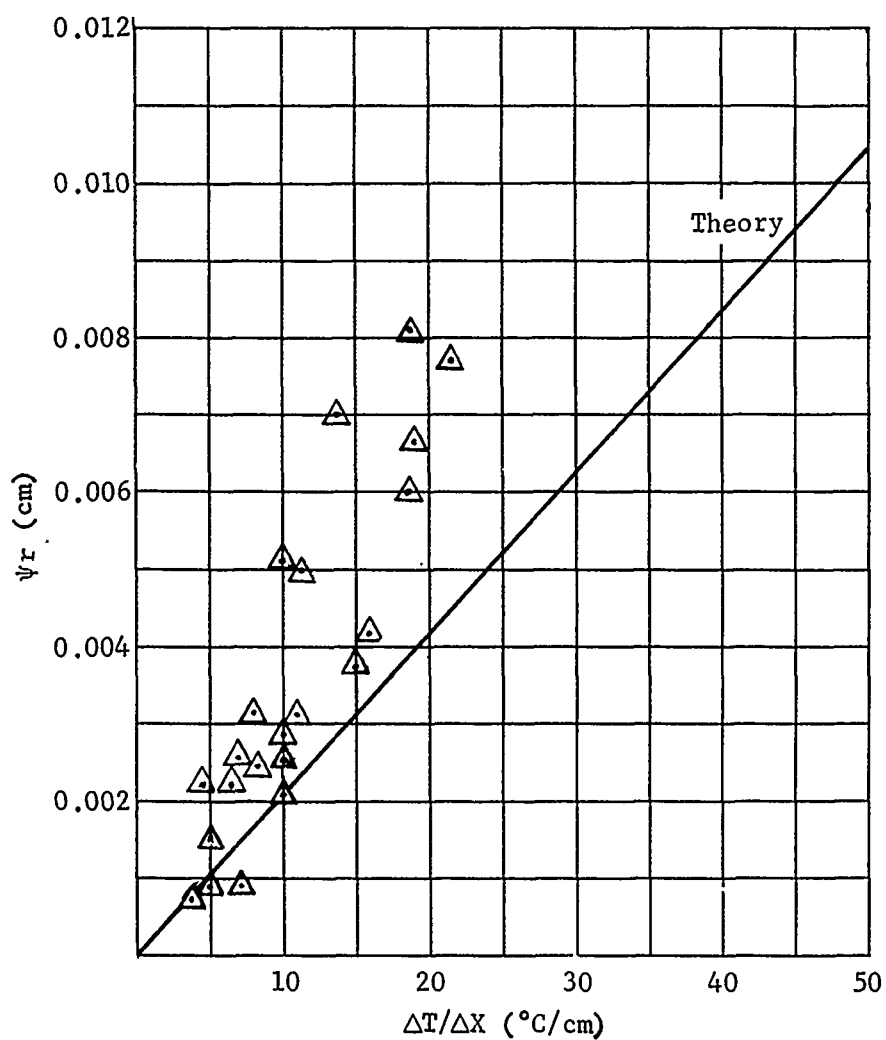


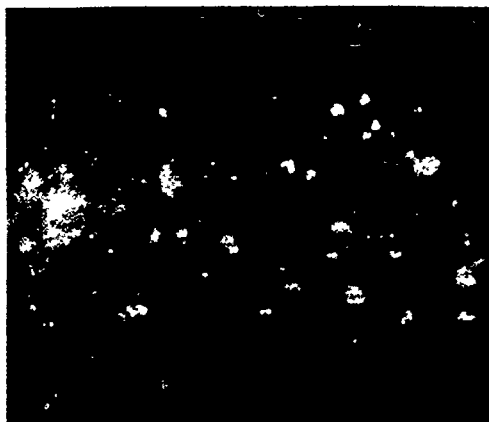
Fig. 20 Bubble Force Parameter vs Liquid Temperature Gradient  
(Test Liquid, Methanol)

As can be seen in Fig. 19, the data for n-butyl alcohol falls on both sides of the theoretical prediction [11], whereas with methanol (Fig. 20), the data falls on and above the theory. These results are readily explained by two factors. First, as previously discussed, the temperature gradient in each experiment is measured by means of two thermocouples in the liquid close to, but not on, the bubble surface. As previously discussed, surface flow caused by surface tension gradients results in considerable thermal mixing in the vicinity of a bubble. The greatest liquid velocities occur at the bubble surface, thus, the greatest degree of thermal mixing occurs there, and the temperature gradients tend to be somewhat lower than in the bulk of the liquid. Because of the mixing effect, then, the actual temperature gradient at the bubble surface tends to be lower than that which is recorded. In general, if the test were conducted very quickly, better agreement between experiment and theory would be obtained. The second factor to consider is the vapor pressure effect discussed previously which is not included in the theoretical predictions. The vapor pressure of n-butyl alcohol is negligible under the test conditions and thus plays no significant role in the thermophoretic force. On the other hand, the vapor pressure of methanol is approximately 200-mm Hg at the test condition, and variations with the temperature differences involved are substantial. Thus, the net measured force on the methanol bubble is greater than the theory predicts even though thermal mixing occurs.

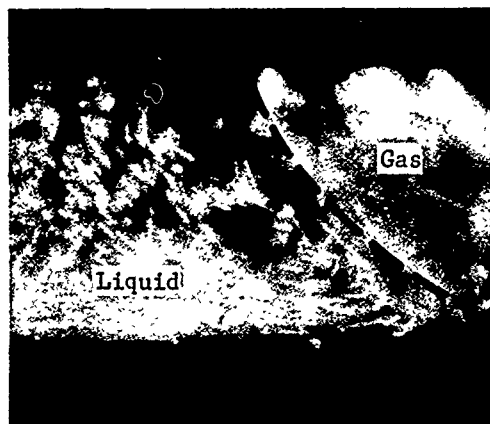
Good agreement between the predictions and the results of the thermophoretic experiments establishes the validity of the analysis for the case of low vapor pressure. Liquid/vapor pressure, if appreciable, results in an increase in bubble force.

### 3. Flow around Bubbles

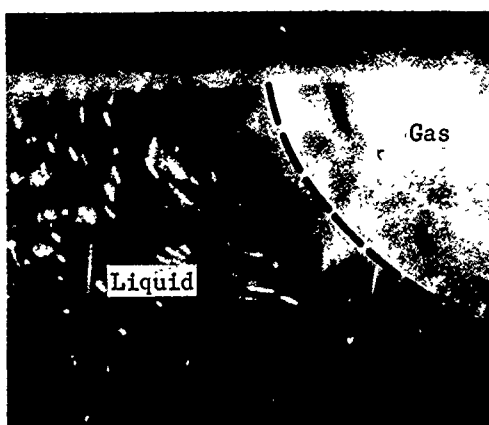
Using the apparatus previously described, experiments were conducted to determine the flow patterns around vapor and gas bubbles both on a solid heating surface and suspended more or less freely in the liquid. Figure 21 shows the liquid flow patterns around air bubbles that were placed on the under side of the heating surface. Since the photographs are time exposures, the Ecospheres appear as streaks indicating flow streamlines. Figure 22 is a sketch showing the direction of motion of liquid around the bubble. As shown, liquid flows along the bubble surface from the hot toward the cold region.



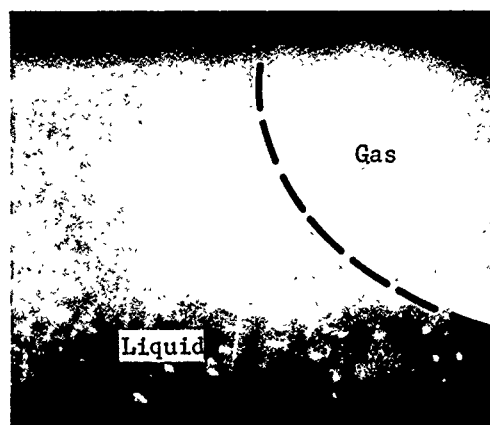
(a) Control Test (No Bubble),  
 $\Delta T/\Delta X = 35^\circ\text{C}/\text{cm}$   
 exposure time = 0.5 sec



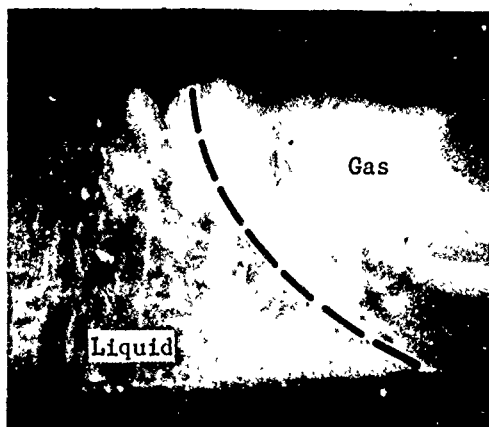
(b)  $\Delta T/\Delta X = 35^\circ\text{C}/\text{cm}$ ,  
 exposure time = 0.5 sec



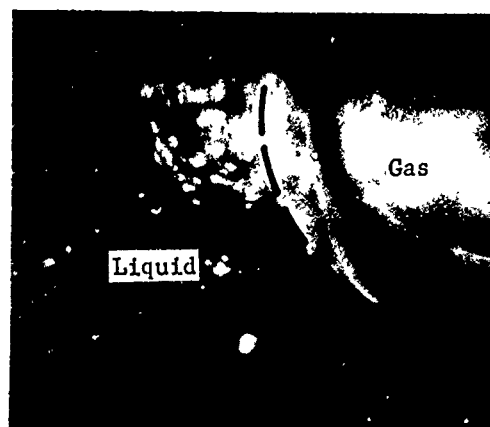
(c)  $\Delta T/\Delta X = 22^\circ\text{C}/\text{cm}$ ,  
 exposure time = 0.5 sec



(d)  $\Delta T/\Delta X = 20^\circ\text{C}/\text{cm}$   
 exposure time = 0.25 sec



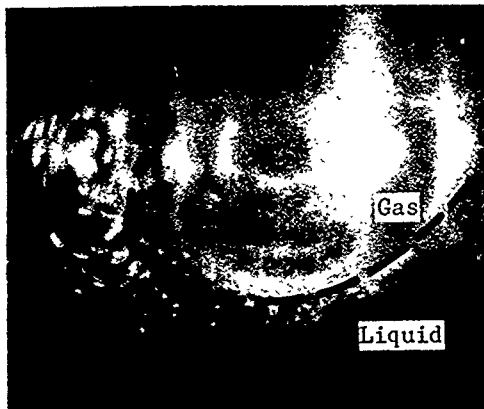
(e)  $\Delta T/\Delta X = 15^\circ\text{C}/\text{cm}$ ,  
 exposure time = 0.25 sec



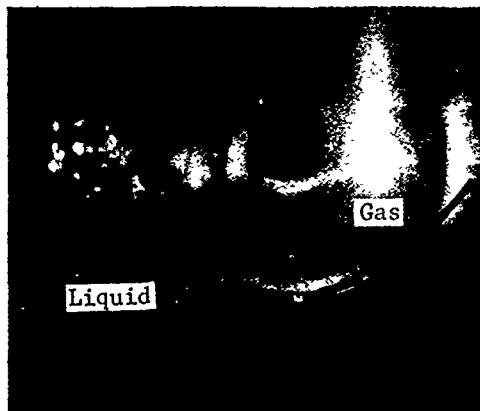
(f)  $\Delta T/\Delta X = 4^\circ\text{C}/\text{cm}$   
 exposure time = 0.25 sec

Fig. 21 Marangoni Flow Around Air Bubbles on a Heated Surface

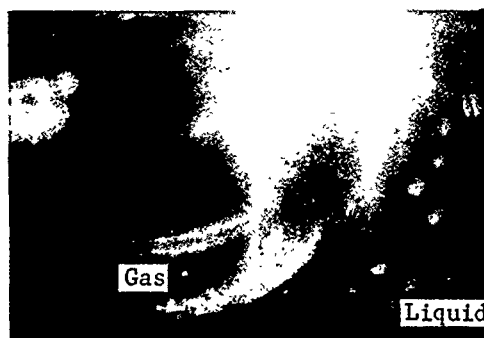




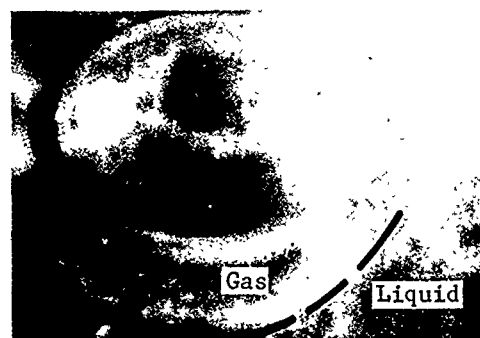
(g)  $T = 30 \text{ sec}$ ,  
 $\Delta T/\Delta X = 30^\circ\text{C/cm}$ ,  
 exposure time = 0.25 sec



(h)  $T = 5 \text{ minutes}$ ,  
 $\Delta T/\Delta X = 2^\circ\text{C/cm}$ ,  
 exposure time = 0.25 sec



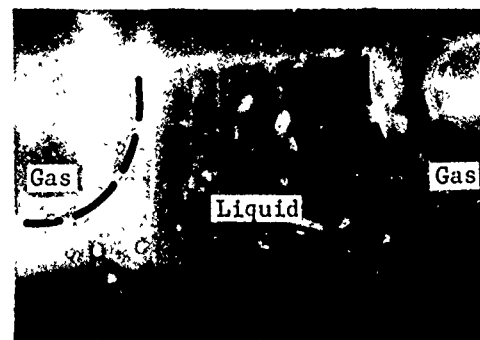
(i)  $T = 1 \text{ minute}$ ,  
 $\Delta T/\Delta X = 35^\circ\text{C/cm}$ ,  
 exposure time = 0.5 sec



(j)  $T = 2 \text{ minutes}$ ,  
 $\Delta T/\Delta X = 20^\circ\text{C/cm}$ ,  
 exposure time = 0.5 sec



(k) Two bubbles,  
 $\Delta T/\Delta X = 35^\circ\text{C/cm}$ ,  
 exposure time = 0.5 sec



(l) Two bubbles,  
 $\Delta T/\Delta X = 25^\circ\text{C/cm}$ ,  
 exposure time = 0.25 sec

Fig. 21 (concl)

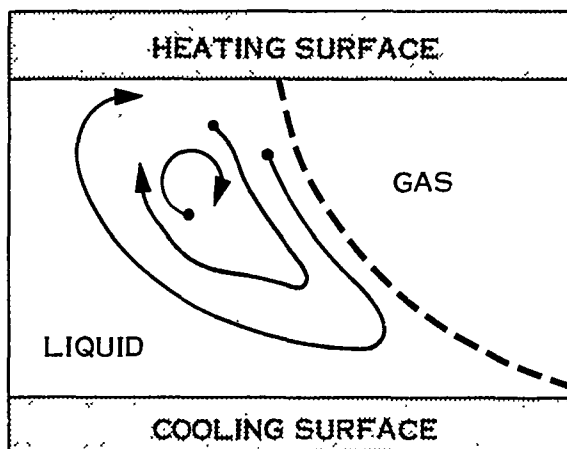


Fig. 22 Liquid Flow at a Bubble Surface

Figure 21(a) shows a control test with no bubble present. As can be seen, no liquid motion occurs even though a relatively large temperature gradient is present. Figures 21(b) through 21(f) show flow around five different bubbles. By measuring the lengths of the streaks in the time exposures, liquid velocities can be estimated. At the bubble surface, flow velocities on the order of one to two cm/sec are observed. Figures 21(g) and 21(h) show flow around the same bubble at different times. As can be seen, liquid is flowing around the entire bubble surface in Fig. 21(g), whereas in Fig. 21(h) there is only a small vortex near the heating surface. Figure 21(g) was taken shortly after the heat was applied, whereas Fig. 21(h) was taken somewhat later. Figures 21(i) and 21(j) indicate the same trend. The gradual decrease in size and intensity of liquid circulation patterns was a consistent trend and is attributed to reduced surface tension gradients around the bubble due to liquid thermal mixing. Liquid circulation patterns around two adjacent bubbles are shown in Fig. 21(k) and 21(l). When heat is applied, the liquid between the adjacent bubbles is circulated more rapidly than elsewhere and, consequently, more quickly reaches thermal equilibriums such that motion ceases in that region while continuing in others. Thus, since the temperature tends to be highest between the bubbles,

the thermophoretic forces cause the two bubbles to move toward the region of higher temperature and the bubbles tend to coalesce. The coalescence tendency of neighboring bubbles was consistently observed. With a single bubble on the horizontal heated surface, no bubble motion occurred. But with more than one bubble, the bubbles moved toward one another shortly after the heat was applied, if they were reasonably close together. To permit experimentation with individual adjacent bubbles, slight depressions were made in the heating surfaces such that the two bubbles would have to move downward to coalesce. The depression stabilized the positions of the adjacent bubbles and prevented coalescence, which always occurred on a perfectly flat surface. Experiments were also conducted with vapor bubbles produced by boiling at the heated surface. In these experiments, boiling was started at the heated surface by slowly increasing the heater temperature. The liquid flow patterns were more readily observed when boiling was vigorous but not so violent that the viewing area was completely filled with bubbles. When boiling was established, we consistently observed flow patterns which were similar to those with air bubbles. The liquid moved along the heated surface toward the bubble from all sides and then traveled downward around the bubble periphery and was exuded downward in a stream from the bottom extremity of the bubble. The exuded stream was only observed during vigorous boiling and was not present with mild boiling or with air bubbles. The circulation patterns around bubbles during mild boiling were identical with those observed around gas bubbles. As new bubbles grew at the preferred nucleation sites, they very quickly established the same characteristic liquid flow patterns. The liquid circulation velocities observed in boiling were considerably higher than those observed in the air bubble experiments, but no velocity measurements were made. The bubbles produced by boiling had a strong tendency to move toward each other and to coalesce. Bubbles left the heating plate by sliding along horizontally and were not observed to move downward from the heating surface. Experiments were also conducted using air bubbles suspended on the wire as explained in a previous section of this report. Liquid flow patterns around the suspended bubbles were very similar to those patterns described above; however, flow in the vicinity of the hot pole of the bubble was altered slightly due to removal of the solid surface. The results discussed above are shown in the film supplement to this report.

Typical results of the shadowgraph photos are shown in Fig. 23. The bubbles are not visible due to the photographic technique used but are on the heated surface. Liquid density patterns associated with Marangoni flow around the bubbles are clearly visible.

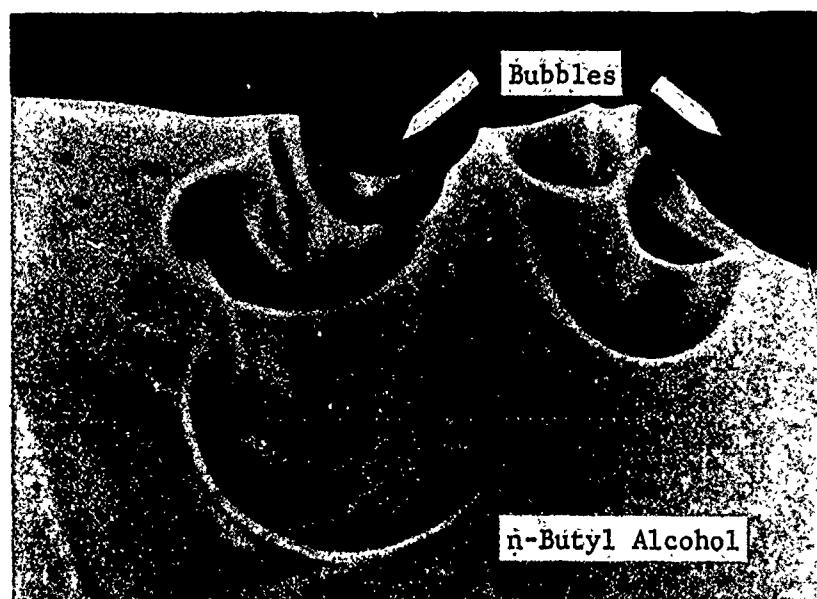
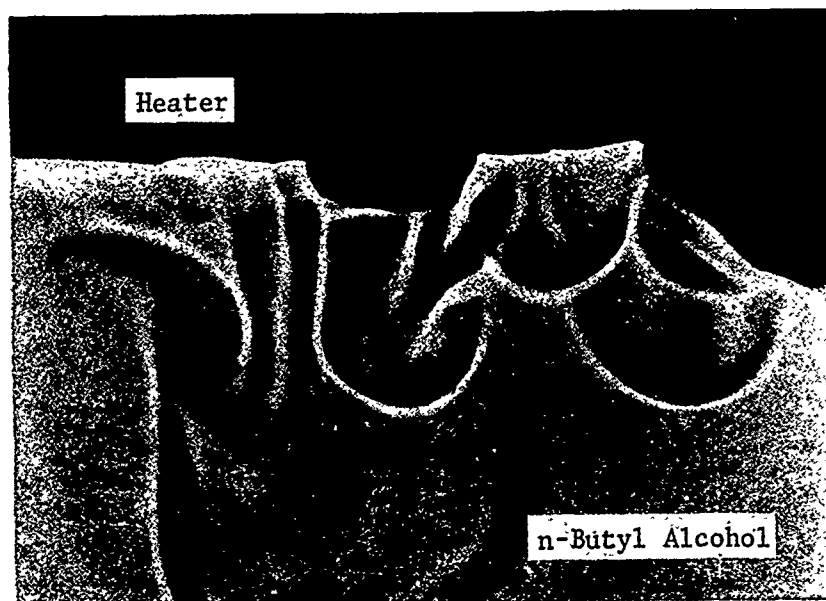


Fig. 23 Shadowgraphs of Density Patterns in the Vicinity of Air Bubbles in n-Butyl Alcohol

The results of the experiments indicate that turbulent flow patterns are established by temperature-induced surface tension gradients around bubbles. High liquid velocities were consistently observed near the boundaries of bubbles in nonisothermal liquid. Flow patterns around air and vapor bubbles were essentially identical for similar conditions. The velocity and temperature patterns observed lead to the hypothesis that Marangoni flow is important in boiling heat transfer, but definite conclusions await further experimental study.

#### 4. Boiling

Photographs of the normal and zero-gravity boiling show some interesting and unexpected results. Figure 24 shows the transition from normal gravity boiling to zero-gravity boiling. Although no temperature measurements were made during the free-fall tests, we estimate that the bulk liquid temperature is about  $0.8^{\circ}\text{R}$  below the saturation condition. This estimate is based on bench tests using the same experimental configuration, heating rates, and dewar pressure used in the free-fall tests.

Figure 24(a) shows bubble evolution in normal gravity prior to capsule release. Bubbles form slightly below the top of the test probe and are rather elongated. During the growth period, these bubbles merge with other bubbles and slide up the metal surface. At a point just above top of the test probe, bubbles reach a maximum size and depart from the surface. This process is somewhat different from that for bubbles growing on a horizontal surface, since the entire bubble is in upward motion during growth. At departure, the bubble shape changes from the elongated form to a more nearly spherical form. That buoyancy forces are primarily responsible for bubble detachment is suggested by the steep trajectory of the bubbles. During the growth process, the bubbles move upward; at departure their path makes an angle from 10 to 20 deg with the zenith, and this angle changes to 30 or 40 deg as they cross over the top of the test probe. At departure, the bubbles are about the same size as the test probe, or about 30 mils in diameter. Because the liquid is below its saturation temperature, the bubble radius continues to decrease as the bubble rises.

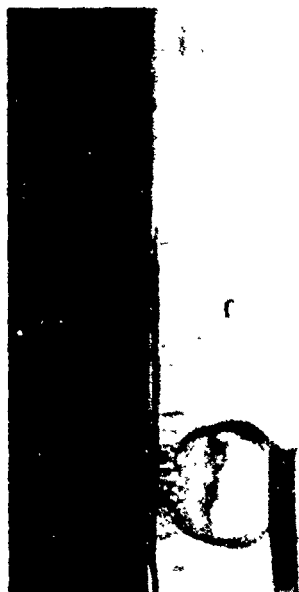
The transition from normal gravity to zero gravity is quite abrupt. At the instant of capsule release, the rising bubbles suddenly stop.



(a) Normal Gravity Boiling



(b) Zero-Gravity Boiling



(c) Zero-Gravity Boiling



(d) Zero-Gravity Boiling

Fig. 24 Boiling Experiment, Bubble Formation in Normal and Zero Gravity  
(Test Liquid, Liquid Hydrogen)

Two types of bubble growth are observed in zero gravity, and these are illustrated in Fig. 24(b), (c), and (d). Nearly all of the vapor formed is fed into a single large bubble. This large bubble is formed by both evaporation of liquid at the bubble base region and by the merging of small elongated bubbles into the larger one. Eventually the bubble grows to the size, and even beyond the size, of the test probe and becomes attached to the probe itself. By scaling from the photographs, we see that the diameter has increased by a factor of about 6 over that for normal gravity boiling. This corresponds to a volume increase of 216 times. By no means is this figure to be taken as the ultimate size, since the bubble was still growing at the time of impact when the experiment ended. The test duration was 0.8 sec.

Although accounting for only a tiny fraction of vapor generation, a second type of bubble generation was noted. A single bubble, about 5 probe diameters above the probe top, is seen to be forming in Fig. 24(b). Between the frames of Fig. 24(b) and 24(c), this bubble is suddenly ejected straight out from the surface. It comes to a stop about 3 probe diameters from the surface and, as shown in Fig. 24(c) and 24(d), begins to collapse in the cooler liquid.

The results of boiling in zero gravity were essentially the same whether boiling was started before capsule release or after capsule release.

The formation of the relatively large bubbles in zero gravity qualitatively verifies the predictions of growth based on capillary theory. However, quantitatively, there is poor agreement, because the observed shapes do not resemble those predicted from capillary theory.

Results presented above suggest that attempts to predict boiling heat transfer rates from free-fall test data would be futile. Boiling heat transfer rates are usually presented as graphs of flux vs temperature difference. But these data are presented as steady-state data. If heat transfer rates were measured for the test shown in Fig. 24, it would not be possible to claim that these rates were steady-state rates. To attain steady-state conditions, many bubbles would have to be generated and removed from the surface. From our tests, we know the period for bubble formation is at least 0.8 sec and perhaps much longer. Assuming we need at least 10 bubble periods to provide a reasonable time to achieve the steady-state condition, then the free-fall test time must be more than 8 sec. This corresponds to a test tower height of 1024 ft, and even this might not be nearly enough. Perhaps there exists no steady-state configuration -- perhaps bubbles remain attached to the surface indefinitely and continue to grow.

## II. LIQUID VENTING

### A. INTRODUCTION

During many space missions it will be necessary to discharge (vent) propellant to space. Because of the low temperature of liquid hydrogen, it is reasonable to expect continuous heat flow into the tanks of any hydrogen-fueled vehicle. Heating a confined fluid always results in pressure rise, and limiting pressure to a specific value requires removal of energy from the system. In the process of venting, energy is removed from the system, and, because of the latent heat difference, venting a pound of vapor is preferable to venting a pound of liquid.

Venting might be either continuous or intermittent. Intermittent venting, such as was once contemplated for the S-IVB, could present a serious problem in a low-gravity environment. If the propellant tank is coasting in orbit, it seems reasonable to expect that the kinetic energy imparted to the liquid during the process of vapor formation would propel significant amounts of liquid to the forward end of the tank, since there is no substantial difference in the potential energy associated with positions at opposite ends of the tank. Another important factor is the tendency of vapor bubbles formed as the pressure is reduced to remain attached to the nucleation site as a result of their lack of buoyancy, thus forcing the static position of the upper liquid surface to move toward the top (or front) of the tank. Both of these phenomena would limit the length of time that the vent could remain open without passing liquid, and hence would have a strong influence on the feasibility of intermittently venting the hydrogen tank during orbital coast.

The purpose of this phase of our program was to experimentally study the problem of intermittent venting and to develop an analysis that would allow design of venting systems.



## B. EXPERIMENTAL PROGRAM

### 1. Freon Venting

A series of free-fall venting experiments were performed, following a series of normal gravity venting tests. Figure 25 is a line drawing of the experimental apparatus installed in the drop capsule and Fig. 26, 27, and 28 are photographs of the same apparatus. Figure 29 shows the same experimental apparatus flanked by the equipment used for readout and control of the test specimen pressure. The test specimens were 15.2 cm and 29.2 cm (inside diameter) plexiglass cylinders. Test liquid was Freon TF (trichlorotrifluoroethane). This liquid was chosen both for its high vapor pressure at room temperature, resulting in ease of performing the experiments, and its low specific surface tension, resulting in more pronounced fluid behavior occurring within the relatively small test specimens.

The purpose of this series of experiments was to obtain a qualitative appreciation of the type of fluid behavior that might occur during rapid venting of an S-IVB, rather than quantitative results. The investigators responsible for carrying out the various portions of this program feel that quantitative data on such phenomena as boiling and evaporation in low-acceleration fields can be obtained only from experiments using the actual liquid of interest -- in this case hydrogen -- because of a lack of the detailed understanding of these phenomena required for valid scaling from one liquid to another.

Before the drop capsules were assembled and moved to the top of the drop facility, the throttling valve (Fig. 25 and 26) was set to give the desired vent rate, and the vacuum reservoir was evacuated. The solenoid-operated bypass valve was opened until the pressure in the test specimen had been reduced to saturation pressure (about 6 psia). After the vacuum reservoir pressure had been reduced to about 1 mm Hg, the vacuum pump and pressure readout dial were detached and the capsules assembled, sealed, and raised to the top of the drop tower. There the pressure readout dial was again attached (through electrical connectors between the capsules), and the bypass valve opened to finally adjust the test specimen pressure to a value near the saturation pressure. This adjustment was necessitated by air leakage into the test specimen during capsule assembly and evacuation of the space between the capsules, and while the assemblage was hoisted to the top of the drop tower.

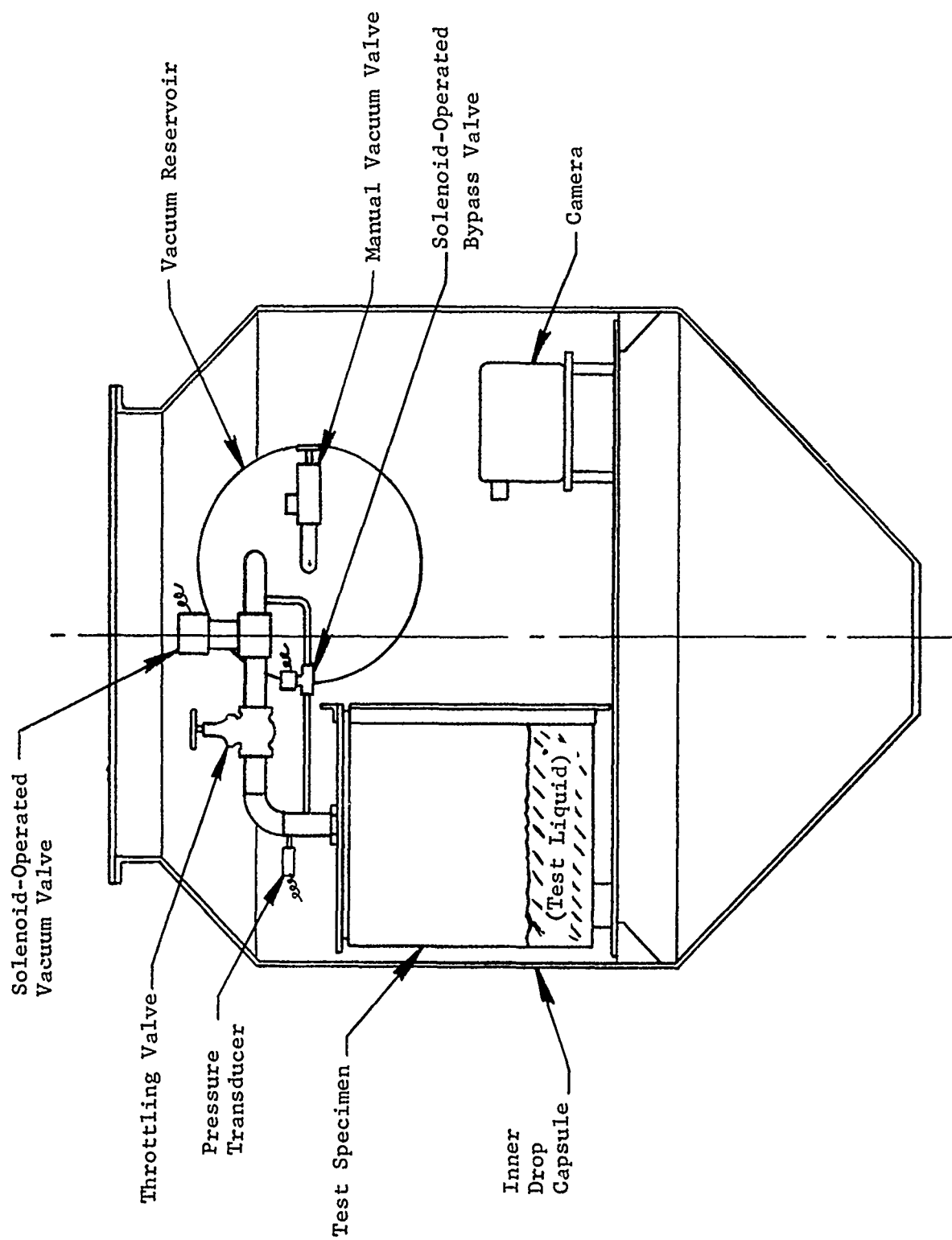
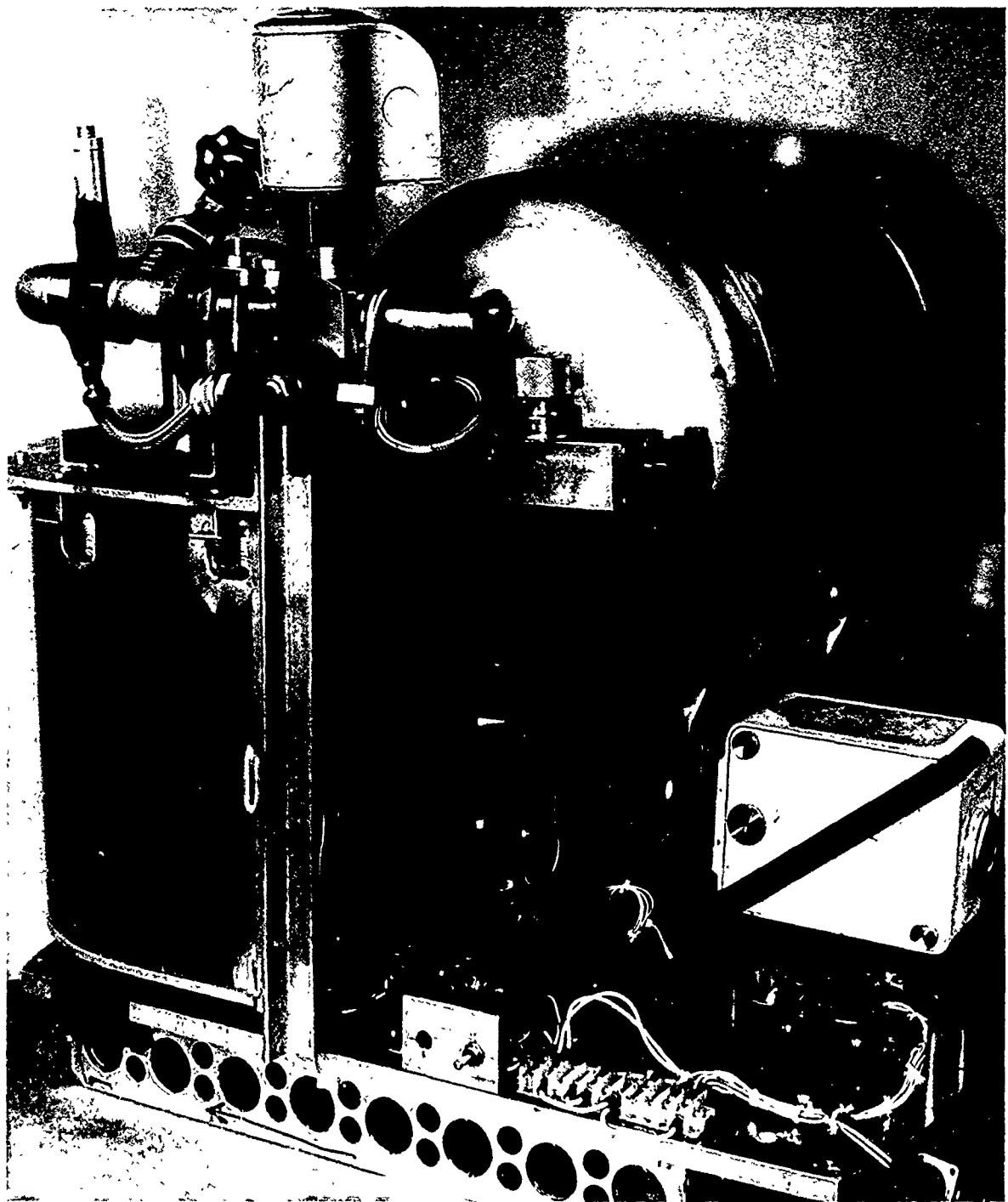


Fig. 25 Line Drawing of the Experimental Apparatus



Front View

Fig. 26 Experimental Apparatus

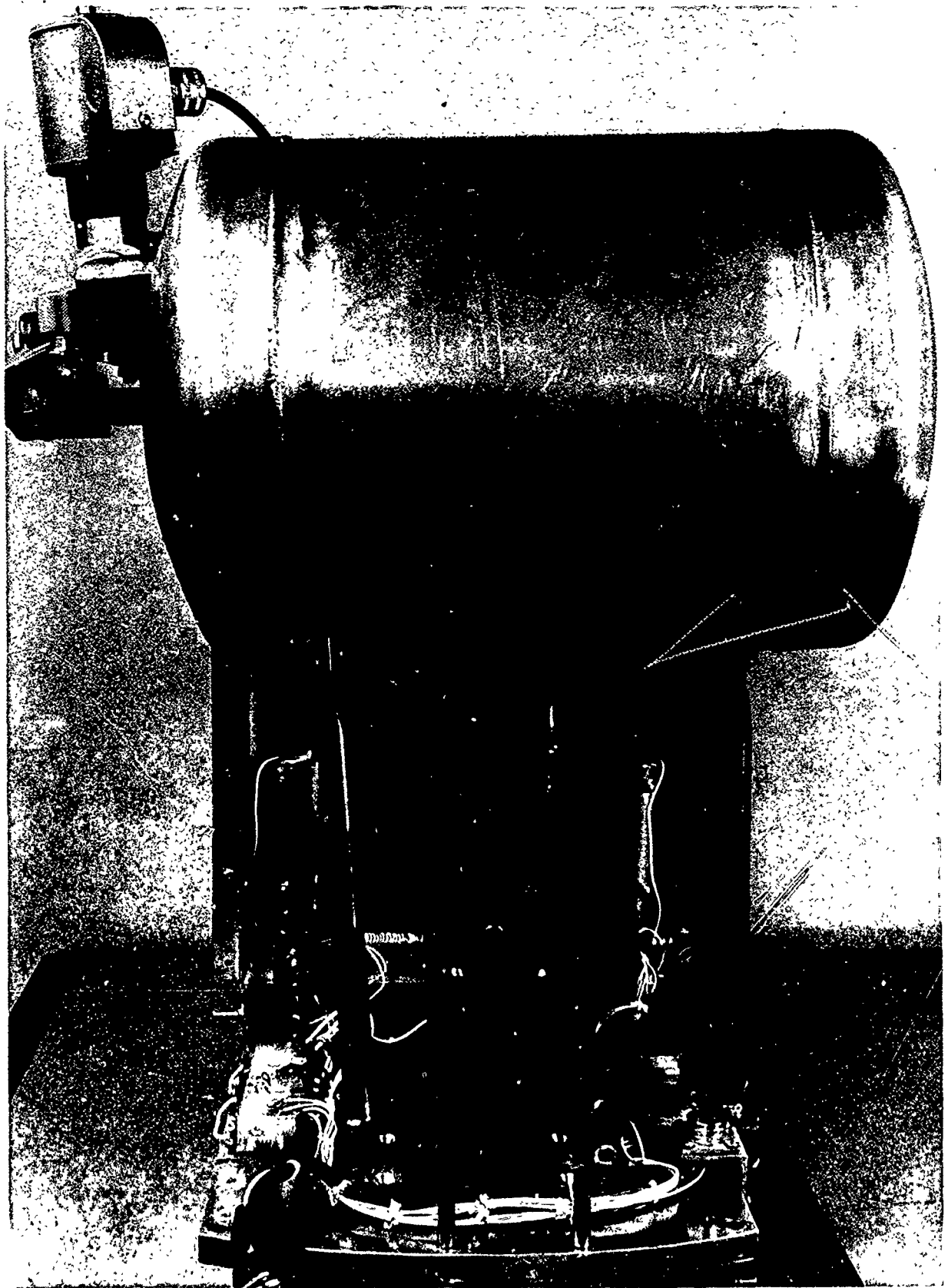


Fig. 27 Reservoir-Side View

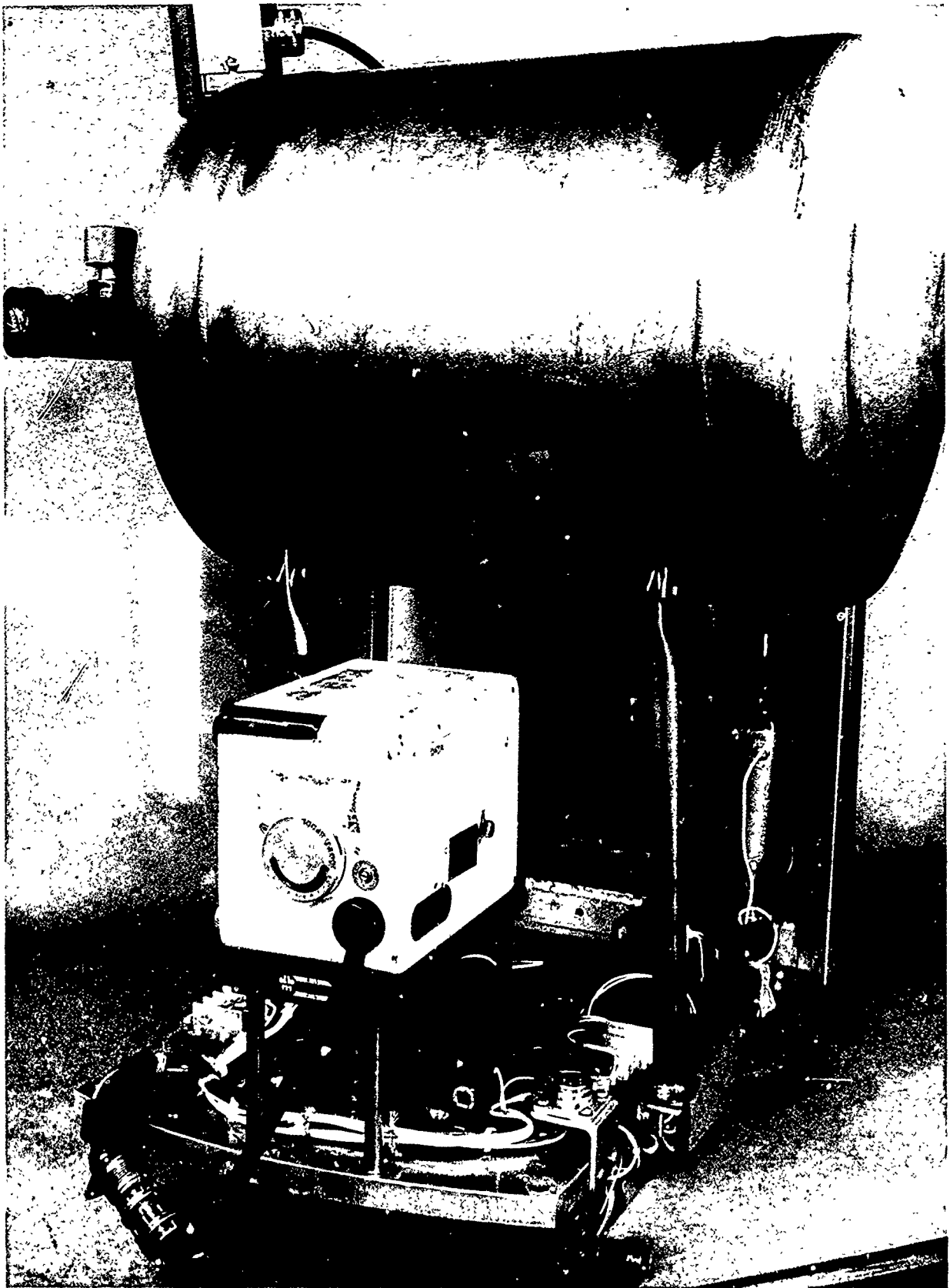


Fig. 28 Camera-Side View

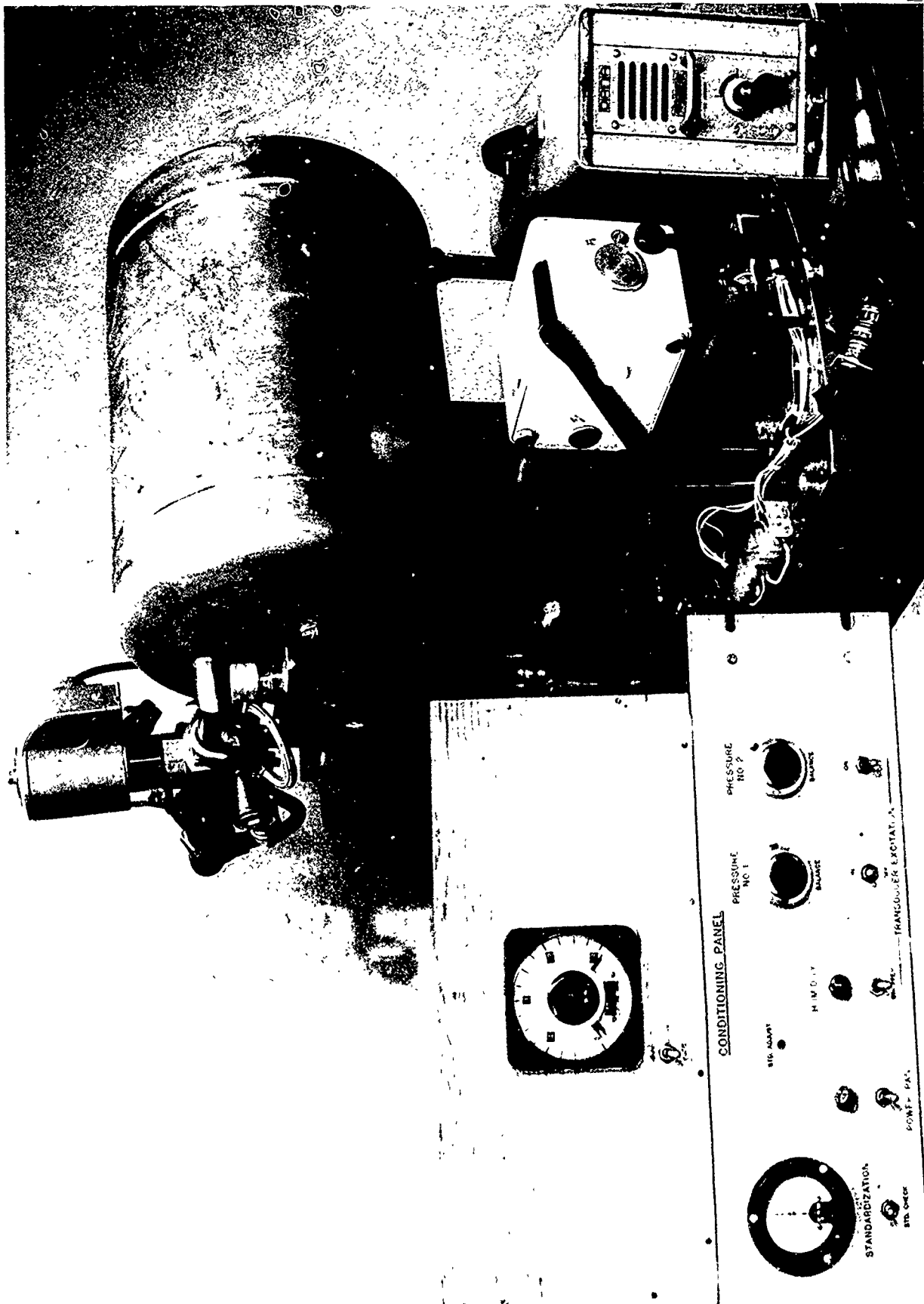


Fig. 29 Experimental Apparatus with Pressure Readout and Control Equipment

Immediately following release of the capsules, the downward motion of the outer capsule moved a microswitch, closing the circuit through the large solenoid-operated vacuum valve. A small wire dropped with the capsules carried the current required to hold the valve open for the duration of the drop. Data were recorded by a motion picture camera, operating at 200 frames per second, on Ektachrome MS film. A small amount of dye was added to the liquid to provide better photographic resolution.

Representative results\* are shown in Fig. 30, 31 and 32. Figure 30 shows venting of the 29.2-cm cylinder at one of the lowest venting rates used. Figure 31 shows venting of the 15.2-cm cylinder at the same rate. Although vapor production occurs at the same rate in either case, the amount of vapor produced is relatively more significant in the smaller vessel.

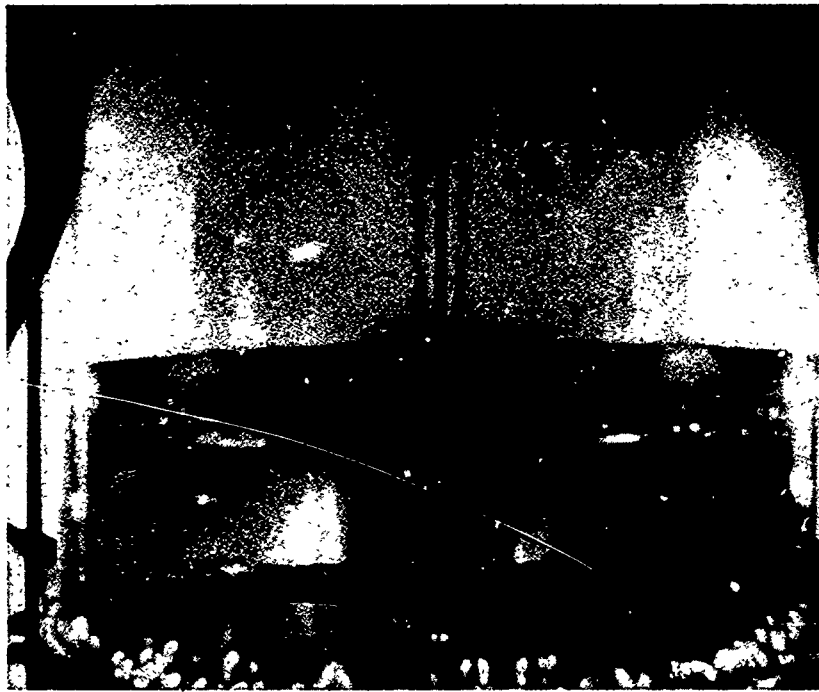
Figure 32 shows the smaller vessel being vented at a considerably higher rate, with the result that liquid is sent out of the vent.

In all of the experiments, vapor that formed below the liquid surface remained below the surface, pushing the liquid surface toward the vent. Bubbles that formed on the bottom of the tank appeared to remain attached to their initial nucleation sites, while those that formed on the walls moved upward with the surrounding liquid, which was pushed upward by bubbles growing below, but did not move relative to the liquid. Thus the bubbles did not rise to the surface, carrying vapor and entrained liquid into the ullage space, as they do in normal 1-g boiling. In addition, the kinetic energy imparted to the liquid during bubble formation was not observed to be a significant problem.

Thus the rate of venting was not found to have a measurable effect on the ability to vent a tank of saturated liquid without removing liquid through the vent. However, there is a definite limitation on the quantity of gas that can be vented. Since none of the bubbles formed on the wetted walls join the ullage, the amount of gas that can be removed is very nearly limited to the amount initially contained in the ullage. It is interesting that both these conclusions are opposite from the conclusions that would be drawn in the case of venting in normal gravity, where there is no limit on the quantity of gas that can be removed (short of actually evacuating the tank), but the rate is limited because of liquid entrainment by rising bubbles.

---

\*The results reported in the Phase I Report, Ref 20, were later found to be misleading because of a deficiency in the zero-gravity experimental technique.



(a)  $t = 1.0$  sec



(b)  $t = 2.1$  sec

Fig. 30 Zero-Gravity Venting of Freon TF, Cylinder  
Diameter = 29.2 cm, Vent Valve  $\frac{1}{2}$  Turn Open





(a)  $t = 1.0 \text{ sec}$



(b)  $t = 1.5 \text{ sec}$

Fig. 31 Zero-Gravity Venting of Freon TF, Cylinder Diameter = 15.2 cm, Vent Valve  $\frac{1}{2}$  Turn Open

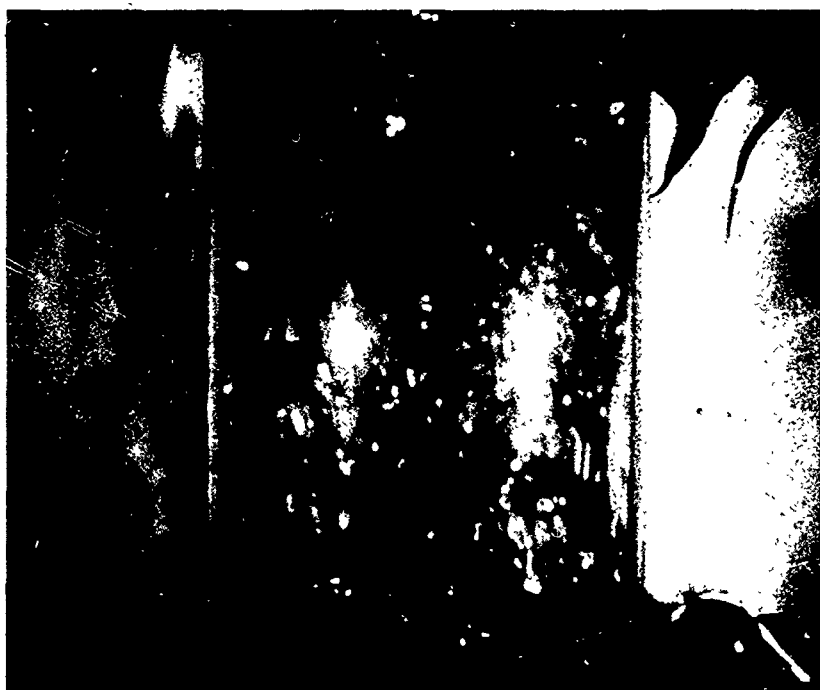


(a)  $t = 0.7$  sec



(b)  $t = 1.0$  sec

Fig. 32 Zero-Gravity Venting of Freon TF, Cylinder Diameter = 15.2 cm, Vent Valve 1 Turn Open



(c)  $t = 1.3 \text{ sec}$

Fig. 32 (concl)

## 2. Hydrogen Venting

The sudden venting of liquid hydrogen in zero gravity was studied experimentally in the Martin-Denver 16-ft drop tower facility, Fig. 33. Saturated liquid hydrogen, contained in a glass dewar, was vented after falling about 4 in. in the drop facility. Disturbances of the vapor/liquid interface were recorded by a movie camera, and the vented vapor was metered by collecting it in a tank of known volume. Both 4- and 8-in.-diameter dewars were used in the test program, and similar experiments were performed in normal gravity for the purpose of comparison.

Photographs of the apparatus are presented in Fig. 34 and 35, and a schematic of the apparatus is presented in Fig. 36. Suspended from the lid is a Teflon rod that supports three thermistors and an electrical heater, Fig. 34. The scale can be visualized from the fact that the threaded rods holding the lid are 1/4-20. The baffle, supported from the lid, is used to keep liquid from splashing into the vent system on impact. On the right side of the dewar, the 250-watt sun gun may be seen. To diffuse the illumination from the sun gun, an opal screen is fastened to the outer surface of the dewar. Figure 35 shows the dewar, camera, and associated plumbing. The Milliken camera, Type DBM IV, was run at 128 frames per second in the drop tests. Color film proved to be much superior to black and white in showing venting results, and we used Kodak Ektachrome, Type ER.

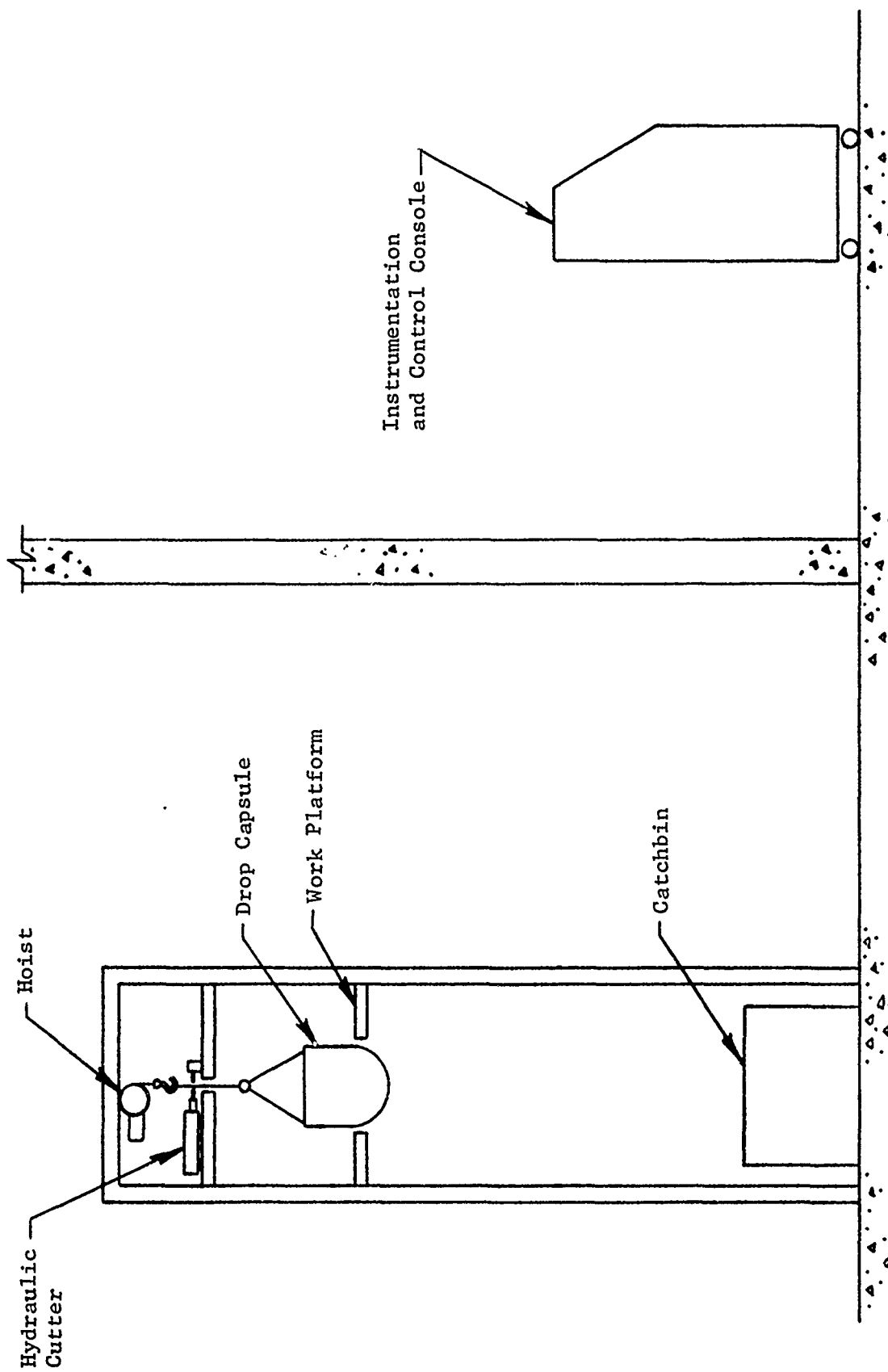


Fig. 33 16-ft Droptower Facility

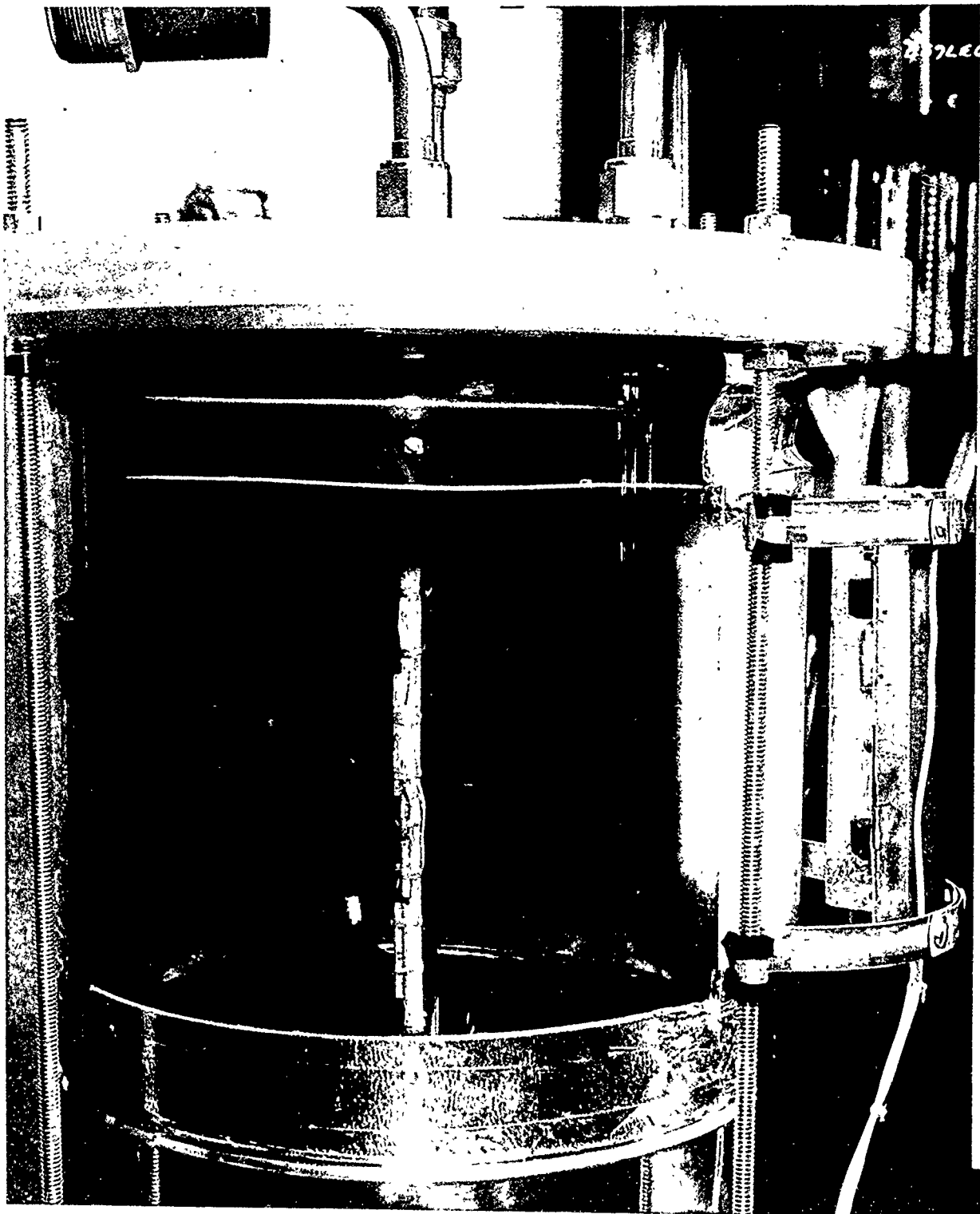


Fig. 34 Venting Experiment, 8-in. Hydrogen Dewar

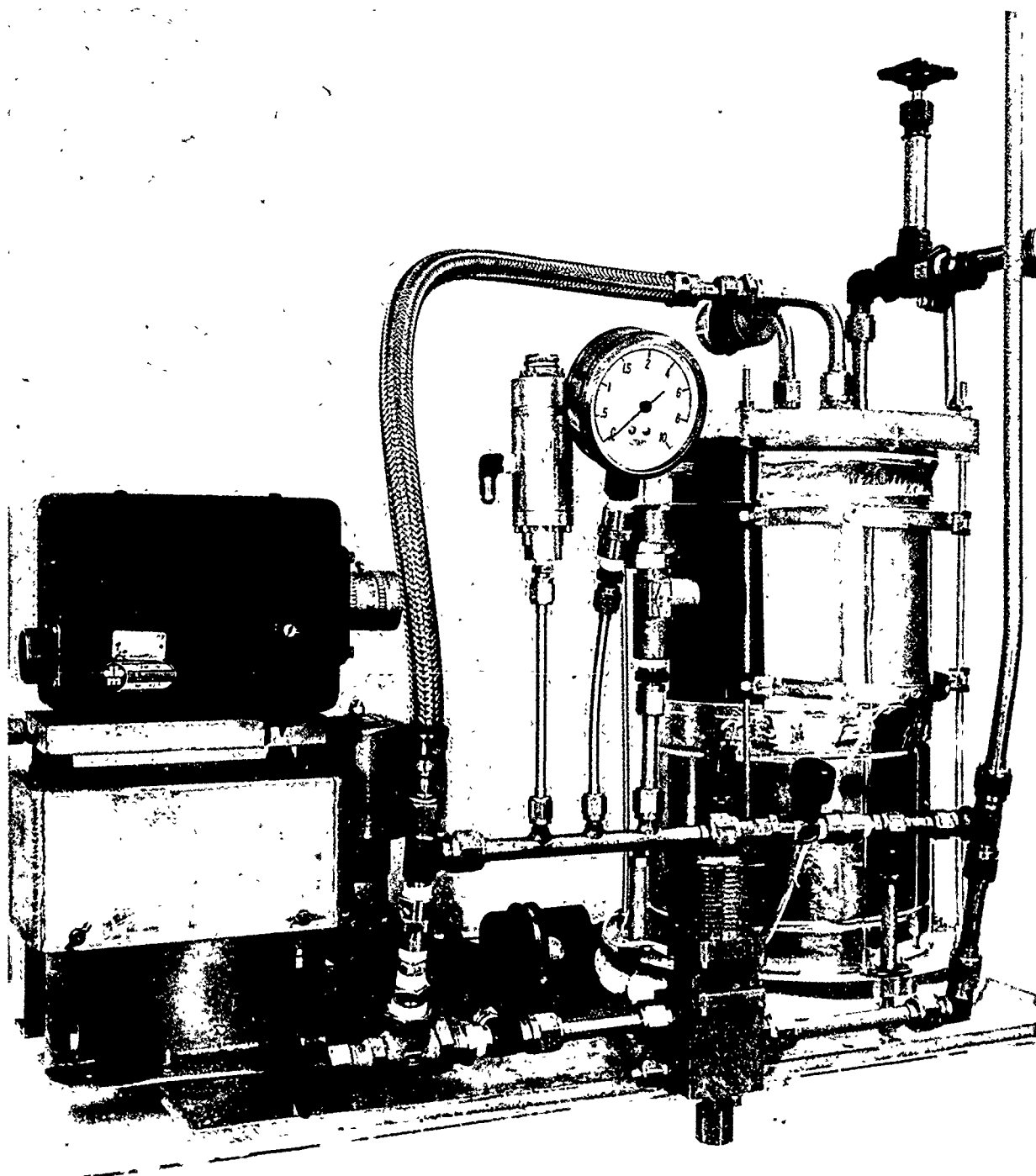


Fig. 35 Hydrogen Venting Apparatus

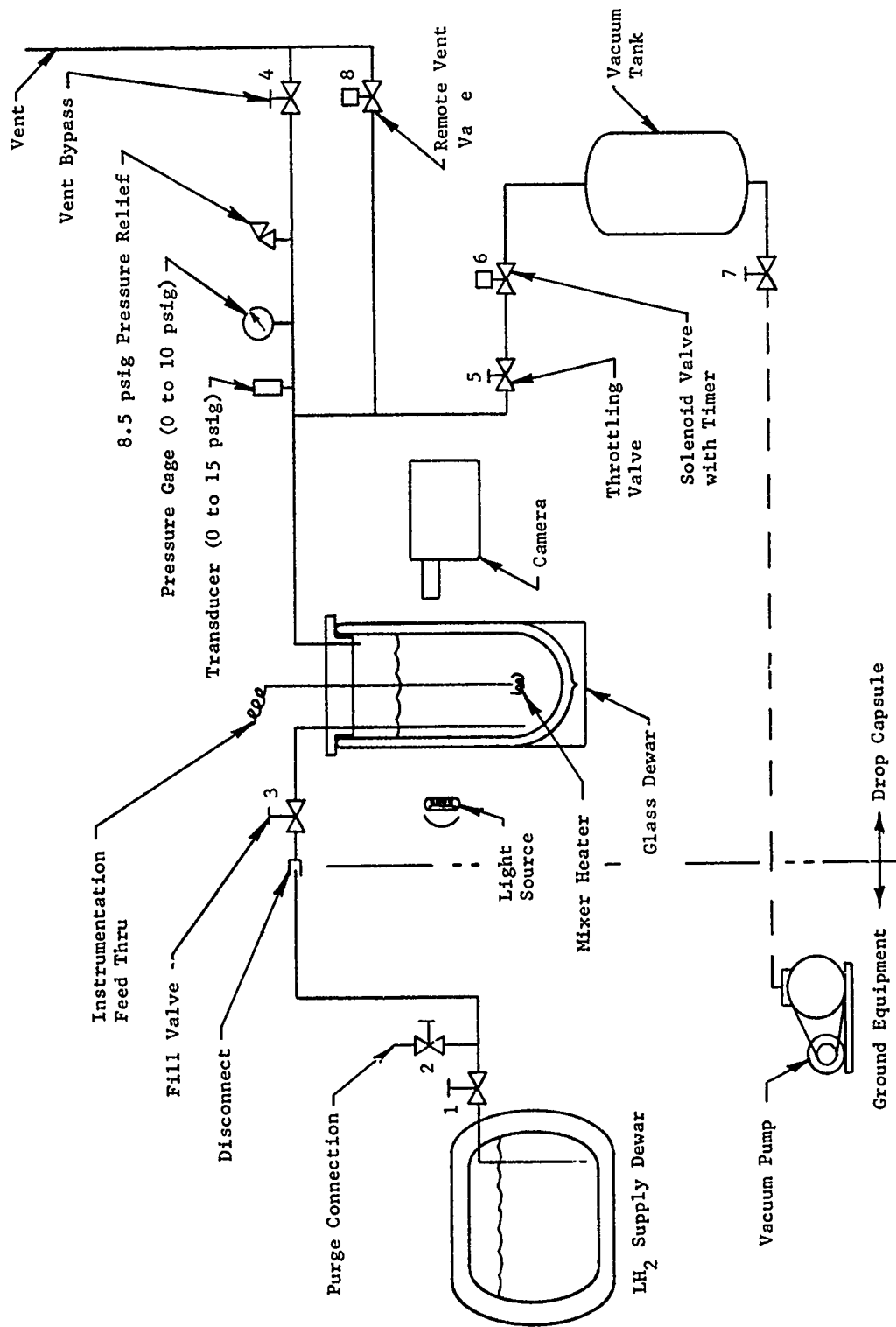


Fig. 36 Hydrogen Venting Schematic



Figure 36 is helpful in understanding the experimental procedure. First the metering tank is evacuated with a small Cenco pump to about 0.1 psia. The transfer line is connected between the test dewar and the 1000-liter dewar. Valve settings are as follows: 1 closed, 2 open, 3 closed, 4 open, 5 preset to provide desired vent rate, 6 closed, 7 closed, 8 open. Valves 1 and 2 are opened to purge the transfer line. Next valve 2 is closed and 3 is opened to initiate filling the test dewar. When liquid hydrogen is 1 in. below the baffle, 3 is closed, 1 is closed, and 2 is opened. The dewar is now filled, and the transfer line is removed, 4 is closed, and the capsule is hoisted to the tower top. From the control console, 8 is closed, and the pressure begins to rise in the sealed dewar. Power is next applied to the internal heater to increase the rate of pressure rise and to mix the liquid phase by bubble evolution. As the pressure reaches 8 psig, power is applied to the sun gun and movie camera, the internal heater is disconnected, and the hydraulic cutting block is actuated, releasing the capsule. At 4 in. in the drop trajectory, a solenoid timer opens 6 to vent the test dewar into the metering tank. The timer closes 6 at 0.75 sec after it opens (just before impact). On impact 8 is opened and power is removed from the camera and sun gun. Control of the vent rates is realized by the setting of valve 5 and changing the size of the metering tank. In computing the amount of vent vapor, tank temperature, volume, and pressure are measured and the ideal gas law is applied.

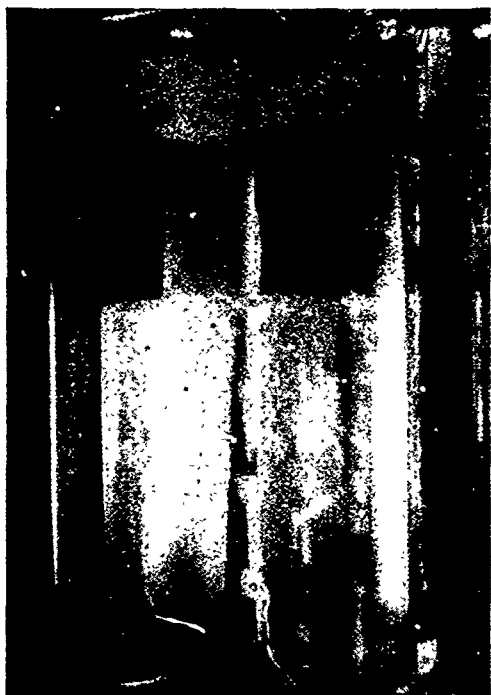
### C. RESULTS AND CONCLUSIONS

The results of 19 venting experiments for hydrogen are summarized in Table 1. Run 30, not listed, was performed by dropping the 4-in. dewar but not allowing the vent valve to open. Test results (Fig. 37) show interface disturbance at four times during the drop. In Fig. 37(a) the liquid interface is flat, and some boiling may be seen along the upper wall and along the instrumentation probe. For this frame the capsule has not yet been released. In (b), (c), and (d) of Fig. 37, the liquid boils as it climbs the container wall. The fact that the dewar wall above the liquid is above the local boiling temperature accounts for the boiling.

Table 1 Liquid Hydrogen Venting Data

Run No.	Nominal Dewar Size (in.)	Volume (cc)		Vented Mass (gm)	Vented Volume* (cc)	Ullage Pressure (psia)		Liquid Temperature (°R)		Vent Time (sec)	g Level
		Ullage	Liquid			Initial	Final†	Initial	Final		
17	4	1280	1270	1.26	1730	20.1	16.2	38.8	37.1	0.76	1
19	4	1280	1270	1.24	1660	20.1	16.7	38.8	37.3	0.76	1
20	4	1280	1270	0.97	1300	20.1	16.7	38.7	37.3	0.82	1
21	4	1280	1270	0.68	900	20.1	17.0	38.8	37.4	0.80	1
24	4	1050	1500	1.27	1750	19.9	16.2	28.7	37.1	0.74	0
26	4	1100	1450	1.21	1710	20.1	15.7	38.8	36.9	0.71	0
27	4	1100	1450	0.76	1210	19.9	13.7	38.5	36.1	0.74	0
28	4	1100	1450	0.53	840	19.8	13.7	38.8	36.1	0.74	0
31	8	2960	5340	1.19	1570	19.8	17.0	38.6	37.4	0.68	1
32	8	3360	4940	1.08	1670	19.8	14.2	38.5	36.3	0.68	1
33	8	2960	5340	0.77	1090	19.6	15.7	38.5	36.9	0.70	1
34	8	3360	4940	0.61	980	19.6	13.5	38.5	36.0	0.69	1
35	8	3550	4750	0.44	680	19.6	14.2	38.5	36.3	0.70	1
36	8	3160	5140	0.83	1680	19.8	10.6	38.5	34.6	0.70	0
38	8	3160	5140	0.74	1380	21.1	11.6	38.8	35.1	0.69	0
39	8	2960	5340	0.57	1080	19.8	11.4	38.2	35.0	0.72	0
46	8	2370	5960	1.37	2210	19.6	13.5	37.5	36.0	0.75	1
47	8	2370	5960	1.06	2580	19.6	8.5	37.1	33.4	0.77	0

\*Based on final temperature and pressure.  
†Assumed as saturation pressure at final temperature.



(a)



(b)



(c)



(d)

Fig. 37 Venting Test 30

To show that venting can lead to liquid loss in the system, we cite Fig. 38. Figure 38(a) shows the initial interface to be flat. On venting [Fig. 38(b)] a mist forms in the ullage space just over the rising liquid. At later stages in experiment [Fig. 38(c) and 38(d)], liquid has expanded up to the baffle. Note the large size of the vapor bubbles that were formed. Figure 39 shows results qualitatively similar to Fig. 38, but for the larger dewar. As venting begins, bubbles form around the Teflon rod and at the upper liquid surface. The single bubble in the right side of the dewar [Fig. 38(b)] was generated in normal gravity and was arrested at that point by capsule release. Figures 38(c) and 38(d) show that additional bubbles have formed, and some have even formed in the liquid interior. The large bubble in the upper right corner of Fig. 39 formed over a hole in the baffle.

Normal gravity venting tests showed a considerable difference. When a bubble forms in the saturated liquid, an appreciable buoyancy force expels the vapor bubble from the liquid phase. Sudden venting in normal gravity leads to violent bubble evolution and much disturbance of the vapor/liquid interface. On the other hand, in zero gravity there is no buoyancy force to expel the vapor bubbles. Thus bubbles form and cause the original vapor/liquid interface to rise in response to the volume increase resulting from vapor formation. No appreciable amount of kinetic energy was imparted to the liquid as a result of venting. Although some motion is imparted to the liquid as a result of change in  $g$  level from unity to zero, there seems to be no additional contribution to motion from venting. At lower vent rates, for example, in runs 21 and 28, the liquid motion was similar to that of the no-vent run 30.

On the basis of venting tests for both hydrogen and Freon it is possible to propose a relatively simple venting design theory. Because venting is a relatively complex phenomenon and the tests were run in small vessels and were of short duration, our theory contains some deficiencies. During venting, vapor will form at both the original liquid/vapor interface and in the liquid at various nucleation sites. While surface-formed vapor might be free to flow through the ullage space and escape to the vent system, we assume all vapor generated is formed in the liquid interior. This, of course, is a conservative estimate. Vapor bubble growth causes the original liquid/vapor interface to move through the original ullage space. To avoid liquid loss in venting we permit expansion only until the original ullage volume is replaced by newly formed vapor.



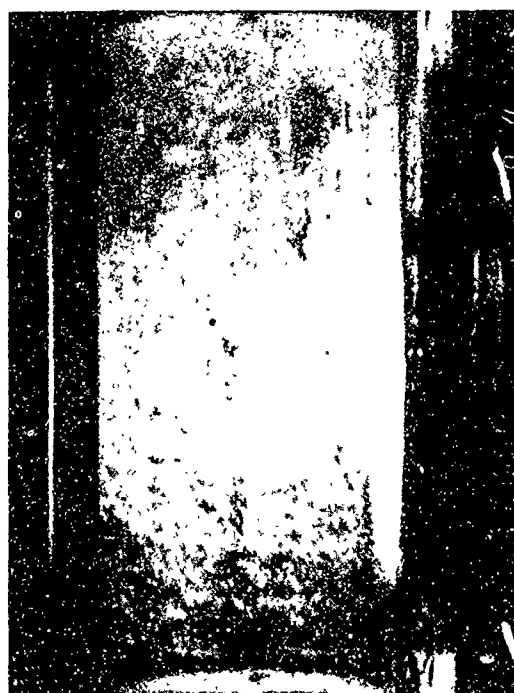
(a)



(b)



(c)



(d)

Fig. 38 Venting Test 24 (Using Liquid hydrogen)



(a)



(b)



(c)



(d)

Fig. 39 Venting Test 47

Thus the amount of vent mass may be determined from the above model. For the maximum venting rate, the vent system itself must be considered. Because of the pressure ratio between space and ullage pressure, it is reasonable to expect sonic flow in the vent line. Thus the vent must be open long enough to allow the original ullage vapor, flowing at sonic speed, to escape.

Because of the simplicity of the theory, the calculation of pressure decrease from venting is a straightforward thermodynamic exercise. In the process of venting we suppose that bottoming rockets are used to move the propellant from the force end of the propellant tank to the aft end thus clearing the vent line. This bottoming or settling operation induces thermodynamic equilibrium between vapor and liquid, and the initial tank pressure is  $P_0$ . Before venting, the mass in the system is a vapor mass,

$$M_v = V_v \rho_v,$$

and a liquid mass,

$$M_\ell = (V - V_v) \rho_\ell,$$

where  $V$  is the total tank volume,  $V_v$  is the ullage volume,  $\rho_v$  is the vapor density and  $\rho_\ell$  is the liquid density. By the venting operation, the mass  $M_v$  is removed from the system and the liquid mass expands at constant internal energy (no heat transfer and no work is done). To solve for the resulting pressure and temperature, several simultaneous equations must be solved:

$T = f(P)$ , the vapor pressure curve;

$\rho_v = g(P, T)$ , the saturated vapor density curve;

$\rho_\ell = h(P, T)$ , the saturated liquid density curve;

$M_\ell = V_v' \rho_v' + (V - V_v') \rho_\ell'$ , the material balance;

$M_\ell e_\ell = M_\ell' e_\ell' + M_v' e_v'$ , the energy balance;

where

$e$  = internal energy,

' = thermodynamic state following venting.

Solutions of these equations were obtained for parahydrogen, and the results are presented graphically (Fig. 40). Parametric curves are shown for initial tank pressures of 1, 2, and 3 atm. Initial ullage fraction is the independent variable, and, for each initial pressure, the ratio of pressure after venting to initial pressure decreases monotonically with ullage fraction.

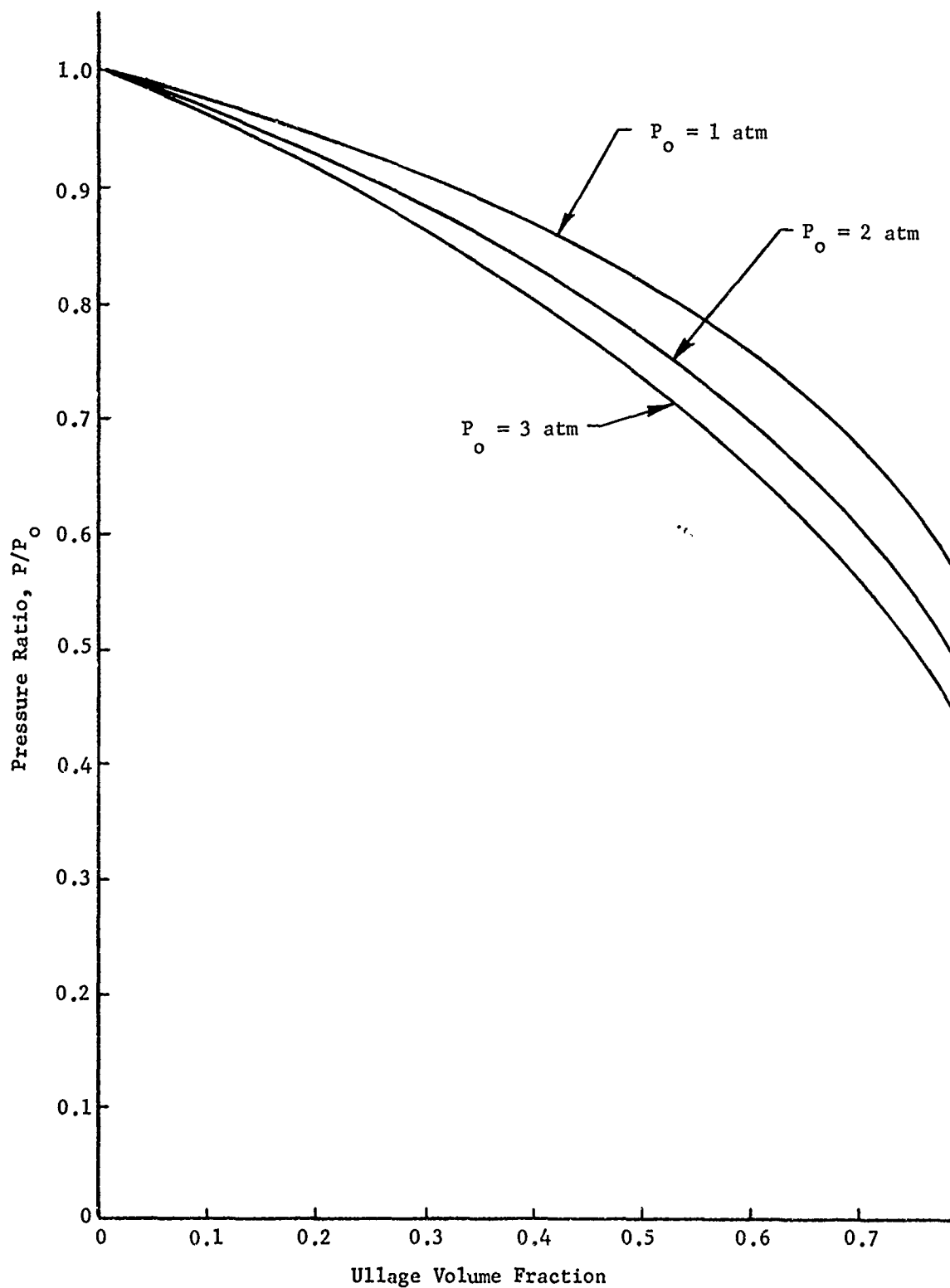


Fig. 40 Pressure Change from Venting



Zero-gravity experiments, with both hydrogen and Freon, support the conclusion that vapor bubbles tend to remain in the vicinity of their nucleation site. Venting at low volumes (vent vapor volume much less than ullage volume) produces no more interface disturbance than merely dropping a sealed vessel. By assuming that all vapor formed from venting causes the liquid to expand and thereby replace the original ullage volume, a simple thermodynamic calculation of allowable pressure decrease may be made.

## REFERENCES

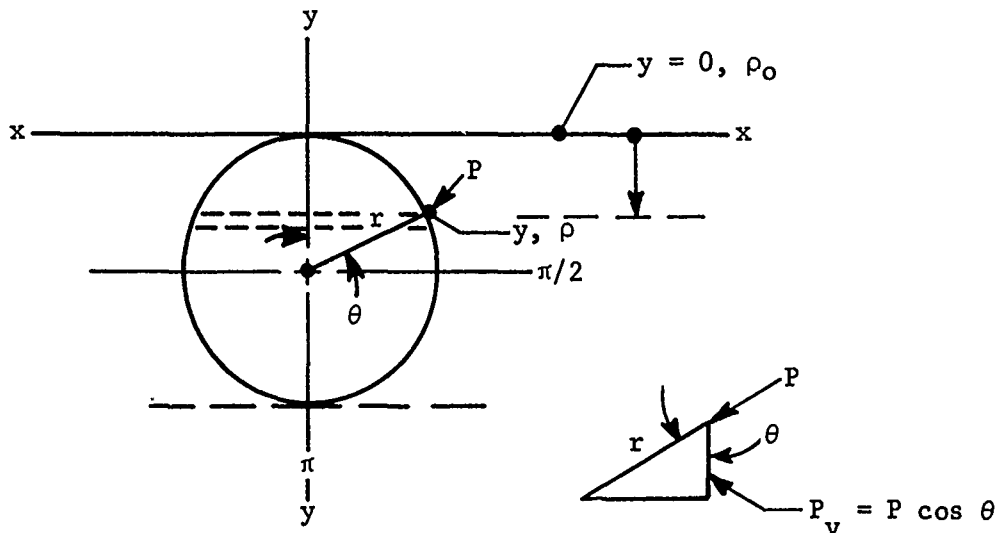
1. J. A. Clark and H. Merte, Jr.: Advances in Astronautical Science, 14, p 177 to 196, 1963.
2. E. G. Keshock and R. Siegel: NASA TN D-2299, 1964.
3. J. E. Shirley: "Nucleate Boiling Heat Transfer Data for Liquid Hydrogen at Standard and Zero Gravity." Advances in Cryogenics, Plenum Press, Vol 8, 1962.
4. T. R. Rehm: Preprint 24b, Am. Inst. Chem. Engr. Meeting, February 1965.
5. C.S.M. Marangoni: Il Nuovo Cimento, Ser 2.516, p 239, 1872.
6. L. E. Scriven and C. V. Sternling: "On Cellular Convection Driven by Surface Tension Gradients." J. Fluid Mechanics, 19, p 321, 1964.
7. N. O. Young, J. S. Goldstein, M. J. Block: "The Motion of Bubbles in a Vertical Temperature Gradient." J. Fluid Mechanics, 6, 1959.
8. W. Fritz: Physik. Z., 36, p 379 to 384, 1953.
9. F. Bashforth and J. C. Adams: An Attempt to Test the Theories of Capillary Action. University Press, Cambridge, England, 1883.
10. M. Jakob: Heat Transfer, Vol I. John Wiley & Sons, New York, New York, 1949.
11. R. Siegel and E. G. Keshock: Am. Inst. Chem. Eng. J., 10, p 509 to 518, 1964.
12. K. Kawasaki: J. Colloid Sci., 15, p 402 to 407, 1960.
13. C. G. L. Furmidge: J. Colloid Sci., 17, p 309 to 324, 1962.
14. J. J. Bikerman: J. Colloid Sci., 5, p 349 to 359, 1950.
15. J. A. Clark and H. Merte, Jr.: Advances in Astronautical Science, 14, p 177 to 196, 1963.

16. A. W. Adamson: Physical Chemistry of Surfaces. Interscience Publishers, New York, New York, 1960.
17. H. Bateman: Partial Differential Equations of Mathematical Physics. Cambridge University Press, Cambridge, England, 1959.
18. D. W. Peaceman and H. H. Rachford: J. of the Soc. for Ind. and Appl. Math., 3, No. 1, p 28 to 41, 1955.
19. R. W. Graham, R. C. Hendricks, and R. C. Ehlers: NASA TN D-1883 and Film Supplement C-224. February 1965.
20. T. E. Bowman, B. K. Larkin, and I. L. McGrew: Phase I Report, Criteria for Cryogenic Liquid Experiments in Orbit, (Contract NAS8-11328). Martin CR-65-25, October 1965.

## APPENDIX A

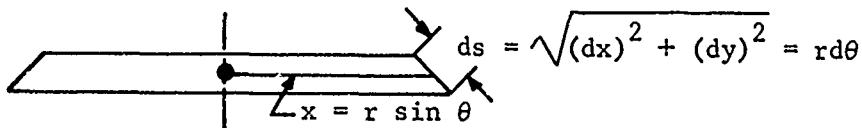
### ANALYSIS OF BUOYANCY FORCE WITH NONCONSTANT DENSITY

An analysis is made of the net buoyancy force on a bubble. For purposes of providing a check on the analytical method, the analysis is first made assuming constant liquid density which leads to the well known result,  $F = \text{volume displaced} \times \text{density}$ . The analysis is then extended to the case in which density varies linearly with distance. The sketch below defines the geometry and coordinate system used in the analysis:



Assume  $\rho_L = \text{constant}$ :

$$F_v = \int_0^\pi P \cos \theta \, dA$$



$$dA = 2\pi r \sin \theta \, ds = 2\pi r^2 \sin \theta \, d\theta$$

$$F_v = \int_0^\pi P \cos \theta (2\pi r^2 \sin \theta) d\theta.$$

Now:

$$P = P_o + y\rho_L, \quad y = r(1 - \cos \theta);$$

$$P = P_o + r\rho_L (1 - \cos \theta);$$

so

$$F_v = \int_0^\pi [P_o + r\rho_L (1 - \cos \theta)] \cos \theta (2\pi r^2 \sin \theta) (d\theta);$$

$$F_v = \int_0^\pi (P_o + r\rho_L) \cos \theta (2\pi r^2 \sin \theta) d\theta - \int_0^\pi r\rho_L \cos^2 \theta (2\pi r^2 \sin \theta) d\theta;$$

$$F_v = 2\pi r^2 (P_o + r\rho_L) \int_0^\pi \cos \theta \sin \theta d\theta - 2\pi r^2 (r\rho_L) \int_0^\pi \cos^2 \theta \sin \theta d\theta;$$

$$F_v = 2\pi r^2 (P_o + r\rho_L) \left[ \frac{1}{2} \sin^2 \theta \right]_0^\pi - 2\pi r^2 (r\rho_L) \left[ \frac{-\cos^3 \theta}{3} \right]_0^\pi;$$

$$F_v = 2\pi r^2 \left[ (P_o + r\rho_L) \left( \frac{1}{2} \sin^2 \pi - \frac{1}{2} \sin^2 0 \right) - r\rho_L \left( \frac{-\cos^3 \pi}{3} + \frac{\cos^3 0}{3} \right) \right];$$

$$F_v = 2\pi r^2 \left[ -r\rho_L \left( -\frac{(-1)^3}{3} + \frac{1}{3} \right) \right];$$

$$F_v = 2\pi r^2 \left[ -r\rho_L \left( +\frac{1}{3} + \frac{1}{3} \right) \right];$$

$$F_v = -2\pi r^2 r\rho_L \cdot \frac{2}{3} = -\frac{4}{3} \pi r^3 \rho_L.$$

Assume  $\rho_L = f(\theta)$ .

Further assume

$$\rho = (P_o + \alpha y),$$

where

$$\alpha = \left( \frac{\Delta \rho}{\Delta y} \right), \quad y = r(1 - \cos \theta).$$

So,

$$\rho = (\rho_o + \alpha r (1 - \cos \theta)).$$

Then:

$$F_v = \int_0^\pi [P_o + r(\rho_o + \alpha r (1 - \cos \theta)) (1 - \cos \theta)] \cos \theta (2\pi r^2 \sin \theta) d\theta;$$

$$F_v = \int_0^\pi P_o \cos \theta (2\pi r^2 \sin \theta d\theta) + \int_0^\pi r\rho_o (1 - \cos \theta) \cos \theta (2\pi r^2 \sin \theta) d\theta +$$

$$+ \int_0^\pi r(\alpha r) (1 - \cos \theta)^2 \cos \theta (2\pi r^2 \sin \theta) d\theta;$$

$$F_v = \int_0^\pi [P_o + r\rho_o (1 - \cos \theta)] \cos \theta (2\pi r^2 \sin \theta) d\theta +$$

$$+ \int_0^\pi r(\alpha r) (1 - \cos \theta)^2 \cos \theta (2\pi r^2 \sin \theta) d\theta;$$

$$F_v = 2\pi\alpha r^4 \left[ \int_0^\pi \cos \theta \sin \theta d\theta + \int_0^\pi -2 \cos^2 \theta \sin \theta d\theta + \int_0^\pi \cos^3 \theta \sin \theta d\theta \right] - \frac{4}{3} \pi r^3 \rho_o;$$

$$F_v = 2\pi\alpha r^4 \left[ \frac{1}{2} \sin^2 \theta - 2 \left( -\frac{\cos^3 \theta}{3} \right) + \left( -\frac{\cos^4 \theta}{4} \right) \right]_0^\pi - \frac{4}{3} \pi r^3 \rho_o;$$

$$F_v = -\frac{4}{3} \pi r^3 \rho_o - \frac{8}{3} \pi \alpha r^4;$$

$$F_v = -\frac{4}{3} \pi r^3 (\rho_o + 2\alpha r).$$

Since

$$\alpha = \frac{\Delta \rho}{\Delta y} = \frac{\Delta \rho}{\Delta T} \cdot \frac{\Delta T}{\Delta y},$$

and assuming the following system properties for n-butyl alcohol:

$$\frac{\Delta \rho}{\Delta T} = 0.000688 \text{ gm/cc-}^\circ\text{C};$$

$$\frac{\Delta T}{\Delta y} = 200^\circ\text{C/cm};$$

$$D = 0.160 \text{ cm};$$

$$r = 0.080 \text{ cm};$$

$$V_b = 2.14 \times 10^{-3} \text{ cm}^3;$$

$$\rho_o = 0.81;$$

then

$$\alpha = (0.000688) (200) = \frac{0.1376 \text{ gm}}{\text{cm}^4};$$

and

$$\begin{aligned} F_v &= V_b(\rho_o + 2\alpha r) = V_b[(0.81 + 2(0.1376)(0.08)] V_b[0.81 + 0.02] = \\ &= 0.83 V_b. \end{aligned}$$

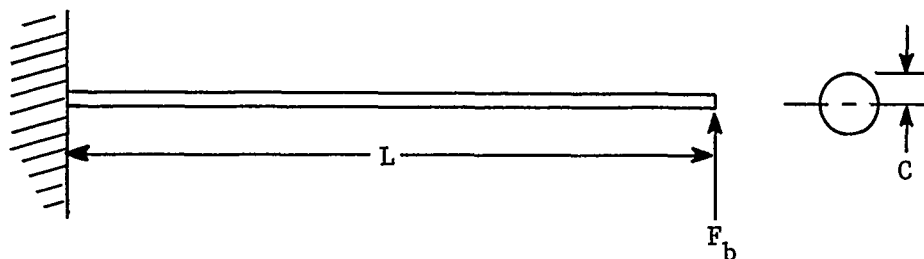


## APPENDIX B

### CANTILEVERED SPRING WIRE

#### A. EXTREME FIBER STRESS

Compute wire size that will deflect and not exceed elastic limit. A sketch is given below:



where:

$$\delta = \frac{MC}{I};$$

$$M = LF_b;$$

$$F_b = \frac{4}{3} \pi r_b^3 \rho_L;$$

$$M = \frac{4}{3} \pi r_b^3 L \rho_L;$$

$$I = \frac{\pi d^4}{64} = \frac{\pi \cdot \cancel{16} r^4}{\cancel{64} 4} = \frac{\pi r^4}{4};$$

$$C = r;$$

then

$$\delta = \left( \frac{4}{3} \pi r_b^3 L \rho_L \right) \frac{0.4 \cancel{r}}{\cancel{43}} = \frac{16}{3} \left( r_b^3 \rho_L \right) \frac{L}{r^3}.$$

where

$\delta\rho$  (elastic limit) for iron wire is  $> 26,000$ ,

$$r = \sqrt[3]{\frac{16}{3} (r_b^3 \rho_L) L \cdot \frac{1}{\delta}} = r_b \sqrt[3]{\frac{16}{3} \rho_L \cdot \frac{L}{\delta}}$$

further,

$$L = 3 \text{ in.}$$

and

$$\rho_L = 0.8 \times 62.4 = 50 \text{ lb/ft}^3 = 0.029 \text{ lb/in.}^3$$

So:

$$r = r_b \sqrt[3]{\frac{16}{3} \times 0.029 \times \frac{3}{\delta}} = r_b \sqrt[3]{\frac{0.465}{\delta}} = 0.775 r_b \sqrt[3]{\frac{1}{\delta}}$$

Letting

$$r_b = 0.08 \text{ cm} = 0.0315 \text{ in.},$$

$$r = 0.775 (0.0315) \sqrt[3]{\frac{1}{26000}} = (0.775)(0.0315)(0.0335) = 0.00816$$

(say 0.001 wire).

#### B. COMPUTE SIZE WIRE TO GIVE PROPER TEST ACCURACY END DEFLECTION

Letting:

$$\Delta = \frac{P\ell^3}{3EI};$$

where

$$P = \frac{4}{3} \pi r_b^3 \rho_L$$

and

$$I = \frac{\pi r^4}{4};$$

then

$$\Delta = \frac{\left(\frac{4}{3} r_b^3 \rho_L\right) L^3}{3E \frac{r^4}{4}} = \frac{16}{9} \frac{r_b^3 \rho_L L^3}{Er^4}.$$

Let:

$$E = 30 \times 10^6;$$

$$r_b = 0.0315 \text{ in.};$$

$$\rho_L = 0.029 \text{ lb/in.}^3;$$

$$L = 3 \text{ in.};$$

$$r = 0.004.$$

Then:

$$\Delta = \frac{(1.78)(0.0315)^3(0.029)(3)^3}{(30 \times 10^6)\left(\frac{0.004}{2.54}\right)^4} = \frac{(1.78)(31.2) \times 10^{-6} (0.029)(27)}{(30 \times 10^6)(256) \times 10^{-12}} =$$

$$= \frac{4.35}{768.0} = 0.00567 \text{ in.} = 0.0144 \text{ cm};$$

$$\Delta = 0.0144 \times 2.54^4 = 41.6 \times 0.0144 = 0.60 \text{ cm.}$$

*"The aeronautical and space activities of the United States shall be conducted so as to contribute . . . to the expansion of human knowledge of phenomena in the atmosphere and space. The Administration shall provide for the widest practicable and appropriate dissemination of information concerning its activities and the results thereof."*

—NATIONAL AERONAUTICS AND SPACE ACT OF 1958

## NASA SCIENTIFIC AND TECHNICAL PUBLICATIONS

**TECHNICAL REPORTS:** Scientific and technical information considered important, complete, and a lasting contribution to existing knowledge.

**TECHNICAL NOTES:** Information less broad in scope but nevertheless of importance as a contribution to existing knowledge.

**TECHNICAL MEMORANDUMS:** Information receiving limited distribution because of preliminary data, security classification, or other reasons.

**CONTRACTOR REPORTS:** Technical information generated in connection with a NASA contract or grant and released under NASA auspices.

**TECHNICAL TRANSLATIONS:** Information published in a foreign language considered to merit NASA distribution in English.

**TECHNICAL REPRINTS:** Information derived from NASA activities and initially published in the form of journal articles.

**SPECIAL PUBLICATIONS:** Information derived from or of value to NASA activities but not necessarily reporting the results of individual NASA-programmed scientific efforts. Publications include conference proceedings, monographs, data compilations, handbooks, sourcebooks, and special bibliographies.

*Details on the availability of these publications may be obtained from:*

SCIENTIFIC AND TECHNICAL INFORMATION DIVISION  
NATIONAL AERONAUTICS AND SPACE ADMINISTRATION

Washington, D.C. 20546